Erbacher, J., Mosher, D.C., Malone, M.J., et al., 2004
Proceedings of the Ocean Drilling Program, Initial Reports Volume 207

8. Site 1261[1]

Shipboard Scientific Party[2]

BACKGROUND AND OBJECTIVES

Site 1261 is located at a water depth of 1899 meters below sea level (mbsl) on the gently dipping (~1°) northwest-facing slope of Demerara Rise, which is ~350 km north of Suriname (see Fig. **F1,** p. 5, in Shipboard Scientific Party, this volume ["Site Survey and Underway Geophysics"]). Site 1261 is the shallowest site of those forming the paleoceanographic depth transect across Demerara Rise. The major objectives were the following:

1. Core and log a Paleogene–Albian section to evaluate paleoceanographic and paleoclimatic changes, with emphasis on major and abrupt events during this interval that include the Eocene/Oligocene (E/O) and Paleocene/Eocene (P/E) boundaries and the Cretaceous oceanic anoxic events (OAEs).
2. Reconstruct the history of the opening of the Equatorial Atlantic Gateway by obtaining benthic foraminifer proxy data. These data will help to understand changes in bottom water circulation over Demerara Rise during the gradual opening of the seaway.
3. Recover continuous and expanded sediment records of the Paleogene and Cretaceous in order to reconstruct short- and long-term changes in greenhouse forcing.

Seismic Stratigraphy

The seismic stratigraphy established for Demerara Rise, including Horizons "A," "B," "B′," and "C," has been correlated to Site 1261 with line GeoB213 (Fig. **F1**). Lines GeoB204 and GeoB208 are orthogonal to line GeoB213 and pass within 5 km of the site to the northwest and south-

F1. Seismic line GeoB213, p. 39.

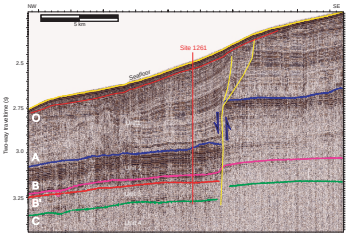

[1]Examples of how to reference the whole or part of this volume.
[2]Shipboard Scientific Party addresses.

Ms 207IR-108

east, respectively. Industry line C2206a passes orthogonal to line GeoB213 8 km to the northwest of the drill site (Fig. F2).

The seismic stratigraphy for Demerara Rise shows increasing sediment thickness to the south (in board). At Site 1261, the uppermost sediment section has not been defined previously. It consists of a thin (30 ms thick; 24 m) package of parallel coherent reflectors that offlap from the upslope direction (south) and truncate against the seafloor ~10 km downslope. This sequence is Quaternary in age, and the base of it is Reflector "O" (Fig. F1).

What was previously defined as seismic Unit 1 (Miocene–Pliocene) (see **Shipboard Scientific Party** ["Site Survey and Underway Geophysics"], this volume) underlies Reflector O. It is largely missing at the other sites. In the immediate vicinity of Site 1261, Unit 1 comprises a well-defined set of coherent seismic reflections of varying amplitudes. The topmost reflections truncate against Reflector O, sometimes in an angular fashion. At the base of the Unit 1 is a 50-ms-thick (~40 m) zone of incoherent reflections capped by a bright reflector that appears to be a debris flow. The bottom of the unit is Reflector A. Unit 1 is 415 ms thick (367 m thick) at the drill site.

Unit 2 is below Reflector A, the presumed early Miocene erosional unconformity. The base of seismic Unit 2 is correlated to Reflector B at 586 ms (550 m). It is represented by a sequence of high-amplitude parallel coherent reflections that are relatively flat lying, dipping 0.5° to the north. Seismic Unit 3, between Reflectors B and C, is estimated to be 150 ms thick (175 m). Much of the acoustic energy in the high-resolution site survey profile (line GeoB213) is lost within the highly reflective Unit 2. Little detail is resolved in Unit 3 as a result. It appears as an acoustically transparent package with occasional semicoherent reflectors at the top and at the very base just above Horizon C. It is difficult to correlate Horizon B and thus to distinguish Subunits 3a and 3b due to this low reflectivity. It has been correlated to the base of the slightly coherent section near the top of Unit 3, but the tie is uncertain.

Reflector C, at the base of the section of interest, is an unconformity. No coherent subsurface data are recognizable on the survey data, but the nearby industry line C2206a shows the underlying section. At Site 1261, the unconformity appears as a disconformity and it is difficult to pick Reflector C as a result. Further below, reflections form a broad anticline, which is fault-bounded to the southwest and folded into a syncline to the northeast.

A listric-normal fault is shown on line GeoB213 (Fig. F1) 5 km southeast of the drill site. This fault apparently has affected the entire sediment column. Offset across the fault is ~30–60 ms in the deeper portion of the section at Reflector C, whereas in the upper portion it is on the order of 200 ms. This discrepancy in offset can be accounted for only by invoking either significant rotation or massive slumping in the upper sediment column. The fault splays at 300 ms subbottom, showing significant tilting of reflections in the interval between offsets, which is further evidence of slumping.

F2. Multichannel seismic line C2206a, p. 40.

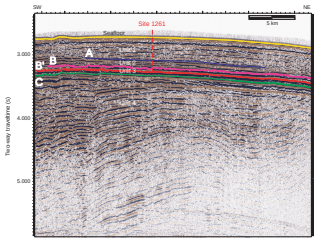

OPERATIONS

Transit from Site 1259 to Site 1261

We departed Site 1259 for Site 1261 at 1330 hr on 16 February 2003, making the 17.0-nmi transit in 2.3 hr at an average speed of 7.4 kt. Af-

ter positioning the ship over the site's coordinates at 1547 hr on 16 February, thrusters and hydrophones were lowered and a beacon was deployed, commencing operations at Site 1261.

Hole 1261A

A standard rotary core barrel (RCB) bottom-hole assembly was assembled and lowered to the seafloor, which was tagged at 1899.7 mbsl. Hole 1261A was spudded with the RCB at 1940 hr on 16 February and drilled to 236.9 mbsf, taking spot cores from the following intervals: 0–22.5, 69.7–79.3, 131.4–141.1, and 189.1–198.7 mbsf. Continuous coring resumed from 236.9 to 669.4 mbsf (total recovery = 73.4%) (Table T1). The hole was displaced with 208 bbl of sepiolite mud for abandonment. The bit was pulled clear of the seafloor at 1140 hr on 19 February, officially ending Hole 1261A.

T1. Coring summary, p. 77.

Hole 1261B

Hole 1261B was spudded at 1250 hr on 19 February and washed from 0 to 525.3 mbsf. Rotary coring commenced at 525.3 mbsf and continued to a total depth of 674.1 mbsf (recovery = 62.2%) (Table T1). In preparation for logging, the bit was released, the hole was displaced with 209 bbl of sepiolite mud, and the base of the pipe was pulled to 102 mbsf. The hole was then logged with both the triple combination (triple combo) and Formation MicroScanner (FMS)-sonic tool strings from 652 mbsf, with two passes of each. On the third logging run, the Well Seismic Tool (WST) could not be advanced past a bridge at 192 mbsf and a checkshot survey was conducted only in the interval above the bridge. In preparation for the transit to Rio de Janeiro, Brazil, the drill string was tripped to the ship, clearing the rotary table at 0035 hr on 23 February, ending operations in Hole 1261B.

Transit from Site 1261 to Rio de Janeiro, Brazil

After retracting the thrusters and hydrophones and securing the ship for transit, we departed for Rio de Janeiro at 0045 hr on 23 February. The 2724-nmi transit required 279.8 hr at an average speed of 9.7 kt. At 1720 hr on 6 March, the first line was ashore ending Leg 207.

LITHOSTRATIGRAPHY

Site 1261 lies in the shallowest water depth (~1900 mbsl) of the Leg 207 Demerara Rise depth transect. From the two holes at Site 1261, we recovered 68% of the ~478 m cored (Fig. F3). Sediments and sedimentary rocks recovered at Site 1261 range in age from Albian to Pleistocene (see "Biostratigraphy," p. 10), but the section was drilled and washed with occasional spot cores from 0 to 237 mbsf. The recovered section is interrupted by at least two major and several minor hiatuses.

Five lithostratigraphic units were recognized at Site 1261 (Table T2). The oldest unit recovered (Unit V) is dominated by quartz sandstone. The superjacent unit (Unit IV) is composed dominantly of laminated calcareous organic-rich claystone (black shale) and laminated chalk/limestone. The youngest three units (Units I–III) recognized are pelagic and are composed dominantly of foraminifers, nannofossils, carbonate debris, diagenetic calcite, and clay. These pelagic sediments are perva-

F3. Carbonate and TOC, p. 41.

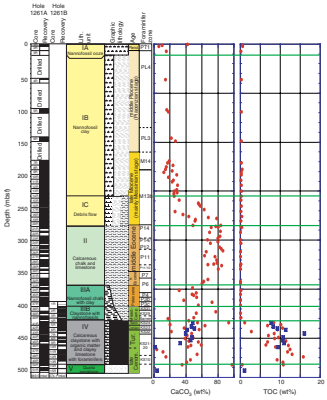

T2. Summary of lithology, p. 79.

sively bioturbated; pyrite and other iron sulfides are found throughout the pelagic interval but are most abundant in Unit III. Clay and zeolite are also relatively abundant in Unit III. Unit II contains a relatively high abundance of diagenetic calcite, with only minor quantities of zeolite. The carbonate content for pelagic Units I and II increases progressively downhole from 10 to 80 wt%. Values then decline through the clay-rich Unit III to ~20–50 wt% carbonate at its base.

Lithostratigraphic units recognized at Site 1261 generally parallel those reported for Sites 1257–1260 (Fig. F4). Differences between the lithostratigraphic divisions in units co-occurring at Site 1261 and other Demerara Rise sites represent differences in the level at which unit boundaries are placed and can be attributed to uncertainty related to short coring gaps and hiatuses of varying length and age. Unit I is considerably thicker at Site 1261 than previous sites because of the recovery of an extraordinarily thick pre-Eocene package. Units II and III were comparatively condensed in relation to sections recovered from previous sites, but the succession of lithologies was similar. Unit IV ranked second in total black shale thickness of all sites (89 m) and represents the longest stratigraphic range of Unit IV at one site, with deposition spanning from the upper Santonian to the lower Cenomanian (see "Biostratigraphy," p. 10). Finally, the basal Unit V (quartz sandstone) at Site 1261 is similar to sandstones recovered from Unit V at Sites 1257 and 1259. This unit shows significant variation across all sites and probably represents synrift deposition. Quartz grains of Unit V at Site 1261 are subangular medium sand, implying a relatively little weathering and a relatively proximal setting.

F4. Lithostratigraphic summary, p. 42.

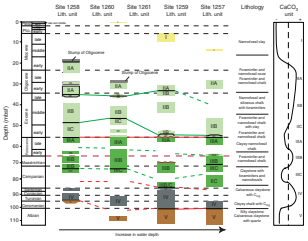

Lithostratigraphic Units

Unit I

Interval: 207-1261A-4R, 0 cm, through 20R-5, 120 cm
Depth: 0.00–369.30 mbsf
Thickness: 369.30 m
Age: Pleistocene–late Miocene
Lithology: nannofossil ooze, nannofossil clay, and clayey nannofossil ooze

Unit I is composed dominantly of nannofossil ooze, nannofossil clay, and a matrix-supported conglomerate. This unit also includes rare bluish gray clay layers. Pyrite and foraminifers are minor constituents throughout the unit.

Unit I is subdivided into three subunits. Subunit IA is a nannofossil ooze, and Subunit IIB is a nannofossil clay. Spot coring over the interval from 22.5 to 236.9 mbsf does not allow for the nature or placement of the boundary between these subunits to be rigorously determined. Subunit IC is a matrix-supported conglomerate composed of clayey nannofossil ooze (matrix) and nannofossil chalk (clasts). Unit I is distinguished from Unit II by a sharp transition from relatively clay-rich oozes and debris flow deposits of late Miocene age at the base of Subunit IC to the pelagic middle–early Eocene nannofossil chalks and limestones of Unit II.

Subunit IA

Interval: 207-1261A-1R-1, 0 cm, through 4R-1, 0 cm
Depth: 0.00–69.70 mbsf

Thickness: 69.70 m
Age: Pleistocene–middle Pliocene
Lithology: nannofossil ooze with foraminifers

Subunit IA is a nannofossil ooze with foraminifers that is characterized by few discrete traces and frequent black mottles and streaks. There is a sharp color change from pale yellow/pale brown to olive gray/greenish gray at ~0.25 mbsf. Neither sediment composition nor sediment fabric change is noticeable at this boundary, so it is interpreted as a diagenetic redox boundary that propagated down from the seafloor. Below this color change, the sediments are light greenish gray with only subtle variations. The base of Subunit IA (69.70 mbsf) is placed at the base of a coring gap between nannofossil ooze (Subunit IIA) and nannofossil clay (Subunit IB).

Subunit IB

Interval: 207-1261A-4R-1, 0 cm, through 14R-5, 15 cm
Depth: 69.70–310.55 mbsf
Thickness: 240.85 m
Age: middle Pliocene–late Miocene
Lithology: nannofossil clay

Subunit IB is a greenish gray to olive-gray to bluish gray nannofossil clay. The top of this subunit is placed at the first massive clay-rich sediments at the top of Core 207-1261A-4R (Fig. F5). Clay contents were estimated at 40%–50% in smear slides. Nannofossils compose most of the rest of the sediment. Color variations are seen as distinct bluish gray layers found at a 20- to 30-cm spacing superimposed on meter-scale gray to reddish brown color cycles. Blue layers have clay contents of 80%–90%, with the remaining 10%–20% composed of nannofossils. Bioturbation is moderate to pervasive throughout, but only a few discrete *Zoophycos* and *Planolites* burrows are observed. Pyrite is millimeter-sized crystals through much of the subunit and occasionally concentrated within burrows. The base of this subunit is marked by a distinct contact with the multicolored matrix-supported conglomerate of Subunit IC at 310.55 mbsf (Hole 1261A).

F5. Representative lithologies, Unit I, p. 43.

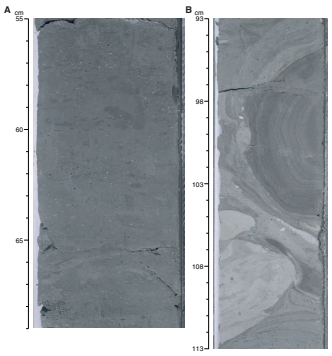

Subunit IC

Interval: 207-1261A-14R-5, 15 cm, through 20R-5, 117 cm
Depth: 310.55–369.27 mbsf
Thickness: 58.72 m
Age: late Miocene
Lithology: clayey nannofossil ooze and nannofossil chalk (matrix-supported conglomerate)

Subunit IC is composed of a matrix-supported conglomerate, interpreted as a debris flow (Fig. F5B). The matrix is clay rich with well-preserved nannofossils and well-preserved but heavily fragmented foraminifers. The clasts consist of nannofossil chalk of late Miocene age (Fig. F5C). The top of this subunit is placed at a distinct contact between the olive-gray to greenish gray nannofossil clay of Subunit IB and the multicolored matrix-supported conglomerate of Subunit IC at 310.55 mbsf (Hole 1261A). The subunit is intensely slumped, folded, and faulted (e.g., Cores 207-1261A-15R and 19R). The intervals that appear to be less disturbed are characterized by moderate to heavy bioturbation, with distinct dark coloration of backfilled *Zoophycos* and *Planolites* burrows.

These more stable sedimentary intervals possess distinctive sharp, thin, very dark green layers (Cores 207-1261A-16R and 17R), which may represent redox boundaries in the sediment. Large clasts of nannofossil chalk are located in Sections 207-1261A-14R-6, 15R-1, 15R-6, 17R-6, and 19R-5 through 19R-CC. These chalk clasts are moderately bioturbated with discrete white mottles. The base of Subunit IC is placed at a sharp contact of the matrix-supported conglomerate with the underlying middle Eocene calcareous chalk of Unit II at 369.27 mbsf.

Unit II

Interval: 207-1261A-20R-5, 120 cm, through 33R-4, 128 cm
Depth: 369.27–491.70 mbsf
Thickness: 122.43 m
Age: middle Eocene–early Eocene
Lithology: calcareous chalk, nannofossil chalk, and limestone

Unit II is composed of calcareous chalk containing nannofossils, foraminifers, diagenetic calcite, and clay, which grades downcore to limestone. Cyclic alternations (20–50 cm thick) between white to light greenish gray and greenish gray calcareous chalks are a striking feature of this unit (Fig. F6A). These color cycles appear to be caused by a slightly higher clay content in the darker intervals than in the lighter intervals and may have been enhanced by diagenesis. Foraminifers and nannofossils are poorly preserved in this subunit and range in abundance from 15%–30% to 10%–15% in the light and dark intervals, respectively. Diagenetic sparry calcite content is relatively high but variable (15%–50%). Clay and zeolite are also present. Sediment in Section 207-1261A-33R-4 (around the P/E boundary) displays a distinct reddish brown hue (Fig. F6) and is characterized by elevated clay content (up to 90%).

Rarely interbedded within color couplets are short ~5- to 10-cm intervals of indurated siliceous calcareous chalk. Bioturbation is heavy to common throughout Unit II. The darker intervals have a wispy anastomosing subhorizontal fabric with prominent *Zoophycos* burrows, and the lighter intervals are mottled with few distinct burrows (Fig. F6). Mottles, blebs, and streaks are common and seem to be associated with burrows. The base of Unit II (Hole 1261A [491.70 mbsf]) is defined by a transition to the more clay-rich calcareous chalk of Unit III. This transition is gradational, and the boundary is placed at the base of the red and green clay layer corresponding to the biostratigraphically defined P/E boundary.

F6. Representative lithologies, Units II and III, p. 45.

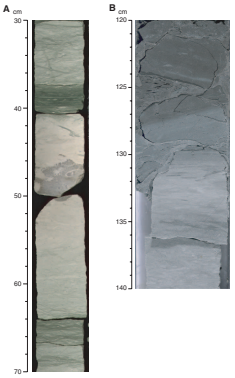

Unit III

Intervals: 207-1261A-33R-4, 128 cm, through 41R-1, 33 cm; and 207-1261B-2R-1, 0 cm, through 5R-4, 109 cm
Depths: Hole 1261A: 491.70–564.13 mbsf; and Hole 1261B: <530.00–563.00 mbsf
Thickness: 72.43 m
Age: late Paleocene–late Campanian
Lithology: nannofossil chalk with clay and claystone with nannofossils

Unit III is composed of nannofossil chalk with clay and claystone with nannofossils. Planktonic foraminifers, calcite debris (both biogenic and diagenetic), pyrite, barite, and zeolites are minor constituents in

portions of the unit. Dominant colors are shades of greenish gray that grade to dark gray at the base. Distinct to subtle color alternations on a decimeter scale occur. The upper contact with Unit II is placed at the base of a distinct 20-cm-thick greenish gray and red clay layer that corresponds to the biostratigraphically recognized P/E boundary (see "Biostratigraphy," p. 10). Unit III is easily distinguished from Unit IV by its lack of laminations, low organic carbon, and greenish gray color. The base of Unit III is placed at the first downhole occurrence of high total organic carbon (TOC)-laminated strata (Fig. F6). Unit III is subdivided into two subunits at the K/T boundary. The K/T boundary coincides with a downhole shift to clay from carbonate as the major lithologic constituent. No ejecta layer was recovered at Site 1261, and the boundary occurs at Sections 207-1261A-37-CC and 207-1261B-2R-3, 78 cm (see "Biostratigraphy," p. 10).

Subunit IIIA

Intervals: 207-1261A-33R-4, 128 cm, through 39R-1, 0 cm; and 207-1261B-2R-1, 0 cm, through 2R-3, 83 cm
Depths: Hole 1261A: 491.70–544.60 mbsf; and Hole 1261B: <530.00–533.83
Thickness: 52–90 m (Hole 1261A)
Age: Paleocene
Lithology: nannofossil chalk with clay

Subunit IIIA consists of light greenish gray to greenish gray mottled nannofossil chalk with clay and clayey nannofossil chalk. Carbonate contents are generally between 40 and 60 wt% (Fig. F3). Zeolites, quartz, calcite debris (diagenetic and biogenic), and pyrite are common as minor constituents. Subtle to distinct alternations between light (relatively carbonate rich) and dark (relatively clay rich) color bands occur on a decimeter scale. Burrow mottling is pervasive. Discrete traces including *Zoophycos, Planolites,* and *Chondrites* are common and often filled with black monosulfide minerals. Subunit IIIA is distinguished from Subunit IIIB by its generally higher calcium carbonate content and lower clay content. The contact is placed at the K/T boundary, which is roughly coincident with a downcore shift from carbonate to clay as the major lithologic constituent.

Subunit IIIB

Intervals: 207-1261-39R-1, 0 cm, through 41R-1, 33 cm; and 207-1261B-2R-3, 83 cm, through 5R-4, 109 cm
Depths: Hole 1261A: 544.60–564.13 mbsf; and Hole 1261B: 533.83–563.30 mbsf
Thickness: 29.47 m (Hole 1261B)
Age: Maastrichtian–late Campanian
Lithology: Claystone with nannofossils

Subunit IIIB consists of greenish gray to dark gray claystone with nannofossils and minor amounts of claystone with foraminifers and nannofossils and clayey limestone with foraminifers. Pyrite is common, and barite is present as millimeter- to centimeter-sized nodules. Light–dark color alternations occur with a 20- to 50-cm spacing and represent changes in the relative abundance of clay and carbonate. Bioturbation is heavy to pervasive, but darker intervals often have a subhorizontal fabric that may reflect primary lamination. *Zoophycos, Planolites,* and *Chondrites* are often ringed by diagenetic halos. The lower portion of Unit III

is less bioturbated, more clay rich, and darker in color than other parts of the unit. Unit III is distinguished from Unit IV by its lack of laminations, low organic carbon content, and greenish gray color. The lower contact is placed at the first downhole occurrence of laminated black calcareous claystone with organic matter (Fig. F6).

Unit IV

Intervals: 207-1261A-41R-1, 33 cm, through 50R-3, 32 cm; and 207-1261B-5R-4, 109 cm, through 14R-4, 51 cm
Depths: Hole 1261A: 564.13–653.52 mbsf; and Hole 1261B: 563.3–650.21 mbsf
Thickness: 89.39 m (Hole 1261A)
Age: Santonian–late Cenomanian
Lithology: calcareous claystone with organic matter, clayey chalk with nannofossils, and clayey limestones

Unit IV ranges from black, finely laminated claystone with organic matter to olive-gray laminated clayey limestone and clayey chalk with nannofossils. The top of the unit is defined by a relatively sharp shift from the bioturbated greenish gray clayey calcareous chalk of Unit III above to the laminated claystones below (Fig. F6).

The two major lithologies in Unit IV, laminated claystone and laminated nannofossil chalk and limestone, show cyclic alternations and gradational contacts over a centimeter to decimeter scale (Fig. F7). There are two modes of cyclicity observed. Fine-grained laminated olive-gray chalks and limestones of 20–50 cm thickness are found every few meters in the top of Unit IV interbedded with organic-rich claystones that contain phosphoritic stringers, fecal pellets, and inoceramids. In the middle of Unit IV, coarse-grained calcite-cemented foraminifer sands are present (Sections 207-1261A-46R-5, 83 cm, to 48R-1, 140 cm; and 207-1261B-12R-1, 0 cm, to 12R-4, 40 cm). These coarser stringers alternate with the organic-rich claystone over 20- to 50-cm scale for an interval of up to 11 m and occur in the fine-grained olive-gray laminated limestone cycles described above. At the base of the unit, the sediments still show cyclic variation but become generally lighter in color, reflecting an increase in carbonate content (Sections 207-1261A-49R-1, 80 cm, to 50R-3, 23 cm; and 207-1261B-13R-2, 0 cm, to 14R-4, 48 cm). The exception to this trend is the black laminated bed found immediately above Unit V in interval 207-1261A-50R-3, 15–32 cm.

Intervals 207-1261A-45R-2, 1–45 cm, to 207-1261B-9R-4, 121–153 cm, contain coarse-grained massive beds with glauconite, fecal pellets, diagenetic calcite, and phosphatic nodules and stringers that extend in burrows into the underlying sediment. These beds are similar to lithologies found in the black organic-rich claystones at Sites 1257–1260 and also appear as a distinctive natural gamma ray (NGR) and magnetic susceptibility peak (see "Physical Properties," p. 29). Additionally, moderately to pervasively bioturbated centimeter-scale beds with coarser sediment containing fecal pellets and fish debris are a minor lithology.

There are several possible ash layers in Unit IV that can be correlated between Holes 1261A and 1261B (e.g., intervals 207-1261A-42R-5, 55–58 cm, and 207-1261B-7R, 138–140 cm). These are homogeneous gray clay layers that have a waxy texture and are devoid of nannofossils. Cores from the two holes at this site also contain several blue diagenetic calcite fans (cone-in-cone structures) (Fig. F7A, F7B) precipitated in a black claystone matrix (intervals 207-1261A-47R-1, 86–91 cm [missing

F7. Representative lithologies, Unit IV, p. 47.

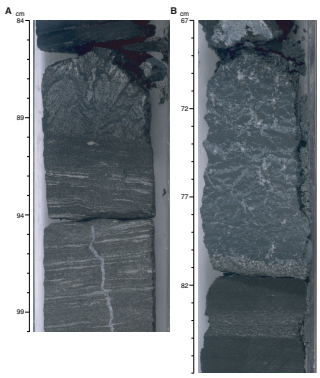

in Hole 1261B], and 48R-4, 63–81 cm, which may correlate with interval 207-1261B-12R-6, 127–142 cm).

Unit V

Intervals: 207-1261A-50R-3, 32 cm, through 51R-2, 114 cm; and 207-1261B-14R-4, 51 cm, through 16R-1, 148 cm
Depths: Hole 1261A: 653.52–662.26 mbsf; and Hole 1261B: 650.21–665.98 mbsf
Thickness: 15.77 m (Hole 1261B)
Age: Albian? (or younger)
Lithology: quartz sandstone

Unit V consists of gray coarse-grained quartz sandstone with calcite cement. The sandstone is heterogeneous with white and black speckles, and the unit is moderately biscuited. The top of the unit is placed at a sharp color and lithologic boundary (Fig. F7) and the unit extends to the bottom of Holes 1261A and 1261B. The quartz grains are subangular. Shell material and ammonite fragments are minor sedimentary components. Silty clay intercalated with the sandstone in interval 207-1261B-16R-1, 93–113 cm, has yielded a possible calcareous nannofossil age of late Albian–Cenomanian. The base of Site 1261 (Sample 207-1261B-16R-1, 141–147 cm) contains a limestone rich in oysters of the genus *Aucellina*.

Summary

The oldest interval recovered at Site 1261 is a quartz sandstone unit (Unit V) of late Albian–Cenomanian age. These rocks may represent synrift deposition. Unit V at Site 1261 appears to be correlative to Unit V at other sites. However, poor age control at all sites limits the rigor of this correlation. Site 1261 may represent a more proximal or high-energy site of sedimentation than the shallow-marine silty calcareous claystones at Site 1260, the claystones with organic matter at Site 1258, and the tidal, possibly calcareous, siltstones of Site 1259.

From the late Cenomanian to Santonian, high productivity and low bottom water oxygen levels, resulting in the preservation of large volumes of organic and phosphatic matter, prevailed at Site 1261. This phase is recorded in the sediments by the dark laminated calcareous claystones and laminated chalks/limestones of Unit IV. Organic carbon concentrations in Unit IV approach 16 wt% TOC, with the organic matter of marine origin (see **"Organic Geochemistry,"** p. 24). Zeolites (clinoptilolite) and rare radiolarians suggest siliceous microfossils were a common component of the sediment. Carbonate values are highly variable (5–95 wt%) and in part reflect diagenetic dissolution and precipitation of inorganic calcite.

Open marine conditions and oxic bottom waters were established by the late Campanian, as indicated by the heavily bioturbated pelagic marls of Unit III. The sharp contact between the bioturbated claystones of Unit III and the laminated shales, clayey nannofossil chalks, and limestones of Unit IV in Hole 1261A reflects a hiatus. A glauconite-rich interval in Hole 1261B, however, is consistent with the transition being recorded by a highly condensed interval. Furthermore, the trace fossils and sedimentary fabric may indicate that bottom waters were relatively dysoxic in the late Campanian and early Maastrichtian.

The K/T boundary interval and associated impact ejecta layer are missing from Holes 1261A and 1261B. Hole 1261B gives a latest Maas-

trichtian age immediately below Sample 207-1261B-2R-3, 78 cm, and an early Danian age immediately above, implying a short hiatus. The P/E boundary seems to be relatively complete at Site 1261. A 3-cm-thick greenish gray clay layer and superjacent 12-cm-thick reddish brown clay layer in Hole 1261A fall in an interval that contains the P/E boundary (see **"Biostratigraphy,"** p. 10). The lack of carbonate in this layer is consistent with sedimentary changes expected during the Paleocene/Eocene Thermal Maximum (PETM).

Above the Eocene calcareous chalks, an extensive Miocene debris flow was cored, which exhibited intense slumping, folding, and faulting. Overlying the debris flow, there is a ~290-m-thick sequence of late Miocene and Pliocene nannofossil clay, although much of this interval was not cored. The Pliocene sediments are capped with a 25-cm veneer of Pleistocene nannofossil ooze.

BIOSTRATIGRAPHY

The two holes at Site 1261 document a 370-m-thick sequence of Pleistocene–late Miocene sediments overlying 300 m of middle Eocene–Cenomanian marine deposits. These yielded calcareous nannofossils, planktonic foraminifers, and radiolarians in varying abundances and states of preservation, depending on lithology and sediment induration. The shipboard examination of these microfossil groups from core catcher samples was supplemented by additional samples from the cores. The biostratigraphic data permitted zonal or stage assignments to be made for the entire sequence. The upper 230 m of the succession (i.e., most of the Neogene) was only recovered by six spot cores; thus, biostratigraphic boundaries encountered in this interval are loosely defined. Datum levels are summarized in Figure **F8** and in Tables **T3, T4, T5, T6,** and **T7.**

A 13-m-thick nannofossil ooze (Samples 207-1261A-1R, 0 cm, to 2R-CC) at the top of the section has a Pleistocene age. This unit overlies a 205-m-thick nannofossil clay (Samples 207-1261A-3R, 0 cm, to 6R-CC) of middle Pliocene age. The boundary to the underlying late Miocene nannofossil clays (Core 207-1261A-7R to Section 20R-5) is not present because of isolated spot coring in the upper part of the succession. The lower part of the Miocene succession (Cores 207-1261A-14R to 20R) is heavily slumped and reworked. The subsequent 165 m of calcareous chalk (Sections 207-1261A-20R-6 to 37R-CC) are of middle Eocene–Paleocene age. A pronounced hiatus at the top of this unit represents the middle Miocene–late Eocene. The P/E boundary, present in Sample 207-1261A-33R-4, 105 cm, is overlain by ~30 cm of radiolarian claystone that may represent the PETM. The lowermost Paleocene (planktonic foraminifer Zone P1 and calcareous nannofossil Zones NP1 and NP2) is missing as well as the earliest Danian boundary clay and the spherule layer, indicating an unconformity across the Cretaceous/Tertiary (K/T) boundary.

The subjacent, highly condensed 33-m section of upper Maastrichtian–lower Campanian nannofossil chalk (Sections 207-1261A-38R-CC to 41R-1) is similar to that of the Paleocene, with moderately or poorly preserved calcareous microfossils. The lowermost part of the Maastrichtian/Campanian chalk facies, enriched in glauconite, overlies an 89-m-thick Santonian–Cenomanian black shale succession (Sections 207-1261A-41R-2 to 50R-3). Calcareous microfossils are generally present throughout this unit, with planktonic foraminifers often poorly pre-

F8. Calcareous microfossil and radiolarian biozones, p. 49.

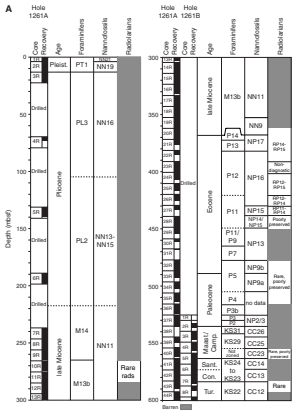

T3. Calcareous nannofossils, p. 80.

T4. Planktonic foraminifers, Hole 1261A, p. 81.

T5. Planktonic foraminifer datums, p. 82.

T6. Datum levels, ages, and preservation of samples, p. 83.

T7. Planktonic foraminifers, Hole 1261B, p. 84.

served. Calcareous nannofossils and planktonic foraminifers of Cenomanian age are present near the base of the black shale. Samples 207-1261A-47-CC, 49-CC, and 50-CC supplied nannofossils and planktonic foraminifers of mid- to late Cenomanian age. A sharp contact between the laminated black shale and quartz sandstone (lithostratigraphic Unit V) occurs in Sample 207-1261A-50R-3, 32 cm. The latter unit did not provide any calcareous microfossils and is not dated. However, oysters and ammonites are present in these sandstones and may provide biostratigraphic information during shore-based studies.

Calcareous Nannofossils

Unlike the sections from other Leg 207 sites, the two holes at Site 1261 recovered a considerable amount of Neogene sediment as well as Paleogene to mid-Cretaceous deposits. These materials contain generally common to abundant calcareous nannofossils of moderate to good preservation that vary with lithology. These fossils allowed for zonal or stage assignments, summarized in Figures **F8A** and **F8B** and Tables **T3** and **T4.** Core catcher samples were examined for all holes and supplemented as time permitted by samples from the cores to further refine zonal assignments.

Sample 207-1261A-1R-CC, 12–17 cm, yielded upper Quaternary sediment with well-preserved nannofossils assigned to Zone NN21. The core catcher contained very abundant *Emiliania huxleyi,* abundant *Gephyrocapsa oceanica, Rhabdosphaera clavigera, Helicosphaera carteri,* and common *Ceratolithus cristatus*. The abundance and preservation is similar in the next core (also Quaternary), where Sample 207-1261A-2R-CC contained *Pseudoemiliania lacunosa* and belongs to Zone NN19.

The middle–lower Pliocene is indicated by a variety of discoasters in Samples 207-1261A-3R-CC to 4R-CC, namely *Discoaster brouweri, Discoaster pentaradiatus, Discoaster variabilis, Discoaster tamalis,* and *Sphenolithus* sp. If none of these taxa are reworked, the assemblage should be assigned to Zone NN16. *Reticulofenestra pseudoumbilica* in Cores 207-1261A-5R and 6R denotes Zones NN13–NN15.

Uppermost Miocene sediments in Sample 207-1261A-7R-CC contain *Amaurolithus delicatus* (Messinian [Zone NN11 or Subzone CN9b]). Sample 207-1207-261A-8R-CC yielded *Discoaster quinqueramus,* which is abundant in the subjacent Sample 207-1261A-9R-CC, as is *D. pentaradiatus, R. pseudoumbilica, Sphenolithus moriformis,* and a few well-preserved *Nicklithus amplificus*. A single specimen of *Eiffellithus turriseiffelii* is reworked from the Cretaceous. This sample is assigned to Zone NN11 or, more precisely, to Subzone CN9bB of the augmented Okada and Bukry (1980) scheme. The next four cores (through Sample 207-1261A-13R-CC) also belong to Zone NN11 or, more precisely, to Subzone CN9bA, as there are few to rare *A. delicatus* and the generally rare *N. amplificus* is not observed.

Triquetrorhabdulus rugosus is rare in Sample 207-1261A-11R-CC, whereas *D. quinqueramus* is abundant, and late-evolved forms of *Discoaster berggrenii* (stellate knobs covering ~80% of the central area) are present in Sample 207-1261A-12R-CC. Three-rayed focus of *D. quinqueramus* are common in the subjacent core catcher in addition to a reworked specimen of *Discoaster calcaris*.

Initially, Sample 207-1261A-14R-CC appeared straightforward, although slightly older (~Zone NN10 or Subzone CP8a) than overlying samples, with little clay to dilute discoasters such as abundant *Discoaster challengeri* and a few specimens of *D. calcaris, T. rugosus, Mi-*

nylitha convallis, and *Pontosphaera multipora*. The sample contains a reworked specimen of *Coronocyclus nitescens*. The next two core catchers were considerably older (middle–lower Miocene Zones NN6 and NN4), but Sample 207-1261A-17R-CC was considerably younger (upper Miocene Zone NN11 again), indicating an age inversion.

The lower half of Core 207-1261A-14R shows a variety of clasts of different colors swirled in a dark brown upper Miocene (Zone NN11) matrix (Fig. **F8A**). The clasts include pieces such as that found in Sample 207-1261A-15R-CC, a coarse foraminifer-rich limestone with abundant *Discoaster exilis, R. pseudoumbilica,* and *C. nitescens* but no *Cyclicargolithus floridanus* or *Discoaster kugleri;* hence, it belongs to middle Miocene Zone NN6. The subjacent Sample 207-1261A-16R-CC contains a greenish calcareous ooze with *C. floridanus, Sphenolithus heteromorphus, C. nitescens, Calcidiscus premacintyrei, D. exilis,* and abundant *Discoaster petaliformis* but no *Helicosphaera ampliaperta,* an assemblage equivalent to Zone NN5. The same assemblage was noted in a small clast (Sample 207-1261A-14R-5, 42 cm) as a minor admixture to a Messinian (Subzone CN9bB) assemblage, whereas a light green clast at 131 cm in this section was dated as lower Miocene Zone NN4 (CN3) (see below for similar dates for these two sampled provided by planktonic foraminifers). A Zone NN4 assemblage was also detected as a minor admixture to Zone NN11 material in Sample 207-1261A-14R-5, 35 cm.

The middle Miocene clast lithologies and/or microfossil assemblages were not found in situ in the remainder of the Miocene section at this site. They, therefore, provide some indication of the nature and extent of the original stratigraphic sequence in the source area(s) from which they came.

Sample 207-1261A-17R-CC contains *D. quinqueramus, D. berggrenii, Discoaster neohamatus, D. calcaris,* and one heavily overgrown reworked specimen of *Discoaster deflandrei* and was assigned to Zone NN11 (approximately Subzone CN9a). This Zone NN11 assemblage evidently represents the matrix for this portion of the slumped material. A similar matrix age is indicated by Sample 207-1261A-18R-CC, which is a green glauconitic clay studded with numerous small (5 mm) round whitish coarse-grained clasts. Both the green and white lithologies yielded nannoliths of two ages: Zone NN11, as indicated by *D. quinqueramus,* and Zone NN5, denoted by common *S. heteromorphus, C. floridanus,* and *Helicosphaera wilcoxonii*. Sample 207-1261A-19R-CC, on the other hand, contains a calcite-cemented, mottled, light green nannofossil chalk with *Discoaster hamatus, Catinaster coalitus, Catinaster calyculus, Hayaster perplexus, Calcidicus macintyrei,* and *R. pseudoumbilica,* indicative of Zone NN9, an assemblage not seen elsewhere in the sequence here.

The base of the slumped upper Miocene section rests on middle Eocene chalk, as displayed in Section 207-1261A-20R-5, 118 cm. The well-indurated core catcher contains a sparse, poorly preserved assemblage characteristic of upper Zone NP17 with *Chiasmolithus grandis, Reticulofenestra umbilica,* and small *Dictyoccocites bisectus* (9 µm long, representing an early evolutionary stage of development).

The abundance of opal-CT lepispheres in the nannofossil smear slides indicates that the biogenic silica usually seen in Eocene chalks at previous Leg 207 sites has been largely altered under the considerably thicker overburden here. The Eocene at this site is overlain by ~370 m of strata, as opposed to ~70 m at Site 1257, 5 m at Site 1258, 130 m at Site 1259, and 40 m at Site 1260. This, plus heavy overgrowth on the discoasters, indicates a relatively advanced state of diagenesis at the present site that has considerably reduced the diversity and abundance

of the nannofossils and diminished their utility for age control. Nevertheless, Sample 207-1261A-21R-CC could still be assigned to upper Zone NP17.

Abundant *Chiasmolithus solitus* accompanied by few *R. umbilica* date Sample 207-1261A-22R-CC as upper Zone NP16 (Subzone CP14a), whereas the absence of *R. umbilica* in the subjacent core catcher suggests lower Subzone NP14b. Preservation of nannofossils is too poor to allow reliable dating of the next two core catchers downhole, but these also appear to belong to Zone NP16. The presence of the total range marker, *Chiasmolithus gigas,* however, indicates Zone NP15 (Subzone CP13b) for Sample 207-1261A-27R-CC, and *Rhabdosphaera inflata* suggests upper Zone NP14 for Sample 207-1261A-28R-CC.

Poor preservation prevented precise dating of Samples 207-1261A-29R-CC to 31R-CC. *Discoaster multiradiatus, Neochiastozygus junctus,* and *Zygrhablithus bijugatus* with only scattered fasciculiths date Sample 207-1261A-32R-CC as upper Zone NP9, above the P/E boundary. That boundary lies in Sample 207-1261A-33R-4, 105 cm, where it is marked by a clay band. The reversal in dominance downhole across this epoch boundary from *Z. bijugatus/N. junctus* to fasciculiths was confirmed in the core catcher, which is assigned to Subzone NP9a. Subzone NP9a continues downhole through Sample 207-1261A-34R-CC. No samples were analyzed for nannofossils from Cores 207-1261-35R and 36R.

The K/T contact was not recovered in Hole 1261A. Sample 207-1261A-37R-CC contains mostly Cretaceous taxa (such as *Micula murus*), but two samplings of the core catcher also disclosed a sparse but persistent representation of the Tertiary taxa *Coccolithus pelagicus, Chiasmolithus danicus,* and moderate-sized (6.25 µm) *Ericsonia subpertusa*. This assemblage belongs to the Danian Zone NP3. Essentially the same assemblage with large *Cruciplacolithus edwardsii* (12.5 µm) occurs upcore (Samples 207-1261A-37R-5, 0–1 cm, and 37R-1, 0–1 cm). The next core returned only a modest-sized core catcher sample and no other material; hence, the contact was not observed.

A disconformity at the K/T contact is clearly visible in Hole 1261B at a color change upsection from light to darker green chalk at Section 207-1261B-2R-3, 83 cm. One centimeter below the contact is a purely Cretaceous nannolith assemblage with abundant *M. murus,* whereas 1 cm above is a Tertiary assemblage with abundant *C. pelagicus* (up to 7.25 µm) and some reworked Cretaceous taxa. A sample 17 cm farther upcore contains *Cruciplacolithus tenuis* (8.75 µm), moderate-sized *E. subpertusa,* and no chiasmoliths, all of which denote Zone NP2.

In Hole 1261A, the core catcher below the K/T contact (Sample 207-1261A-38R-CC) contains *M. murus* and a characteristic upper Maastrichtian assemblage assigned to Zones CC26/upper CC25, as does the subjacent core. Close to this stratigraphic level in Sample 207-1261B-3R-3, 150 cm, the abundant nannolith assemblage includes rare to few *Lithraphidites quadratus, Rhagodiscus splendens,* and some *Kamptnerius magnificus* with large flanges that indicate moderately good preservation.

Rare to few and rather poorly preserved *Uniplanarius trifidum* in Sample 207-1261B-4R-CC (roughly equivalent to Sample 207-1261A-40R-CC) signal upper Campanian Zone CC23, provided they are not reworked at this shallow end-member of the Leg 207 depth transect. This fact plus the site's relatively close proximity to the continental margin could account for the abbreviated Maastrichtian/Campanian section at this locality.

Returning to Hole 1261A, the black shales are present in Sample 207-1261A-42R-CC. In smear slides this gritty sample contains large zeolites but only moderately preserved nannofossils, including common *Eiffellithus eximius* (bar angle < 9°), *Gartnerago obliquum, Tranolithus orionatus,* and the dissolution-resistant *Marthasterites furcatus,* here apparently in acme proportions. As *Micula decussata* is absent, the sample belongs to the lower Coniacian Zone CC13. *Eiffellithus eximius* remains present, however, in the subjacent samples (Samples 207-1261A-43R-CC and 44R-CC), which are accordingly assigned to the upper Turonian Zone CC12. Nannoliths are abundant, but preservation ranges from poor to good. Preservation improves downhole in Sample 207-1261A-45R-3, 136 cm, which contains *Eprolithus apertior, Eprolithus floralis,* and *Eprolithus eptapetalus* but not *E. eximius,* and therefore belongs to the lower Turonian Zone CC11. Sample 207-1261A-46R-CC is barren of nannoliths.

Sample 207-1261A-47R-CC yields *Eprolithus octopetalus, Corollithion signum,* and *Radiolithus planus* in the absence of *E. eptapetalus* and was referred to the upper Cenomanian Zone CC10. The secondary Cenomanian marker taxon *Axopodorhabdus albianus* was encountered in Samples 207-1261A-48R-CC and 49R-CC, and the exclusively Cenomanian species *Corollithion kennedyi* is present in the equivalent Sample 207-1261B-14R-2, 1 cm, despite a rare and poorly preserved nannoflora.

A clean homogeneous massive sandstone was encountered at the base of both holes (Cores 207-1261A-51R and 207-1261B-15R and 16R). Interbedded with the sandstone in the latter core, however, is ~10 cm of apparently in situ black silty claystone. A sparse but moderately well preserved nannoflora in Sample 207-1261B-16R-1, 95 cm, contains abundant *E. turriseiffelii* (which can range in time no lower than the mid- to late Albian), along with rare *E. apertior, E. floralis,* and abundant zygoliths. This sample could be Cenomanian or late Albian in age.

Planktonic Foraminifers

Planktonic foraminifer biostratigraphy at Site 1261 was based upon core catchers in Holes 1261A and 1261B. We examined one sample per section in the Miocene and Paleocene–Cenomanian but looked only at core catchers in the extremely poorly preserved assemblages of the lower and middle Eocene. Zonal assignments are summarized in Figure **F8** and Tables **T4, T5,** and **T7.** Planktonic foraminifers from Pleistocene Zone PT1 through Cenomanian Zone KS19 were identified in Hole 1261A, along with significant breaks in the biozonation between the late Miocene and middle Eocene, the early Eocene to middle Eocene, the middle Paleocene, and the K/T boundary.

Planktonic foraminifers were present in nearly all samples but varied widely in preservation and abundance. Preservation was best in clay-rich parts of the Miocene–Pleistocene sequence and in parts of the upper Paleocene. Foraminifers were frequently filled with calcite spar in the Paleogene and Cretaceous parts of the sequence and, in the majority of cases, were also recrystallized. In contrast to other Leg 207 sites, even selective sampling of black and olive-green claystones in the Cenomanian–Santonian sequence failed to produce foraminifers that are not filled with calcite spar, and nearly all specimens have entirely recrystallized skeletons. The poor preservation of foraminifers in the Cenomanian–Santonian black shales is unfortunate because this section appears to be one of the most expanded and completely recovered intervals through the upper Turonian and Santonian obtained during

Leg 207. Foraminifer preservation in the black shales is generally sufficient for biostratigraphic studies. Foraminifers in the lower and middle Eocene hard chalks are particularly poorly preserved, often consisting of little more than pieces of rocks that are vaguely shaped like foraminifers even after ultrasonic cleaning. Slightly better preservation may be present in more clay-rich bands in the Eocene sequence, and any future foraminifer biostratigraphy should selectively sample such beds.

Sample 207-1261A-1R-1, 0–2 cm, contains modern planktonic foraminifers such as *Orbulina universa, Globigerinoides sacculifer, Globorotalia menardii, Globorotalia truncatulinoides, Neogloboquadrina dutertrei,* and *Globigerinoides ruber* (pink). Pteropods are present in Sample 207-1261A-1R-CC along with scattered grains of glauconite. Pleistocene sediments are also found in Sample 207-1261A-2R-CC.

The contact between Pleistocene sediments and those of middle Pliocene Zone PL3 occurs between Samples 207-1261A-2R-CC and 3R-CC. Both of these are short cores and are highly disturbed by rotary coring, so we did not attempt to refine the stratigraphy. Samples 207-1261A-3R-1, 49–52 cm, to 4R-CC contain *Globigerinoides fistulosus, Sphaeroidinellopsis seminulina,* and *Dentoglobigerina altispira altispira,* which indicate Zone PL3. Specimens of *G. fistulosus* have short knobs on the final chamber and are rare, as is also the case at Ocean Drilling Program (ODP) Site 925 on nearby Ceara Rise. Typical species in Zone PL3 include very well preserved *Globorotalia multicamerata, Globorotalia crassaformis, Globigerinoides extremus, S. seminulina, D. altispira,* and *G. sacculifer.*

Sample 207-1261A-5R-CC contains an assemblages characteristic of lower Pliocene Zone PL2, such as *Globorotalia margaritae, D. altispira, S. seminulina, Globorotalia plesiotumida,* and *Globigerinoides conglobatus*. *Sphaeroidinellopsis paenedehiscens, Globorotalia miocenica,* and *G. multicamerata* are regular constituents as well. As at Ceara Rise (see Chaisson and Pearson, 1997), we find *G. plesiotumida* ranges well into the lower Pliocene. These range extensions for *G. plesiotumida* suggest that this species did not evolve without branching (via anagenesis) into *Globorotalia tumida* near the Miocene/Pliocene boundary, as maintained by Malmgren et al. (1983).

Continuous coring in Hole 1261A began with Core 207-1261A-7R, which we assign to uppermost Miocene Zone M14. We did not find *Sphaeroidinella dehiscens* in any samples from this core, suggesting that all these samples predate the Miocene/Pliocene boundary. The presence of *Globoquadrina dehiscens* (whose last appearance is near the Miocene/Pliocene boundary) also suggests that Core 207-1261A-7R is of late Miocene age. Additional species in Zone M14 include *G. margaritae, Globorotalia limbata, Globigerina nepenthes, Globorotalia cibaoensis, D. altispira,* and *G. extremus*. *G. tumida* is present as low as Sample 207-1261A-9R-2, 50–54 cm.

The top of Subzone M13b, defined by the last appearance of *Globorotalia lenguaensis,* occurs in Sample 207-1261A-9R-CC. Foraminifer assemblages are characterized by *G. extremeus, D. altispira, Globigerinoides obliquus, G. menardii, G. plesiotumida,* and *S. seminulina.* Fragmentation is common. The base of Subzone M13b occurs at an abrupt contact with underlying Eocene chalks between Samples 207-1261A-20R-5, 113–116 cm, and 20R-5, 120–122 cm. Core photographs show that the Eocene/Miocene contact occurs at ~118 cm in Section 207-1261A-20R-5.

The Miocene is pervasively slumped between Cores 207-1261A-14R and 20R. Diverse clast types and colors in this section represent a spectrum of early, middle, and late Miocene ages. No pre-Miocene clasts

were found. Many clasts represent discrete foraminifer assemblages from single biostratigraphic zones. The oldest clasts representing a single zone are found near the top of the slumped section. Zone M4 (late early Miocene) is present in a dark green clast (e.g., Sample 207-1261A-14R-5, 35–36 cm) and in a light green clast (Sample 14R-5, 131–133 cm) where *Globigerinatella insueta* occurs together with *Globigerinoides bisphericus*. A white foraminifer sand clast in Sample 207-1261A-14R-5, 42–43 cm, yielded a Zone M9 (middle Miocene) assemblage with *Fohsella robusta* and *Paragloborotalia mayeri*. Other clasts in Cores 207-1261A-14R to 20R yielded faunas from Subzone M13b (upper Miocene) that are indistinguishable from those of the overlying undisturbed sedimentary sequence.

Lower in the slumped section, several clasts produce mixed assemblages with index species for Subzones M5a and M5b and Zones M8 and M11 (e.g., Sample 207-1261A-18R-2, 24–26 cm [white clast]) and Zones M4 and M11 and Subzone M13b (e.g., Sample 18R-2, 27–30 cm [chocolate brown clast]), but a few clasts also have only Zone M8–M9 assemblages (e.g., Samples 15R-CC, 16R-CC, and 17R-1, 129–131 cm), a Zone M11 fauna (e.g., Sample 17R-6, 123–127 cm [large yellowish green clast]), and one has a Subzone M5a assemblage (e.g., Sample 20R-4, 97–100 cm). Evidently there were several intervals of extensive reworking and winnowing during the middle and late Miocene before final redeposition of winnowed sediments in debris flows during Subzone M13b.

There is no clear progression in clast ages with depth at Site 1261. Nearly all clasts in Cores 207-1261A-18R to 20R contain at most a few middle or lower Miocene foraminifers mixed into an assemblage characteristic of Subzone M13b, whereas many clasts in Cores 14R to 17R produced assemblages representing single lower and middle Miocene zones. Apparently, both lower and middle Miocene strata cropped out in the vicinity of the site throughout the period of debris flow deposition. The lack of Eocene- and Oligocene-age clasts suggests that strata of these ages were not exposed in the source areas for the debris flows at any time in the Miocene.

The middle Eocene rests below a sharp contact with the overlying Miocene slumps. Sample 207-1261A-20R-5, 120–122 cm, immediately below the Miocene slumps, contains an assemblage that includes *Turborotalia pomeroli, Acarinina rohri, Globigerinatheka mexicana* (the *barri* morphotype), *Globigerinatheka index, Morozovella spinulosa,* and *Acarinina collactea,* indicating Zone P14. Similar faunas are present in Sample 207-1261A-20R-CC. In contrast, Sample 207-1261A-21R-2, 84–86 cm, contains large specimens of *Orbulinoides beckmanni,* including completely spherical forms in which the final chamber constitutes more than two-thirds of the shell. The presence of *O. beckmanni* indicates Zone P13. Sample 207-1261A-21R-CC contains an assemblage similar to that in overlying Zone P13 but without *O. beckmanni* and therefore belongs to Zone P12. Assemblages in Samples 207-1261A-22R-CC to 25R-CC are very poorly preserved and could not be dated beyond assigning them to the interval between Zones P11 and P14. Globigerinathekids in these samples show that all belong to Zone P11 or younger Eocene zones.

Zone P11 is indicated in Samples 207-1261A-26R-CC and 27R-CC, based upon the presence of *Morozovella aragonensis* and *G. index* along with *Acarinina bullbrooki, A. rohri, Guembelitriodes nuttali,* and *Igorina broedermanni*. Samples 207-1261A-28R-CC and 29R-CC are assigned to Zones P10–P11 based upon the presence of *A. bullbrooki,* which makes its first appearance near the Zone P9/P10 boundary. In contrast, Sample

207-1261A-30R-CC contains a limited assemblage of *M. aragonensis*, *Acarinina pentacamerata,* and *Acarinina aspensis,* which probably reflects Zone P9, but could be younger (possibly Zone P10).

There is a hiatus between Samples 207-1261A-30R-CC and 31R-CC, as the succession crosses abruptly from Zone P9–P10 to P7. Species representative of Zone P7 include *Acarinina quetra, M. aragonensis, Morozovella lensiformis, Morozovella formosa,* and *Acarinina coalingensis*. Zone P7 is probably separated from the underlying succession by another hiatus because Sample 207-1261A-32R-CC contains the species *Morozovella velascoensis,* which is indicative of the top of Zone P5.

The P/E boundary occurs in Zone P5 at Section 207-1261A-33R-4, 130 cm. Typical assemblages in Zone P5 include *M. velascoensis, Morozovella aequa, Acarinina soldadoensis, A. coalingensis, Morozovella subbotinae,* and *Morozovella occlusa*. The lower boundary of Zone P5 could not be determined precisely owing to the absence of *Globanomalina pseudomenardii* in very poorly preserved assemblages from Samples 207-1261A-33R-CC and 34R-CC. Large flattened globanomalinids are present beginning in Sample 207-1261A-35R-1, 50–54 cm, and may indicate the top of Zone P4, but the poor preservation makes it difficult to confirm this zonal assignment. The base of Zone P4 occurs between Samples 207-1261A-36R-5, 50–54 cm, and 36R-6, 50–54 cm. These earliest assemblages in Zone P4 are nicely preserved, in contrast to virtually all of the remaining Paleocene and Cretaceous faunas, and include *M. velascoensis* (with extremely well developed umbilical muricae), *Morozovella acutispira, Acarinina subspherica,* and *Morozovella apanthesma* as well as very large specimens of *Igorina albeari*. A similar assemblage is present in Sample 207-1261A-36R-6, 50–54 cm, but lacks acarininids.

The Danian/Selandian contact and most of the upper Danian biozones are present in a condensed sequence in Hole 1261A. Subzone P3b is present from Sample 207-1261A-36R-6, 50–54 cm, to 37R-1, 50–54 cm, whereas Samples 37R-2, 50–54 cm, to 37R-3, 50–54 cm, may belong to Subzone P3a because they do not appear to contain *I. albeari* or *M. velascoensis*. However, preservation is very poor so we can only recognize Zone P3 (undifferentiated), pending further study. The boundary between Zones P3 and P2 occurs between Samples 207-1261A-37R-3, 50–54 cm, and 37R-4, 50–54 cm, accompanied by a distinct change in foraminifer assemblage to one dominated by *Praemurica uncinata* and *Morozovella praeangulata,* with subordinate *Praemurica inconstans, Parasubbotina varianta, Subbotina triloculinoides,* and *Parasubbotina pseudobulloides*.

The K/T boundary is apparently unconformable at Site 1261. Samples 207-1261A-37R-CC, 24–29 cm, and 207-1261B-2R-CC both yielded upper Maastrichtian faunas, although a few Danian calcareous nannofossils were found in Sample 37R-CC (see **"Calcareous Nannofossils,"** p. 11). A series of samples was taken in Core 207-1261B-2R, and these showed that faunas representing Danian Zone P2 with *P. uncinata* are present from the top of Core 207-1261B-2R to Sample 207-1261B-2R-3, 78–79 cm, where a mixed assemblage of Zones P2 and KS31 is observed. The interval between 70 and 80 cm in Section 207-1261B-2R-3 is lithostratigraphically similar to Sample 37R-CC and consists of pyrite-rich interbeds of light greenish gray chalk and darker greenish chalk that represent the eroded remains of the K/T boundary sequence.

The Maastrichtian–Campanian succession is highly condensed and probably contains undocumented hiatuses. Uppermost Maastrichtian Zone KS31 is recorded in Samples 207-1261A-37R-CC and 38R-CC. Zone KS31 is represented by poorly preserved foraminifer assemblages including *Abathomphalus mayaroensis, Contusotruncana contusa, Rugoglo-*

bigerina rugosa, Globotruncana aegyptiaca, and *Globotruncanita stuarti*. Sample 207-1261A-39R-CC may belong to Zone KS29 of the upper Campanian because it lacks *C. contusa* and *Gansserina gansseri* and has a very poorly preserved fauna of *G. aegyptiaca, Globotruncanella havanensis,* and *R. rugosa,* similar to Campanian assemblages at other Leg 207 sites. Finally, Sample 207-1261A-40R-6, 55–60 cm, yields only a few poorly preserved specimens of *Heterohelix globulosa* and *Heterohelix striata* that do not provide a conclusive zone assignment. This nearly barren sample contains a few radiolarians and benthic foraminifers similar to upper Campanian samples from other sites drilled during Leg 207.

Black shale in Sample 207-1261A-41R-CC contains a moderately species-rich assemblage of *Dicarinella concavata, Contusotruncana fornicata, Whiteinella inornata, Whiteinella brittonensis, Dicarinella canaliculata,* and *Marginotruncana pseudolinneiana,* representing Coniacian/Santonian Zones KS24–KS23. The overlap of *C. fornicata* and *D. concavata* indicates that these samples cannot be older than the middle Coniacian but could be as young as Santonian. Calcareous nannofossil evidence also suggests that the upper part of the black shale sequence is primarily Coniacian or lowermost Santonian in age (see **"Calcareous Nannofossils,"** p. 11). Coniacian foraminifers are found in Samples 207-1261A-42R-5, 5–8 cm, and 42R-CC and include *W. inornata, W. archaeocretacea, Marginotruncana sinuosa,* and *Archaeoglobigerina blowi,* which probably represents Coniacian Zone KS23, although the zone markers are absent.

The Turonian/Coniacian boundary is in the vicinity of Samples 207-1261A-43R-CC and 44R-CC, both of which contain *W. inornata* and *W. archaeocretacea,* as well as a diverse assortment of clavate and stellate planktonic foraminifers such as *Hastigerinelloides watersi* and *Hastigerinelloides alexanderi*.

Dicarinella hagni in Sample 207-1261A-44R-CC and *Dicarinella primitiva* in Sample 43R-CC suggest uppermost Turonian Zone KS22 and lower Coniacian Zone KS23, respectively, in the absence of the zone markers, *D. concavata* and *Helvetoglobotruncana helvetica*. All foraminifers in the core catchers and samples taken from sections (typically one per section) yielded foraminifers with recrystallized skeletons and chambers filled with calcite spar.

The upper part of the Turonian includes an abundance of whiteinellids, such as *W. inornata* with weak imperforate bands, *W. archaeocretacea,* and *Whiteinella baltica,* along with the nearly ever-present *Hedbergella delrioensis*. The clavate species *Clavihedbergella amabilis, H. watersi,* and *H. alexanderi* are also rare components. Low species diversity foraminifer assemblages range from Sample 207-1261A-45R-3, 136 cm, to 47R-CC and consist of little more than *H. globulosa, Heterohelix moremani, H. delrioensis, W. archaeocretacea,* and *W. baltica,* which could indicate either a Turonian or latest Cenomanian age. Foraminifers are often small (<180 µm) and rare in Samples 207-1261A-46R-CC to 47R-1, 132–133 cm, which we believe may approximate the Cenomanian/Turonian boundary.

Cenomanian assemblages can be found between Sample 207-1261A-48R-CC and 50R-CC. *Rotalipora greenhornensis* in Sample 207-1261A-48R-CC indicates Zone KS19 along with *H. moremani, Globigerinelloides* sp., *H. delrioensis,* and *Praeglobotruncana gibba*. Whiteinellids range as low as Sample 207-1261A-50R-CC and indicate that the black shales above the first of the quartz sandstone beds near the base of Hole 1261A cannot be older than the middle of Zone KS19. A black silty claystone sample interbedded between quartz sandstone in Sample 207-1261B-15R yielded only a few well-rounded quartz grains.

Radiolarians

The radiolarian record at Site 1261 consists of long barren intervals and, in general, poor preservation. Core catcher samples were processed systematically only from Hole 1261A. The Pleistocene and Pliocene are entirely barren of radiolarians. Only two samples of the late Miocene interval (Samples 207-1261A-10R-CC and 11R-CC) contained some non–age diagnostic radiolarians. In the Paleogene, radiolarians are present nearly throughout the entire interval but generally are poorly preserved. The consistent occurrence of *Dictyoprora mongolfieri* and species of the *Lithocyclia ocellus* group in Samples 207-1261A-20R-CC through 27R-CC allows assignment of this interval to Zones RP11 to RP15, as the evolutionary transition of the latter species to the *Lithocyclia aristotelis* group is approximately synchronous with the base of Zone RP16. The presence of *Sethochytris triconiscus* in Sample 207-1261A-22R-CC and *Eusyringium lagena* in Sample 26R-CC allows recognition of Zones RP12–RP14 and RP14–RP15, respectively.

Radiolarian occurrence is very patchy in the Cretaceous. In the undistinguished Campanian–Maastrichtian interval, a few poorly preserved radiolarians are present in Sample 207-1261A-40R-CC. Preservation improves in the Cenomanian–Turonian interval (Sample 207-1261A-43R-CC), but the rare radiolarians encountered were not age diagnostic.

PALEOMAGNETISM

Shipboard paleomagnetic measurements from the two holes at Site 1261 were disappointing, but shore-based thermal demagnetization of minicores revealed the main successions of polarity chrons bound by hiatuses. Maastrichtian Chrons C31r–C29r, early Paleocene–early Eocene Chrons C27n–C24r, and middle Eocene Chrons C21r–C19r were delimited.

Shipboard and Shore-Based Procedures and Data Filters

Details are given in **"Paleomagnetism,"** p. 16, in the "Explanatory Notes" chapter of the standard shipboard analysis procedures using the pass-through cryogenic magnetometer, of the filtering and polarity interpretation procedures of this shipboard data, and of the shore-based progressive demagnetization of discrete minicores. Shipboard measurements of natural remanent magnetization and after 10- and 15-mT alternating-field (AF) demagnetization steps were made at 5-cm intervals on all archive halves longer than 15 cm from Cores 207-1261A-7R through 40R and from Cores 207-1261B-2R through 5R, with the exceptions of most cores in the Miocene debris flow. In general, the 10-mT step was effective in removing steep downward overprints induced by the drilling process and the 15-mT step was usually needed to resolve trends toward negative inclination directions but also reduced the magnetic intensity of the majority of the sediment intervals to the background noise level of the cryogenic magnetometer. As at the other Leg 207 sites, we did not analyze the black shale cores rather than partially removing the magnetization of these sediments without obtaining any useful shipboard information. These black shale intervals typically display magnetic intensities near the background noise level of the ship-

board cryogenic magnetometer and were deposited during the Cretaceous Long Normal Polarity Superchron C34n.

Shipboard identification of polarity zones through nearly half of the succession was not possible because of weak magnetization near the noise limit of the cryogenic magnetometer, secondary overprints associated with reddish coloration that could not be removed by shipboard AF demagnetization, and several intervals characterized by reduced core recovery. Therefore, we took a set of oriented paleomagnetic cylinders from every second section (3-m spacing) of Eocene–Campanian sediments (Cores 207-1261A-20R through 40R, and 207-1261B-2R through 4R) for combined progressive AF and thermal demagnetization at the magnetic-shielded facility at the University of Munich, Germany. These shore-based measurements enabled resolution of removed and characteristic components of magnetization and significantly modified the tentative shipboard polarity interpretations from all facies (Table T8).

T8. Polarity and characteristic directions, p. 85.

Paleomagnetic Behavior and Interpretations of Magnetostratigraphy

The generalized stratigraphy of sediment facies, biostratigraphic ages, and magnetization characteristics of Site 1261 from the shipboard pass-through cryogenic magnetometer are summarized in Figure F9. Intervals of greenish white to gray chalk are characterized by very weak magnetization, and nearly half of the measurements after the 15-mT demagnetization step for such intervals were below the 3×10^{-5} A/m background noise level of the magnetometer system. In contrast, the normal polarity overprint dominating the strongly magnetized Paleocene and Miocene clay-rich facies did not respond to AF demagnetization. The polarity zones of all facies were resolved by applying thermal demagnetization to minicores, followed by interpreting the polarity of each minicore from an examination of the movement of its magnetic vector during progressive demagnetization (see "Paleomagnetism," p. 16, in the "Explanatory Notes" chapter).

F9. Shipboard paleomagnetic data, p. 51.

Late Miocene and Pliocene

Cores 207-1261A-7R through upper 14R consist of a gray silty claystone of late Miocene (M13, NN11) to earliest Pliocene (PL1) age. This facies had a uniformly strong magnetization that averaged 5×10^{-5} A/m after 10-mT demagnetization. The 10-mT step was effective in removing a steep downward drilling-induced magnetic overprint, but application of an additional 15 mT did not significantly change the intensity or directions (Fig. F9). This resistance to AF demagnetization, coupled with the near-continuous normal polarity inclinations during an interval of time that should be characterized by frequent magnetic reversals, implies that the gray claystone probably has a persistent overprint that is perhaps carried by goethite-type minerals. Thermal demagnetization >200°C is generally required to remove overprints carried by goethite, but this interval was not a priority for our shore-based program of measurements.

Debris flows and redeposited material into upper Miocene (nannofossil Zone NN10) host sediments compose the majority of Cores 207-1261A-15R through 20R. We measured only a few sections in this interval, primarily the large 45° tilted block of light green chalk of the middle Miocene (nannofossil Zone NN6) spanning all of Core 207-1261A-16R and uppermost Core 17R. Frequent magnetic reversals are charac-

teristic of the original depositional age of this block (Serravallian stage). Intact pieces in this 10-m-thick chalk display well-defined polarity reversals with simultaneous 180° changes of declination and inclination. It is rather ironic that the best polarity data obtained from shipboard measurements taken during Leg 207 are from a displaced olistrostrome. In all other units, shore-based progressive thermal demagnetization of minicores was required to adequately resolve magnetic polarity zones.

Eocene

The light greenish gray to medium gray lower–middle Eocene chalk was very weakly magnetized, with an average magnetic intensity of ~3 × 10^{-5} A/m after the 15-mT demagnetization step. Therefore, only a few intervals were significantly above the effective background noise of the shipboard magnetometer (3 × 10^{-5} A/m) (Fig. F9). The shore-based cryogenic magnetometer enabled an additional order of magnitude in sensitivity, and we were able to adequately resolve the polarity patterns from this facies (Fig. F10).

The uppermost meters of the Eocene yielded a dominance of normal polarity, which is tentatively assigned to Chron C18n from its coincidence with foraminifer Zones P13 and P14. Below a gap in paleomagnetic sampling, we resolved the complete succession of Chrons C19r through probably C20r and perhaps the underlying Chrons C21n and C21r. A hiatus at the early/middle Eocene boundary is indicated by biostratigraphy, which probably encompasses Chrons C22n and C22r. A sediment piece recovered from the interval spanned by Core 207-1261A-31R has normal polarity, which is suggested by its biostratigraphic age to correspond to a portion of Chron C23n. Another hiatus in the middle of the early Eocene probably spanned much of Chrons C23r and C24n, and the lower lower Eocene section at Site 1261 is entirely within Chron C24r.

Paleocene

The Paleocene medium–light gray clayey chalk had a slightly stronger magnetization (averaging ~5 × 10^{-5} A/m), but only positive inclinations were resolved by AF demagnetization (Fig. F9). Thermal demagnetization successfully removed this normal polarity overprint. The upper Paleocene section contains the record of lower Chron C24r and Chrons C25r–C27n (Fig. F10).

Campanian and Maastrichtian

The greenish gray clayey chalk with light–dark cycles of Maastrichtian and Campanian age is characterized by weak intensity and susceptibility (Fig. F9). The magnetic signals from many of the minicores from both holes were commonly reduced to near the noise level of the Munich cryogenic magnetometer upon heating >200°C, and polarity interpretations were commonly uncertain. When the data from the two holes are merged using the composite depth (mcd), then general magnetic characteristics and biostratigraphic constraints suggest Chrons C30n–C31n and the underlying Chron C31r (Fig. F10).

F10. Shore-based magnetostratigraphy, p. 52.

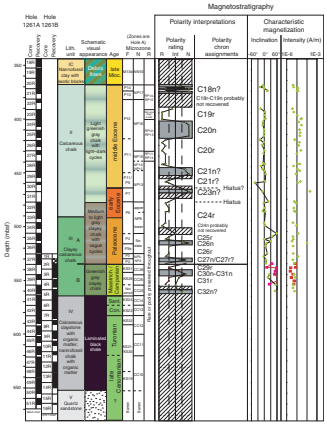

COMPOSITE DEPTHS

Coring at Site 1261 extended to a total depth of 674 mbsf. The interval from just above the K/T boundary through the Cretaceous black shales (below ~525 mcd) was the only interval targeted for overlap and composite section construction. Magnetic susceptibility, gamma ray attenuation (GRA) bulk density and noncontact resistivity (NCR) data were collected with the multisensor track (MST) at 2.5-cm intervals on all whole-core sections from Holes 1261A and 1261B. NGR data were collected at 7.5-cm intervals on all whole cores from Holes 1261A and 1261B. Spectral reflectance data were collected at 2.5-cm intervals on all split cores. GRA bulk density data provided the most reliable core-to-core comparisons and were supplemented by NGR and magnetic susceptibility data.

Composite Section

The depth offsets that compose the composite section for Holes 1261A and 1261B are given in Table **T9.** The quasi-periodic variability of the claystone and chalks/limestone composing the black shales resulted in strong signal-to-noise ratios in both the GRA bulk density (Fig. **F11**) and NGR data sets. These data sets, combined with good RCB recovery over a significant portion of the black shale interval, allowed for the construction of a semicontinuous composite section from ~550 to 650 mcd.

T9. Composite depth offsets, p. 87.

F11. Composite and spliced GRA bulk density, p. 54.

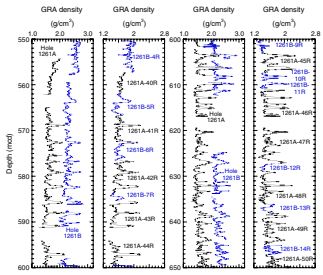

T10. Splice tie points, p. 88.

SEDIMENTATION RATES

Age-Depth Model

An age-depth model was constructed for Hole 1261A using the estimated age and depth uncertainty for biostratigraphic datums (Table

T11) and paleomagnetic data (Table T12). Spot coring in the upper 237 m at this site limited stratigraphic resolution in this part of the hole, and foraminiferal identifications were hampered by poor preservation through much of the section (see **"Biostratigraphy,"** p. 10). Further, shipboard paleomagnetic data yielded magnetochron estimates only for the Campanian–Maastrichtian interval (see **"Paleomagnetism,"** p. 19). Thus, sedimentation rate calculations depend most heavily on nannofossil datums. Despite these limitations, five intervals of relatively constant sedimentation separated by hiatuses, mass flows, or condensed intervals are apparent in the age-depth plot (Fig. F12).

T11. Biostratigraphic datums and sedimentation rates, p. 89.

T12. Campanian–Maastrichtian magnetostratigraphic datums, p. 90.

F12. Age-depth plot, p. 55.

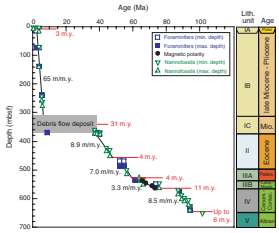

Sedimentation Rates and Hiatuses

The upper 368 m of section at Site 1261 is unique among the five sites drilled during Leg 207. The youngest interval is Pleistocene in age and was too thin relative to sampling density for a meaningful sedimentation rate to be calculated. It is separated by a gap of ~3 m.y. from an interval of Pliocene–upper Miocene nannofossil clay and nannofossil ooze, where sedimentation rates (at 65 m/m.y.) were the highest calculated for any interval recovered during Leg 207. This interval of high sedimentation rates sits above a thick series of mass flow deposits, which occupy a stratigraphic position corresponding to a gap in pelagic sediment of >30 m.y.

Below the mass flow deposits, sedimentation patterns are similar to those seen at the other four sites drilled during Leg 207. The middle Eocene is represented by calcareous chalks, and calculated sedimentation rates are close to 9 m/m.y. Chalk deposition ends downcore at a hiatus with a duration of ~4 m.y. Below this hiatus, sediments are richer in clay than above, but early Eocene–early Paleocene sedimentation rates (7.0 m/m.y.) were similar to those in the middle Eocene. This interval ends at another ~4-m.y. hiatus, which includes the basal Danian and K/T boundary interval. Sedimentation rates are markedly lower below this hiatus than above it. At 3.3 m/m.y., the sedimentation rate in this interval is the lowest rate calculated for the Campanian–Maastrichtian interval among the five Demerara Rise sites. Pelagic deposition ends downcore in a hiatus and/or condensed interval of ~11 m.y. that spans the lower Campanian, the Santonian, and perhaps part of the upper Coniacian. Sedimentation rates in the subjacent black shale facies are 8.5 m/m.y., a rate at the high end of those found in this interval during Leg 207. The only datum below the black shale interval yields a maximum age of late Albian (see **"Biostratigraphy,"** p. 10), which is consistent with the age of lithostratigraphic Unit V at other sites. If accurate, this age suggests a hiatus of ~6 m.y. separates the black shale from the subjacent sandstones.

Mass Accumulation Rates

Average mass accumulation rates (MARs) were calculated from linear sedimentation rates (LSRs) discussed above and the average of the dry bulk density measured on discrete samples for each interval of apparently constant sedimentation. MAR calculations remove the influence of compaction on LSR calculations and give a better indication of the quantity of accumulating sediment. Comparing MAR rates, though, does not change the conclusion that sedimentation rates were very high during the Pliocene and, hiatuses notwithstanding, slowed pro-

gressively from the middle Eocene–Campanian. Finally, MARs were relatively high during deposition of black shales (Table T13).

T13. LSRs and MARs, p. 91.

ORGANIC GEOCHEMISTRY

Concentrations of inorganic carbon and TOC were determined on sediments from Holes 1261A and 1261B. Organic matter atomic carbon/nitrogen (C/N) ratios and Rock-Eval pyrolysis analyses were employed to assess the type of organic matter contained in the sediments. Routine monitoring of interstitial gas contents of the two holes was performed for drilling safety and pollution prevention, and the possibility of microbial activity was evaluated from headspace gas contents of Hole 1261B.

Inorganic and Organic Carbon Concentrations

Concentrations of inorganic carbon vary from 0.1 to 11.7 wt% at Site 1261 (Table T14). These concentrations are equivalent to 0.9–93 wt% $CaCO_3$, assuming that all of the carbonate is calcite or aragonite. All five lithostratigraphic units at this site (see "Lithostratigraphy," p. 3) contain carbonate but show differences in average concentrations related to their facies. In Subunits IA and IB, carbonate concentrations range between 15 and 30 wt%, whereas Subunit IC shows a wider scatter between 25 and 78 wt%. Unit II is composed of calcareous chalk, representing the most carbonate-rich unit at Site 1261, with most samples clustering close to the average concentration of 75 wt% carbonate. The clayey calcareous chalks of Unit III show a wider scatter of carbonate contents, between 17 and 77 wt% (average = 47 wt%). The black shales in Unit IV average ~43 wt% carbonate but have a marked layer-by-layer scale variation between 1 and 97 wt%. This variability is associated with lithologic changes, mainly the alternating abundant calcite-enriched laminae between clay-dominated black shale intervals. From Unit V, only one sample (Sample 207-1261B-16R-1, 99–100 cm), from a short, dark, clay-rich interval intercalated with the dominating sandy lithofacies, was analyzed, yielding 3.8 wt% carbonate.

T14. Inorganic and organic carbon and total nitrogen, p. 92.

There is a wide range of TOC concentrations among the five lithostratigraphic units at Site 1261. The sediments of Units I–III contain <0.5 wt% TOC (average = 0.1 wt% TOC) (Table T14). The sediments of Unit IV have an average TOC concentration of 9.3 wt% but vary widely (0.4–16.1 wt%). The TOC of Sample 207-1261B-16R-1, 99–100 cm, from Unit V, is 1.0 wt%. However, this clay-rich sample is not representative of this sandstone unit.

Organic Matter Source Characterization

Atomic $C_{organic}/ N_{total}$ ratios were employed to help identify the origin of organic matter in sediments at Site 1261. Most of the C/N values in organic-lean Units I–III are low (Table T14) and are below the range typical of fresh algal organic matter (4–10) (Meyers, 1997). These values are probably an artifact of the low TOC concentrations, combined with the tendency of clay minerals to absorb ammonium ions generated during degradation of organic matter (Müller, 1977). Some values are artificially elevated because the low amounts of C and N are near the limits of detection of the elemental analyzer.

The C/N ratios of the black shales in Unit IV average 34.3, which is a value typical of land-plant organic matter but is also common to Cretaceous black shales (Meyers, 1997). A van Krevelen–type plot of hydrogen index (HI) and oxygen index (OI) values (Fig. F13) indicates that the black shales in Unit IV contain Type II (algal) organic matter. High HI and low T_{max} values (average = 397°C) like those found in the black shales (Table T15) are characteristic of thermally immature, relatively well preserved marine organic matter (Espitalié et al., 1977; Peters, 1986). Consequently, the elevated C/N values, which mimic those of land-derived organic matter, are probably the result of partial alteration of marine organic matter. A likely scenario is that nitrogen-rich components are preferentially degraded during sinking of organic matter to the seafloor, thereby elevating the C/N ratio of the surviving organic matter (Twichell et al., 2002).

Organic matter in Unit V is represented by only one value of 1.0 wt% TOC (Table T14). Considering this low TOC yield in comparison to the black shales in Unit IV, the C/N ratio of 38.3 could indicate land-plant derived organic matter. Rock-Eval HI and OI values (Fig. F13) place this sample into the transitional field between Types II and III kerogen, indicating a mixture of predominately algal and some terrigenous organic matter. The T_{max} of this sample is 412°C and is therefore slightly higher than the average T_{max} of the samples from Unit IV. This difference can be explained by either the mixed organic matter type or overall poorer conditions of organic matter preservation in Unit V.

F13. Rock-Eval van Krevelen–type diagram, p. 56.

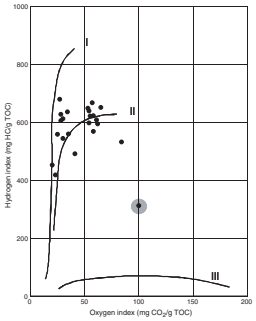

T15. Rock-Eval pyrolysis analyses, p. 94.

Interstitial Gas Contents

Concentrations of interstitial gases in lithostratigraphic Units I–III at Site 1261 were generally low but slightly higher in comparison to other Leg 207 sites. The gas concentrations increase dramatically in Units IV and V. In these units, gas voids were not observed, but most cores from Unit IV showed active degassing when brought on deck. Small gas bubbles were visible through the core liner for several minutes until the cores adjusted to surrounding warm temperature and low pressure conditions. When the cores were cut after several hours, some still yielded a large amount of gas that was liberated during the cutting process.

The results of the headspace and microbial gas analysis are very similar (Fig. F14). Methane (C_1) concentrations rose above background values (>3 ppmv) in lithostratigraphic Unit I. After a concentration maximum (10 ppmv) was reached at 251 mbsf, methane yields gradually returned to background values until 394 mbsf. Although the C_1 concentrations in this specific interval are very low, the presence of some methane is consistent with a decrease in interstitial sulfate concentrations (refer to "Inorganic Geochemistry," p. 26). Interstitial sulfate is known to generally inhibit microbial methanogenesis (Claypool and Kvenvolden, 1983), and sulfate disappeared completely from the pore water at ~250 mbsf in Hole 1261A.

Below 400 mbsf, the methane concentrations continuously increased to reach 19,300 ppmv at the base of Unit III (562 mbsf). When the top of the black shales in Unit IV was penetrated at ~564 mbsf, methane increased suddenly to 62,000 ppmv and ethane (C_2) was recorded for the first time in concentrations >100 ppmv (Table T16). The methane concentrations stayed elevated (average = 50,000 ppmv) through the black shale unit, reaching a prominent maximum of 111,000 ppmv at 586 mbsf. The last sample from Unit IV at 653 msbf contained 53,800 ppmv

F14. Headspace gas concentrations, p. 57.

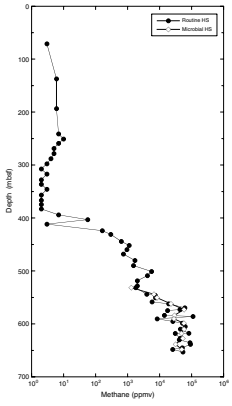

T16. Headspace analysis, p. 95.

methane. The two cores from Unit V were not suitable for gas monitoring because of their quartz sandstone lithology.

The natural gas analyzer was employed to monitor the higher molecular weight volatile compounds butane (C_4), pentane (C_5), and hexane (C_6) in the black shale unit and to augment the routine monitoring. These three compounds are usually not considered to result from microbial activity (Claypool and Kvenvolden, 1983), and their presence might therefore indicate thermogenic gas. They were found only in traces (<5 ppmv) at Site 1261. The methane/ethane (C_1/C_2) ratio dropped from >1000 ppmv (Table **T16**) above Unit IV to somewhat lower values in the black shales. The ratio stayed at relatively high levels (~500 ppmv) throughout the middle of the unit and increased at the base. The overall depth trend of the C_1/C_2 ratio in Unit IV and the complete disappearance of interstitial sulfate just above the unit (see **"Inorganic Geochemistry,"** p. 26) strongly suggest an exclusively microbial origin for the gas at this site. As neither the organic matter concentration nor its quality (the lipid richness of organic matter expressed by its average HI values) are elevated with respect to other Leg 207 sites, the relatively high methane concentrations observed at Site 1261 can be most likely explained by higher lithostatic pressure.

INORGANIC GEOCHEMISTRY

Interstitial water from 24 samples was collected at Site 1261: 22 from Hole 1261A (2.95–638.31 mbsf) and 2 from Hole 1261B (619.37–648.00 mbsf). The samples from both holes were taken to constitute a single depth profile. However, slight differences in lithology may cause minor breaks in concentration-depth gradients of some chemical parameters. Chemical constituents were determined according to the procedure outlined in **"Inorganic Geochemistry,"** p. 31, in the "Explanatory Notes" chapter. Alkalinity was not determined in five samples because of low yields of interstitial water. Results of the chemical analyses are presented in Table **T17.**

T17. Pore water analyses, p. 96.

Organic Matter Consumption

Pore water chemistry at Site 1261 is dominated by processes in two depth regimes: the rapidly sedimented Unit I (65 m/m.y.) (see **"Sedimentation Rates,"** p. 22) and the organic matter–rich black shale sequence of Santonian–Cenomanian age (lithostratigraphic Unit IV [~564–654 mbsf]). Unlike the previous sites drilled on Demerara Rise, the pore water sulfate profile at Site 1261 approaches zero at ~200 mbsf in the middle Pliocene section of Subunit IB (see Fig. **F15F**). At the base of Subunit IC and in Unit II, sulfate returns to slightly higher values (<1.5 mM) before zero concentrations are attained a second time in and below Subunit IIIA. These observations suggest that the organic matter–rich Unit IV provides a suitable substrate for ongoing microbial activity at depth and that sulfate reduction is occurring in the upper 200 m of the sedimentary column. Most of the hydrogen sulfide produced by sulfide reduction at Site 1261 must be trapped as iron sulfide because we detected no smell of H_2S gas. The second decrease of residual interstitial sulfate may be related to methane diffusing upward from the black shales. The source for metabolic activity is possibly anaerobic methane oxidation (Borowski et al., 1999; Boetius et al., 2000) because higher alkalinities are found above the black shales (Fig. **F15E**).

F15. Pore water chemical profiles, p. 58.

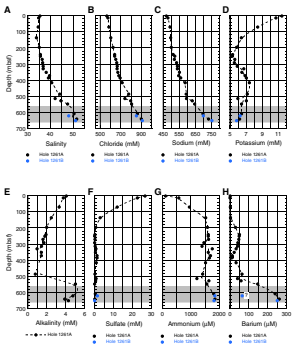

The reducing character of the clay-rich and therefore Fe-rich Unit I sediments is also demonstrated by measurable quantities of dissolved Fe (Fig. F15O). Below 300 mbsf, dissolved Fe concentrations are below the detection limit. The same is true for Mn, where only trace quantities are detected in lithostratigraphic Units II–IV (Fig. F15P). Therefore, both redox-sensitive metals not only reflect the generally reducing character of the sediments but also the difference between the clay contents of Unit I and the remaining units. We interpret the low Mn content of Unit IV to indicate complete syndepositional removal under highly reducing conditions (see "Inorganic Geochemistry," p. 24, in the "Site 1257" chapter; "Inorganic Geochemistry," p. 26, in the "Site 1258" chapter; "Inorganic Geochemistry," p. 30, in the "Site 1259" chapter; and "Inorganic Geochemistry," p. 26, in the "Site 1260" chapter).

Sulfate depletion is accompanied by an increase in ammonium (Fig. F15G), a common respiration product of organic matter consumption. Ammonium concentrations are high throughout lithostratigraphic Units II–IV and decrease from ~100 mbsf in Subunit IB toward the sediment/seawater interface. The highest ammonium concentrations are attained in the black shales and imply that Unit IV is characterized by continuing microbial activity.

The complete absence of sulfate in two different depth intervals promotes another phenomenon typically seen in organic matter–rich sediments, the mobilization of Ba. Increases in Ba concentrations (Fig. F15H) are governed by barite solubility (Church and Wolgemuth, 1972) and are prone to even slight contamination by seawater sulfate. For this reason, we have marked one data point with a question mark (interval 207-1261B-11R-2, 147–157 cm) because we suspect some contamination with seawater sulfate from drilling fluid. Assuming that the sulfate content (1.4 mM) originates from a seawater admixture, we estimate the level of contamination to be ~5%. The highest dissolved Ba levels attained in Unit IV are >250 µM. The second maximum at ~250 mbsf is smaller in magnitude but closely follows near-zero sulfate levels in this depth interval. It is noteworthy that elevated Ba levels are still present in Subunit IIIB, where authigenic barite crystals of millimeter to centimeter scale are frequently observed (see "Lithostratigraphy," p. 3). Similar sedimentological and mineralogical relationships are reported elsewhere (Brumsack, 1986; Torres et al., 1996).

The downhole interstitial water concentration profile for Mg (Fig. F15K) shows an S-shaped trend: a pronounced decrease toward 200 mbsf (the depth interval where sulfate reaches zero values), increasing concentrations down to Subunit IIIB, followed by a decrease in Unit IV. The Mg profile resembles the K profile, which is also indicated by the good correlation between Mg/Cl and K/Cl ratios (Fig. F16). We assume that the Mg distribution is influenced more by clay mineral interaction than dolomitization processes, except for Unit IV, where dolomite formation cannot be excluded. From the sediment/water interface to the top of lithostratigraphic Unit IV, the downhole interstitial water concentration profile for Ca appears totally decoupled from Mg (Fig. F15I). Instead, the pore water Ca depth profile more closely resembles the Sr profile, particularly in the upper 250 mbsf (Subunits IA and IB) (Fig. F15J), and a good linear correlation of the two elements is shown in Figure F17. Between ~300 and 400 mbsf, Sr concentrations continue to increase downhole whereas Ca concentrations remain essentially constant. We interpret the decoupling of these two parameters in terms of carbonate precipitation supported by the low alkalinity values and poor preservation of nannofossils and foraminifers documented within and

F16. Mg/Cl vs. K/Cl, p. 61.

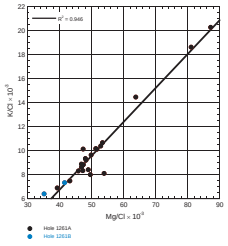

F17. Sr vs. Ca, p. 62.

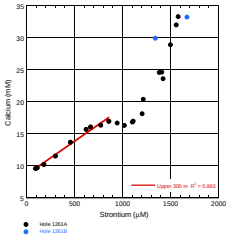

below Unit II (see "Biostratigraphy," p. 10) (Fig. F15E). Chloride normalization shows essentially the same trend (Fig. F15S).

The Li profile (Fig. F15L) shows seawater concentrations down to 290 mbsf (the base of clay-rich Subunit IB). Below this depth, values dramatically increase to 300 µM in Unit III and remain essentially constant to the base of Unit IV. Li/Cl ratios show the same trend (Fig. F15U). We have no firm explanation for this dissolved Li profile or for those seen at the other Leg 207 sites. Speculative alternatives for Site 1261 include the following:

1. The release of Li in Unit III sediments and fixation in the clay-rich base of Subunit IB and
2. The existence of a relation between Li and the degree of carbonate recrystallization/precipitation, which is most intense in Unit II sediments and below, possibly related to the loss of specific surface area of the recrystallizing calcite.

The B profile shows a slight decrease in clay-rich Unit I down to 370 mbsf (Fig. F15M). Below this depth interval, B concentrations increase in Unit II and show minimum values in Unit III, which is also characterized by elevated clay contents. Within the black shales (lithostratigraphic Unit IV), B concentrations attain maximum values. The B profile seems to reflect adsorption processes by clays (Brumsack and Zuleger, 1992). A relationship to biogenic Si may be deduced from the similar shape of the B profile.

Dissolved Si concentrations decrease with depth down to ~370 mbsf (Fig. F15N), reflecting the absence of biogenic Si in Unit I (see "Biostratigraphy," p. 10). A strong increase in Si is seen in the upper part of lithostratigraphic Unit II, whereas values are lower in Unit III. Whether this is because of opal-A/opal-CT transformation (Dixit et al., 2001) or the absence of biogenic Si remains unanswered. Generally, the Si profile reflects the abundance of siliceous tests and may be highly variable because of chert or silicate mineral formation.

Lithostratigraphic Unit IV as an Aquifer for Brines

A prominent feature of the interstitial water chemistry at Site 1261 that is similar to Sites 1257 and 1259 is the increase in Cl concentration with depth to >60% relative to standard seawater (Fig. F15A–F15C). This increase is paralleled by Na, but the Na/Cl ratio decreases toward Unit IV, from seawater values of 0.86 to below 0.82 (Fig. F15V). The maximum salt content is located at the base of Unit IV at ~648 mbsf. Unfortunately, we were unable to retrieve an interstitial water sample from below the black shale sequence, but based on our findings at Site 1257 we assume that Unit IV may act as an aquifer for the brine. We cannot exclude that a fraction of the Ca, Sr, and Li (Fig. F15S–F15U) is also associated with this brine because their element/Cl ratios are essentially constant in the lowermost samples.

In summary, the interstitial water profiles from this site primarily reflect ongoing organic matter diagenesis and microbial activity in the rapidly deposited lithostratigraphic Unit I and the black shales, carbonate diagenesis, and the dissolution of biogenic silica. A small influence of ash alteration cannot be excluded, but further shore-based isotopic studies are required to rule out this possibility. In contrast to the findings at Site 1257 and in agreement with Site 1259, we cannot com-

pletely rule out the existence of underlying, deeper-seated evaporite sequence, as suggested at Site 144 by Waterman et al. (1972).

PHYSICAL PROPERTIES

Site 1261 differed significantly from the other four sites drilled during Leg 207. A 360-m Neogene unit of clayey nannofossil-rich material lays atop expanded highly lithified middle Eocene chalks and limestones. The bottom 60 m of the Neogene unit was a large debris flow. Below the expanded middle Eocene deposits, the lithology of Site 1261 begins to reflect that of the other sites (see "Lithostratigraphy," p. 3).

Physical property measurements at Site 1261 were conducted on whole cores, split cores, and discrete samples. Whole-core measurements, conducted with the MST, included GRA bulk density (2.5-cm intervals), magnetic susceptibility (2.5-cm intervals), NCR (5-cm intervals), and NGR (15-cm intervals). Compressional (*P*)-wave velocity was measured in the transverse direction on split cores at ~50-cm intervals and along both transverse and longitudinal directions on cube samples taken at a frequency of two per core in Hole 1261B between ~380 and 560 mbsf.

Moisture and density (MAD) measurements were conducted on discrete samples at a frequency of one per section from both holes at Site 1261. Sampling for MAD was reduced across critical intervals, important transitions, and throughout lithostratigraphic Unit IV (Cretaceous black shale sequence). A full description of the various measurement techniques can be found in "Physical Properties," p. 33, in the "Explanatory Notes" chapter.

Density and Porosity

MAD properties determined at Site 1261 include bulk density, dry bulk density, porosity, grain density, water content, and void ratio (Table T18). Bulk density was determined on whole-core sections using the MST (GRA density) and on discrete samples. GRA-derived densities tend to underestimate the true bulk density because RCB cores do not completely fill the inner diameter of the liner. The average difference between the GRA and MAD density for Hole 1261A was 0.199 g/cm³. Differences in the MAD- and GRA-derived density vary between lithostratigraphic units and have been calculated for samples taken from both holes at Site 1261 (Table T19). If the GRA data sets are to be used for quantitative purposes it is recommended that they should first be corrected to the MAD data.

The upper 300 m of Site 1261 appears normally consolidated, with bulk density increasing linearly with depth (Fig. F18). An abrupt drop in the grain density and porosity occurs at 300 mcd but is not reflected in the bulk density. Porosity and, to a greater degree, grain density are highly variable throughout a debris flow deposit between 310 and 370 mbsf (Subunit IC), reflecting the variable composition of clasts and matrix. In contrast, bulk density maintains a linear increase with depth through this interval, indicating postdepositional normal consolidation.

The calcareous chalk and limestone of Unit II has greater variability in all MAD properties (Fig. F18). This variability arises from cyclic alternations between light greenish gray and greenish gray calcareous chalks with the darker layers containing higher proportions of clay (see

T18. MAD of discrete samples, p. 97.

T19. GRA and MAD bulk density, p. 101.

F18. Bulk and grain density and porosity, p. 63.

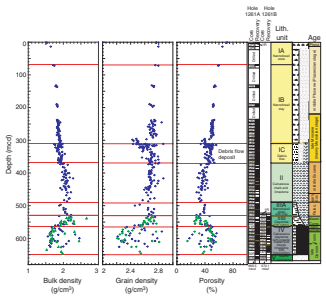

"Lithostratigraphy," p. 3). Porosity increases across the Unit II/Subunit IIIA boundary, coincident with the P/E boundary, and is matched by a decrease in both bulk density and grain density.

In Subunit IIIA, density increases with depth (porosity covarying), indicating normal consolidation. This is supported by the grain density, which does not change downhole. Throughout Subunit IIIB, porosity increases and bulk density and grain density decrease. Light–dark color bands, produced by changing abundances of carbonate and clay, are responsible for the variability in bulk density, grain density, and porosity in this subunit (Fig. F18).

Unit IV is characterized by low and variable bulk density, highly variable grain density, and a slight tendency toward higher porosity in the middle of the unit. Peaks in the density and grain density are associated with variably cemented limestone and sandstone intervals interbedded with the organic-rich, low-density laminated claystone.

No MAD samples were taken in Unit V.

Acoustic Velocity

P-wave velocity was measured on split cores using the modified Hamilton Frame apparatus. In addition, measurements of transverse (x- and y-direction) and longitudinal (z-direction) velocity were conducted on cube samples from Hole 1261B (Table T20).

The general depth trend of acoustic velocity correlates directly with bulk density and inversely with porosity (Figs. F18, F19). In Unit II, the variability in the MAD data is even more pronounced in the velocity data, reflecting the cyclical alterations of green clay-rich bands (low velocity) and light variably cemented calcite-rich (higher velocity) bands ("Lithostratigraphy," p. 3). A reduction in the variability of the velocity data and a shift toward decreasing velocity with depth characterizes the bottom 30 m of Unit II. This shift is controlled by increasing clay content downhole through the transition into Unit III.

Velocity increases to the base of Subunit IIIA, driven by the increase in density with depth, which reflects normal consolidation in this part of the section. Velocity then decreases through Subunit IIIB due to increasing clay content.

In Unit IV (black shale sequence), the average velocity of the laminated organic-rich claystones is 1700 m/s, whereas sandstone/limestone velocity varies between 2000 and 4000 m/s (Fig. F19). Unit V has high velocity (~4400 m/s) (Fig. F19), consistent with a well-indurated quartz sandstone lithology.

Whole-Core Multisensor Track

MST data through the clay-rich sequences of Subunits IA and IB have a high and constant NGR signal of 50 counts per second (cps) and an average magnetic susceptibility of 30 (magnetic susceptibility is reported here as dimensionless instrument units. See "Physical Properties," p. 33, in the "Explanatory Notes" chapter for conversion of these data to SI units), matching the uniformity in sediment composition. NGR and magnetic susceptibility become more variable in Subunit IC, and a distinct and abrupt drop in both between 320 and 340 mcd corresponds to an expanded light green sequence in the debris flow of Subunit IIC through Cores 207-1261A-16R and 17R (Fig. F20).

A drop to background noise levels of both the magnetic susceptibility and NGR values marks the transition into the calcareous chalk and

T20. Velocity measurements, p. 102.

F19. Acoustic velocity and velocity anisotropy, p. 64.

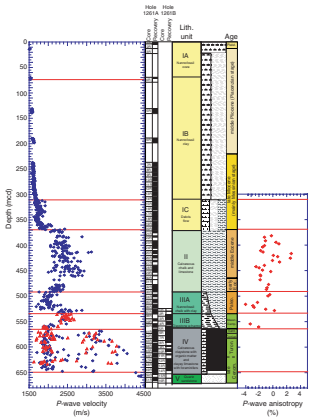

F20. MST data vs. lithostratigraphic units, p. 65.

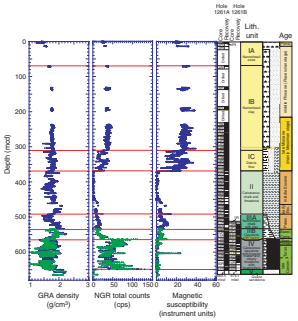

limestone of Unit II. At ~450 mcd, there is a rise in both the NGR and magnetic susceptibility signals that continues across the boundary with Subunit IIIA. GRA density is highly variable through Unit II, reflecting the changing sediment composition (alternating high–low clay content). This interpretation is supported by the comparison between GRA density and MAD bulk density (Table T19).

Crossing into Subunit IIIA, a spike in both NGR and magnetic susceptibility marks the P/E boundary. GRA density drops abruptly across this interval and then increases slowly downhole through Subunit IIIA. A distinct drop in magnetic susceptibility and NGR emissions occurs at ~530 mcd. From here, NGR emissions fluctuate across the hiatus separating the Paleocene and Cretaceous (Subunit IIIA/IIB boundary). NGR counts increase downhole through Subunit IIB with a concomitant decrease in GRA density (Fig. F20), reflecting increasing clay content.

Unit IV is characterized by highly variable GRA and NGR signals that correspond to the alternation of laminated organic-rich intervals and cemented limestone and sandstone (Fig. F20). NGR emissions are highest between ~560 and 585 mcd. Another distinct aspect of the NGR signal is its slow rise near the bottom of Unit IV, where values gradually climb back to levels seen at the top of the sequence. At the contact with Unit V, NGR emissions drop to instrument noise levels. Magnetic susceptibility remains relatively constant through Unit IV, with a narrow spike at ~ 605 mcd, representing a glauconite-rich calcareous claystone (see "Lithostratigraphy," p. 3). This spike is preceded by a ~10-m interval devoid of any measurable magnetic susceptibility signal (Fig. F20). The GRA profile through the shale sequence shows two minima between ~590 and 600 mcd and between 630 and 640 mcd; these broadly correlate to peaks in MAD-derived porosity (Fig. F18).

The boundary between Units IV and V is sharp and best defined by the increase in GRA density and drop in NGR emissions. There is no discernable change in magnetic susceptibility across this interval.

DOWNHOLE LOGGING

Following completion of RCB coring operations in Hole 1261B, the hole was conditioned with a wiper trip and pumped with sepiolite mud. The drill pipe was set at 110 mbsf (logging depth) for all passes. The following three tool strings were run:

1. The triple combo tool string with the Lamont-Doherty Earth Observatory (LDEO) Temperature/Acceleration/Pressure (TAP) tool and Multi-Sensor Spectral Gamma Ray Tool (MST).
2. The FMS-sonic tool string.
3. The WST (see "Downhole Logging," p. 39, in the "Explanatory Notes" chapter for the tool specifications).

The wireline heave compensator (WHC) was used on all passes, with heave varying between 1.3 and 3.0 m throughout the operation. The first tool string run was the triple combo, which encountered a bridge at 210 mbsf. After working the tool for ~30 min, the triple combo passed through and reached the bottom of the hole without further trouble (665 mbsf). There was ~21 m of fill in the bottom of the hole. At the beginning of the first pass, the WHC began to stroke out because of a malfunction of one or both of the limiter switches. This problem was repaired, and during the first pass the WHC stroked out on one occasion

(when heave reached ~3 m). Power was lost to the tool string at 325 mbsf and was reestablished at 316 mbsf. Pass 1 of the triple combo tool string was terminated at 314 mbsf in order to be used as the repeat section. The tool string was lowered, and pass 2 began. High heave again caused the WHC to stroke out on two occasions, between 488 and 470 and 434 and 410 mbsf. The WHC operated for the remainder of the pass (switched off at 141 mbsf), which continued up past the seafloor. A rise in the head tension on the upward pass indicated a tight spot at 210 mbsf but did not cause any difficulties. Following this run, control of the wireline passed to the downhole measurements laboratory and the MGT was powered up and stabilized. One full pass one short repeat pass from 172.5 mbsf into the pipe was made with the MGT. The second tool string, the FMS-sonic, was successfully run to the bottom of the hole, although a reduction in head tension was observed as the tool string passed through 210 mbsf. Two full passes were made with the tool string, logging at maximum FMS recommended speed (548.6 m/hr); the second was made to the seafloor. The WST also encountered the restriction at 210 mbsf but, due to its lower weight, was unable to pass through. Five checkshot stations were acquired between 210 mbsf and the base of the pipe (110 mbsf). In summary, three tool strings were run during the logging operation with seven separate logging passes. Two passes were conducted from total depth to above seafloor, one from total depth into the pipe, and three were reduced-length passes (Fig. **F21**). The wireline depth to seafloor was set at 1899 meters below rig floor (mbrf), determined from the step increase in gamma ray counts found at the sediment/seafloor interface recorded by the Scintillation Gamma Ray Tool (SGT) on the second pass of the FMS. The official ODP depth to seafloor was 1911.1 mbrf. Thus, there is a 12.1-m offset between the core and logging depths. In all of the chapter diagrams the core recovery and lithostratigraphic units have not been depth shifted, giving an apparent 12.1-m depth mismatch, but all core physical property data used in figures herein have been depth shifted.

F21. Summary of logging runs, p. 66.

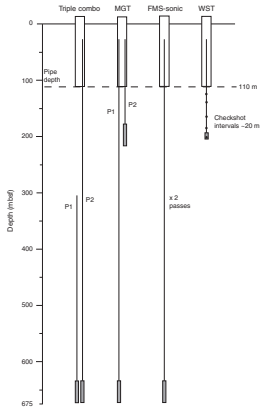

Data Quality

Borehole diameter can affect the response of some tools (e.g., the Hostile Environment Litho-Density Tool [HLDT] and Accelerator Porosity Sonde) and so the size and shape of the borehole are important for interpreting the quality of logging data. The caliper logs from the triple combo (1 per pass) and the FMS-sonic (2 per pass) tool strings provide information on the borehole size (Fig. **F22**). From the pipe (110 mbsf) down to 150 mbsf, the hole diameter varies between bit size and 12 in. From 150 to 374 mbsf, the hole is in very poor condition, with rapid fluctuations beyond 18 in (45.76 cm), which is larger than the maximum extension of both the FMS-sonic (15.5 in; 39.4 cm) and triple combo (18 in; 45.76 cm) calipers. From 374 mbsf to total depth, the borehole is in excellent condition being at or just beyond bit size, except for a few short sections of washouts/breakouts. Because of the borehole conditions, all logs are good below 374 mbsf but above this depth FMS-sonic, density, and porosity have all been adversely affected. The repeat section for the triple combo tool string has only minor (<1 m) depth mismatches between passes, despite the problems with the WHC. Gamma ray data from the HNGS, MGT, and SGT are also well matched in depth and magnitude, making depth matching of the MGT and triple combo tool string logging runs to pass 2 of the FMS-sonic tool string straightforward.

F22. Borehole caliper logs, p. 67.

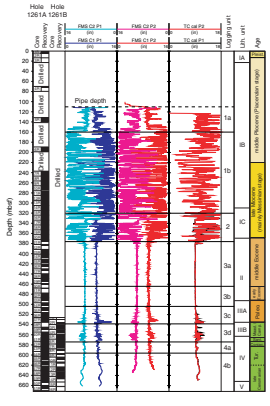

Core physical property data provide a rapid method for visualization of the core-log correlation (Fig. F23). Because of drilling ahead with selective coring, there is a paucity of core data from Hole 1261B, so all of the core data presented are from Hole 1261A. Borehole diameter and wall rugosity effects are adequately displayed by the offset between the core and logging density and porosity values from 150 to 374 mbsf. MAD properties and logging data correlate very well for the remainder of the hole. Core gamma measurements slightly underestimate formation values, but the pattern match is good. Core velocities, measured directly on the core with the modified Hamilton Frame, are close to the logging values, except for the interval between 374 and 538 mbsf, where they are considerably less (100 m/s). The depth match between logging mbsf and core data is excellent when the core depths are corrected (12.1-m downhole shift).

Logging Stratigraphy

Four logging units have been defined for Hole 1261B.

Unit 1 (Base of Pipe [110 mbsf] to 320 mbsf)

Unit 1 is characterized by high gamma ray counts and low resistivity and velocity values (Fig. F24). Borehole conditions throughout most of this unit are poor, but gamma ray, resistivity, and velocity tools are not greatly affected by these problems. The logging unit is further subdivided into two subunits.

Subunit 1a (110–160 mbsf)

The borehole diameter for most of this subunit is between bit size and 12 in (30.5 cm), and so all logs are expected to be of good quality. Gamma ray values are high at the top and decrease toward the bottom of the subunit (Figs. F24, F25). A submeter-scale cyclicity is apparent in the gamma ray logs. Resistivity, porosity, density, and velocity fluctuate moderately around a constant average (Fig. F24).

Subunit 1b (160–320 mbsf)

The borehole diameter throughout this subunit fluctuates greatly. The hole is enlarged to well beyond bit size in some places and is significantly under gauge in others. The under-gauge areas are interpreted to result from deformation (i.e., expansion) of the clay-rich layers (see "Lithostratigraphy," p. 3). Because of poor borehole conditions, density and porosity logs are not used in any descriptions or interpretations of this subunit. Gamma ray levels are high through the unit, reflecting high clay content. This trend is seen in the gamma ray spectrum as the computed gamma ray plots directly over the total gamma ray counts (Fig. F25). High-resolution data obtained with the MGT shows cyclicity down to the submeter scale (Fig. F26). Figure F26 also show that the under-gauge parts of the borehole equate to the clay-rich horizons. Correlation between core and logging data is excellent, given that the core data have only been depth shifted (–12.1 m) and not depth matched. This good core-log correlation also supports the interpretation that the gamma ray logs are valid in terms of the relative changes, if not absolute magnitudes. Velocities increase slowly downhole, suggesting a normal consolidation trend that is supported by the core bulk density data (Fig. F23) (see "Physical Properties," p. 29). Resistivity is low through-

F23. Geophysical logs and core physical properties, p. 68.

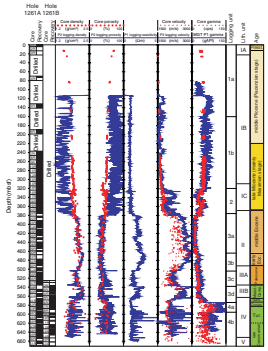

F24. Geophysical logs and caliper data, p. 69.

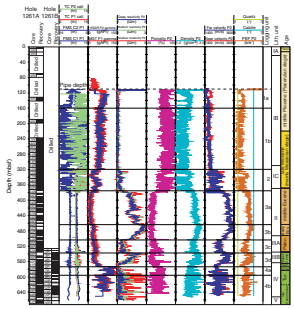

F25. MGT gamma ray logs, p. 70.

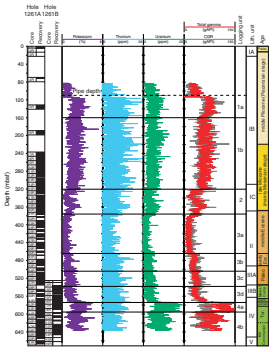

F26. MGT and core gamma ray data, p. 71.

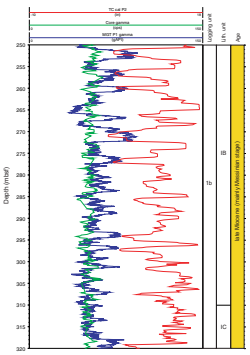

out the subunit. The base of this subunit correlates with the base of lithostratigraphic Subunit IB (see "Lithostratigraphy," p. 3).

Unit 2 (320–380 mbsf)

The top of Unit 2 is seen as a peak in the gamma ray log (Figs. F24, F25). Below the boundary, resistivity and velocity increase in magnitude (Figs. F24, F25). The borehole is still in poor condition, so no density or porosity data are used to define this unit. Between 330 and 340 mbsf, the borehole becomes uniform and density and porosity data are good (Fig. F27). The photoelectric effect (PEF) log indicates a shift toward more carbonate-rich sediment (Fig. F27) and cycles are observed in the FMS-sonic images. This interval is interpreted as a 10-m-thick raft of nannofossil chalk in a large debris flow. The equivalent section was seen in the core in Hole 1261A (Cores 207-1261A-16R and 17R) as clasts of nannofossil chalk up to 0.2 m (see "Lithostratigraphy," p. 3, and "Paleomagnetism," p. 19). Gamma ray values first decrease and then increase before dropping off again at the base of the unit. Velocity values increase steadily downhole, but an increase in resistivity occurs only toward the base of the unit. The base of logging Unit 2 correlates with lithostratigraphic Subunit IC (see "Lithostratigraphy," p. 3) and the middle Eocene–late Miocene unconformity. It is clearly observed in all of the logs, particularly in the borehole diameter data (Figs. F21, F24).

F27. Triple combo logs and FMS imagery, p. 72.

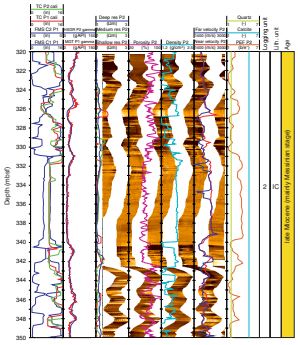

Unit 3 (380–574 mbsf)

Logging Unit 3 is clearly visible in all logging data (Figs. F22, F24). Borehole conditions improved dramatically and are similar to those experienced in other holes logged throughout the leg (see "Downhole Logging," p. 29, in the "Site 1257" chapter; "Downhole Logging," p. 33, in the "Site 1258" chapter; and "Downhole Logging," p. 33, in the "Site 1260" chapter). The top boundary is defined by a decrease in gamma ray and porosity, with a concomitant rise in resistivity, density, and velocity. The decrease in gamma ray (reduction in clay) is matched by a rise in the PEF log toward calcite, indicating an increase in the carbonate content (see "Organic Geochemistry," p. 24) compared to logging Units 1 and 2. The unit is further subdivided into four subunits.

Subunit 3a (380–464 mbsf)

In Subunit 3a, gamma ray counts are the lowest of the formation and fluctuate around a constant average. Density (porosity covarying) and velocity increase with depth and may follow a normal consolidation line, although the trend may also be due, at least in part, to increasing carbonate content as observed in the PEF log (Fig. F24). Resistivity increases downhole, punctuated by a step to lower values between 426 and 441 mbsf. A similar pattern is seen in the velocity log. Density and porosity data show only a single step change to lower and higher values, respectively, from which they gradually recover. Gamma ray and porosity logs display cyclicity to the submeter scale. The base of the subunit is marked by an increase in gamma ray, resistivity, and density.

Subunit 3b (464–504 mbsf)

Resistivity and velocity remain high at the top of the Subunit 3b for ~20 m and then decrease downhole to the bottom (Fig. F24). Density decreases steadily for the length of the subunit and appears to be related to a decrease in carbonate content, indicated by the PEF log (Fig.

F24). The gamma ray log takes a step increase across the upper boundary and maintains a relatively constant average. The porosity log shows little change across the boundary and also fluctuates around a constant average. Both the gamma ray and porosity logs show cyclicity down to the submeter scale. The base of the subunit is defined as a peak in gamma ray and porosity curves and a trough in resistivity, density, and velocity logs and correlates with the P/E boundary (see "Biostratigraphy," p. 10) and the lithostratigraphic Unit II/III boundary (see "Lithostratigraphy," p. 3) (Fig. F24).

Subunit 3c (504–538 mbsf)

Resistivity and velocity magnitudes decrease sharply across the upper boundary of Subunit 3c and exhibit large-amplitude variations (Fig. F24). Density undergoes a smaller decrease but displays similar enhanced amplitude fluctuations (Fig. F24). The gamma ray and porosity log values conversely increase downhole, both displaying cyclicity down to the submeter scale. The base of the subunit is marked by a step increase in several of the logs, best seen in resistivity and velocity and only slightly less pronounced in density. Porosity and gamma ray values concomitantly show a step decrease.

Subunit 3d (538–574 mbsf)

Resistivity, density, and velocity values all decrease downhole from the upper boundary and have higher-amplitude fluctuations relative to the other Unit 3 subunits (Fig. F24). Gamma ray and porosity logs increase downhole, with the porosity log also displaying higher-amplitude fluctuations. The PEF log indicates increased carbonate content, and a number of peaks reach the calcite photoelectric absorption cross-section index (*Pe*), suggesting carbonate-rich layers. This apparent increase in carbonate is not supported by core lithostratigraphic descriptions, which indicates this subunit has an increased clay content. It is, however, supported by geochemical analysis that shows an increase in carbonate content to values just below 90 wt% (see "Organic Geochemistry," p. 24). The PEF-carbonate interpretation is supported by the gamma ray log, which indicates low clay content (Fig. F25). It is difficult at this stage, without detailed core-log depth matching, to determine if the top of the subunit correlates with the K/T unconformity (see "Biostratigraphy," p. 10) or if the K/T unconformity is the trough in density, velocity, and resistivity (peak in gamma and porosity) seen 6 m below the upper subunit boundary. The base of the subunit is marked by a rapid increase in the gamma ray log and a smaller increase in the porosity log and correlates with the bottom of lithostratigraphic Subunit IIIB (now with a 10-m offset) (see "Lithostratigraphy," p. 3).

Unit 4 (574 mbsf–Total Depth [665 mbsf])

Logging Unit 4 demonstrates a shift in the gamma ray and porosity logs to higher levels and the density and velocity logs to lower levels. All logs exhibit increased amplitude fluctuations, especially seen in resistivity (Figs. F24, F28). The unit is further subdivided into two subunits.

Subunit 4a (574–596 mbsf)

The sharp increase in gamma ray values at the upper boundary is maintained to the base of Subunit 4a, punctuated by a number of large amplitude fluctuations. The gamma ray spectrum (Fig. F25) shows that this increase is due mainly to an increase in uranium and, to a lesser ex-

F28. Stratigraphy of the black shales, p. 73.

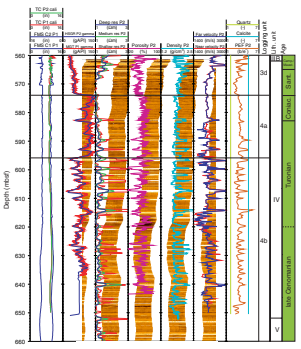

tent, an increase in potassium content. The increase in uranium (bound to organic matter) is supported by core lithology descriptions (see "Lithostratigraphy," p. 3). Layers with high resistivity, density, velocity, and low gamma ray and porosity magnitudes are interpreted to be carbonate cemented, corroborated with peaks in the PEF log (Fig. F28). The upper boundary of the subunit correlates with the top of lithostratigraphic Unit IV (see "Lithostratigraphy," p. 3). The base of the subunit is marked by a step decrease in the gamma ray log.

Subunit 4b (596 mbsf–Total Depth [665 mbsf])

The gamma ray spectrum indicates that the decrease in gamma ray value is due mostly to a reduction in uranium and, to a lesser degree, in potassium (Fig. F25). Uranium contribution increases again toward the base of the subunit. Resistivity, porosity, density, and velocity logs fluctuate at higher amplitudes than in logging Subunit 4a (Fig. F28). Layers with high resistivity, density, and velocity values are distinct in the FMS imagery and are interpreted as carbonate-cemented layers. At 614 mbsf, the PEF log extends beyond the calcite line and correlates with a coarse-grained glauconite-rich layer seen in Sections 207-1261A-45R-2 and 207-1261B-9R-4 (Fig. F28) (see "Lithostratigraphy," p. 3). The base of the subunit extends to the bottom of the logged interval. Lithostratigraphic Unit V is not represented in the logging stratigraphy because 21 m of fill limited the penetration of logging tools to 665 mbsf, which is at the lithostratigraphic Unit IV/V boundary (when depth shifted 12.1 m to the logging seafloor depth).

Discussion

High heave conditions initially caused problems, but data from those runs have been depth matched to pass 2 of the FMS-sonic tool string when the WHC operated throughout, thus removing any problems related to increased heave. Poor hole conditions in the upper part of the borehole (above 376 mbsf) limited the use of some logging data in this region. The main focus was the black shale interval, which was adequately recorded and is readily interpreted with the logging data. For the most part, the logging units described above correlate well with the designated lithostratigraphic units (see "Lithostratigraphy," p. 3) once the core depths have been shifted down 12.1 m to account for the logging and drillers seafloor depth mismatch.

Total Organic Carbon

The continuous data derived from the logs through the black shale interval (logging Unit 4) provide the opportunity for estimation of the TOC content in this unit. The result is only approximate because the shale porosity is assumed to equate to that of the sediments above, and values for some densities (e.g., organic matter) that are not well constrained are also assumed. Following Rider (1996), the following three equations are used to calculate the TOC:

$$\phi_{fl} = (\rho_{bk} - \rho_{ma})/(\rho_{fl} - \rho_{ma}),$$

$$\phi_{om} = (\rho_{bs} - \rho_{bk})/(\rho_{om} - \rho_{ma}), \text{ and}$$

$$\text{TOC (wt\%)} = ([0.85 \times \rho_{om} \times \phi_{om}]/[(\rho_{om} \times \phi_{om}) + \rho_{ma}(1 - \phi_{om} - \phi_{fl})]) \times 100\%,$$

where

ρ_{bk} = density of the background sediment from the density log (2.043 g/cm³).
ρ_{bs} = density of the black shale interval, taken from the density log.
ρ_{om} = density of the organic matter (assumed) (1.15 g/cm³).
ρ_{ma} = density of the matrix (grain density) averaged from five MAD measurements (2.483 g/cm³).
ρ_{fl} = density of seawater (1.05 g/cm³).
ϕ_{fl} = water-filled porosity.
ϕ_{om} = volume fraction of organic matter.

Calculated TOC results are plotted along with values measured on core samples from Holes 1261A and 1261B (see **"Organic Geochemistry,"** p. 24) and are shown in Figure **F29.** The core depths have been depth shifted but are not depth matched to the logs.

Checkshot Survey and Synthetic Seismograms

A checkshot survey was conducted during logging operations in Hole 1261B, but a bridge encountered at 210 mbsf limited the depth of penetration of the WST tool string (see the first paragraph of **"Downhole Logging,"** p. 31). Five stations were collected, using a series of stacked shots at 20-m intervals up the borehole (Fig. **F21**). The checkshot survey provides a direct measurement of acoustic traveltime (Table **T21**) and, thus, formation velocity. Conversion of these traveltimes to interval velocities allows the checkshot data to calibrate the velocity log, which has proved particularly useful at Site 1261 given the poor borehole conditions in the upper part of the hole and the lack of physical property measurements (see **"Physical Properties,"** p. 29). To compute a synthetic seismogram, formation density, and velocity profiles are needed. Wireline logging density and velocity logs were used from the bottom of the hole up to 248 mbsf. Interval velocities calculated from the checkshot survey were used for the upper part. Downhole impedance was calculated from velocity × density, and the impedance contrast between successive layers gave the reflection coefficient series (Fig. **F30**). An idealized Ormsby wavelet was convolved with the reflection coefficient series to generate the synthetic seismogram (Fig. **F31**).

The synthetic seismogram matches allowed lithostratigraphic units and seismic stratigraphy to be correlated. Reflector B′ ties to the top of the black shale sequence (574 mbsf), and Reflector B matches the density and velocity step (538 mbsf) at the Subunit 3c/3d boundary, equivalent to the lithostratigraphic Subunit IIIA/IIIB boundary (see **"Lithostratigraphy,"** p. 3). Reflector A correlates with the logging Unit 2/Subunit 3a boundary, the middle Eocene–late Miocene unconformity (see **"Biostratigraphy,"** p. 10), and is equivalent to the lithostratigraphic Subunit IC/Unit II boundary (see **"Lithostratigraphy,"** p. 3).

F29. Core-measured vs. log-calculated TOC, p. 74.

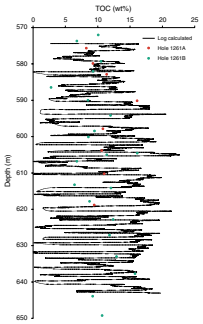

T21. Checkshot data, p. 103.

F30. Density, velocity, impedance, and reflection profiles, p. 75.

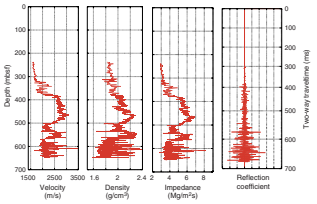

F31. Reflectors, synthetic seismogram, and impedance profile, p. 76.

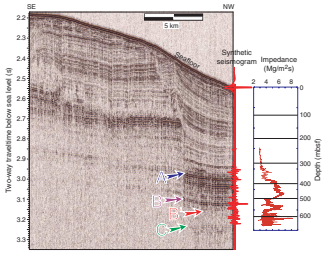

REFERENCES

Boetius, A., Ravenschlag, K., Schubert, C.J., Rickert, D., Widdel, F., Gieseke, A., Amann, R., Jørgensen, B.B., Witte, U., and Pfannkuche, O., 2000. Microscopic identification of a microbial consortium apparently mediating anaerobic methane oxidation above marine gas hydrate. *Nature,* 407:623–626.

Borowski, W.S., Paull, C.K., and Ussler, W., III, 1999. Global and local variations of interstitial sulfate gradients in deep-water, continental margin sediments: sensitivity to underlying methane and gas hydrates. *Mar. Geol.,* 159:131–154.

Brumsack, H.-J., 1986. The inorganic geochemistry of Cretaceous black shales (DSDP Leg 41) in comparison to modern upwelling sediments from the Gulf of California. *In* Summerhayes, C.P., and Shackleton, N.J. (Eds.), *North Atlantic Palaeoceanography.* Geol. Soc. Spec. Publ., 21:447–462.

Brumsack, H.-J., and Zuleger, E., 1992. Boron and boron isotopes in pore waters from ODP Leg 127, Sea of Japan. *Earth Planet. Sci. Lett.,* 113:427–433.

Chaisson, W.P., and Pearson, P.N., 1997. Planktonic foraminifer biostratigraphy at Site 925: middle Miocene–Pleistocene. *In* Shackleton, N.J., Curry, W.B., Richter, C., and Bralower, T.J. (Eds.), *Proc. ODP, Sci. Results,* 154: College Station, TX (Ocean Drilling Program), 3–31.

Claypool, G.E., and Kvenvolden, K.A., 1983. Methane and other hydrocarbon gases in marine sediment. *Annu. Rev. Earth Planet. Sci.,* 11:299–327.

Church, T.M., and Wolgemuth, K., 1972. Marine barite saturation. *Earth Planet. Sci. Lett.,* 15:35–44.

Dixit, S., van Cappellen, P., and van Bennekom, A.J., 2001. Processes controlling solubility of biogenic silica and pore water buildup of silicic acid in marine sediments. *Mar. Chem.,* 73:333–352.

Espitalié, J., Laporte, J.L., Madec, M., Marquis, F., Leplat, P., Paulet, J., and Boutefeu, A., 1977. Méthode rapide de caractérisation des roches mères, de leur potentiel pétrolier et de leur degré d'évolution. *Rev. Inst. Fr. Pet.,* 32:23–42.

Malmgren, B.A., Berggren, W.A., and Lohmann, G.P., 1983. Evidence for punctuated gradualism in the late Neogene *Globorotalia tumida* lineage of planktonic foraminifera. *Paleobiology,* 9:377–389.

Meyers, P.A., 1997. Organic geochemical proxies of paleoceanographic, paleolimnologic, and paleoclimatic processes. *Org. Geochem.,* 27:213–250.

Müller, P.J., 1977. C/N ratios in Pacific deep sea sediments: effect of inorganic ammonium and organic nitrogen compounds sorbed by clays. *Geochim. Cosmochim. Acta,* 41:765–776.

Okada, H., and Bukry, D., 1980. Supplementary modification and introduction of code numbers to the low-latitude coccolith biostratigraphic zonation (Bukry, 1973; 1975). *Mar. Micropaleontol.,* 5:321–325.

Peters, K.E., 1986. Guidelines for evaluating petroleum source rock using programmed pyrolysis. *AAPG Bull.,* 70:318–329.

Rider, M.H., 1996. *The Geological Interpretation of Well Logs* (2nd ed.): Caithness (Whittles Publishing).

Torres, M.E., Brumsack, H.-J., Bohrmann, G., and Emeis, K.C., 1996. Barite fronts in continental margin sediments: a new look at barium remobilization in the zone of sulfate reduction and formation of heavy barites in diagenetic fronts. *Chem. Geol.,* 127:125–139.

Twichell, S.C., Meyers, P.A., and Diester-Haass, L., 2002. Significance of high C/N ratios in organic-carbon-rich Neogene sediments under the Benguela Current upwelling system. *Org. Geochem.,* 33:715–722.

Waterman, L.S., Sayles, F.L., and Manheim, F.T., 1972. Interstitial water studies on small core samples, Leg 14. *In* Hays, D.E., Pimm, A.C., et al., *Init. Repts. DSDP,* 14: Washington (U.S. Govt. Printing Office), 753–762.

Figure F1. Seismic line GeoB213 at Site 1261. See Figure F1, p. 5, in Shipboard Scientific Party, this volume ("Site Survey and Underway Geophysics") for a location map for this line.

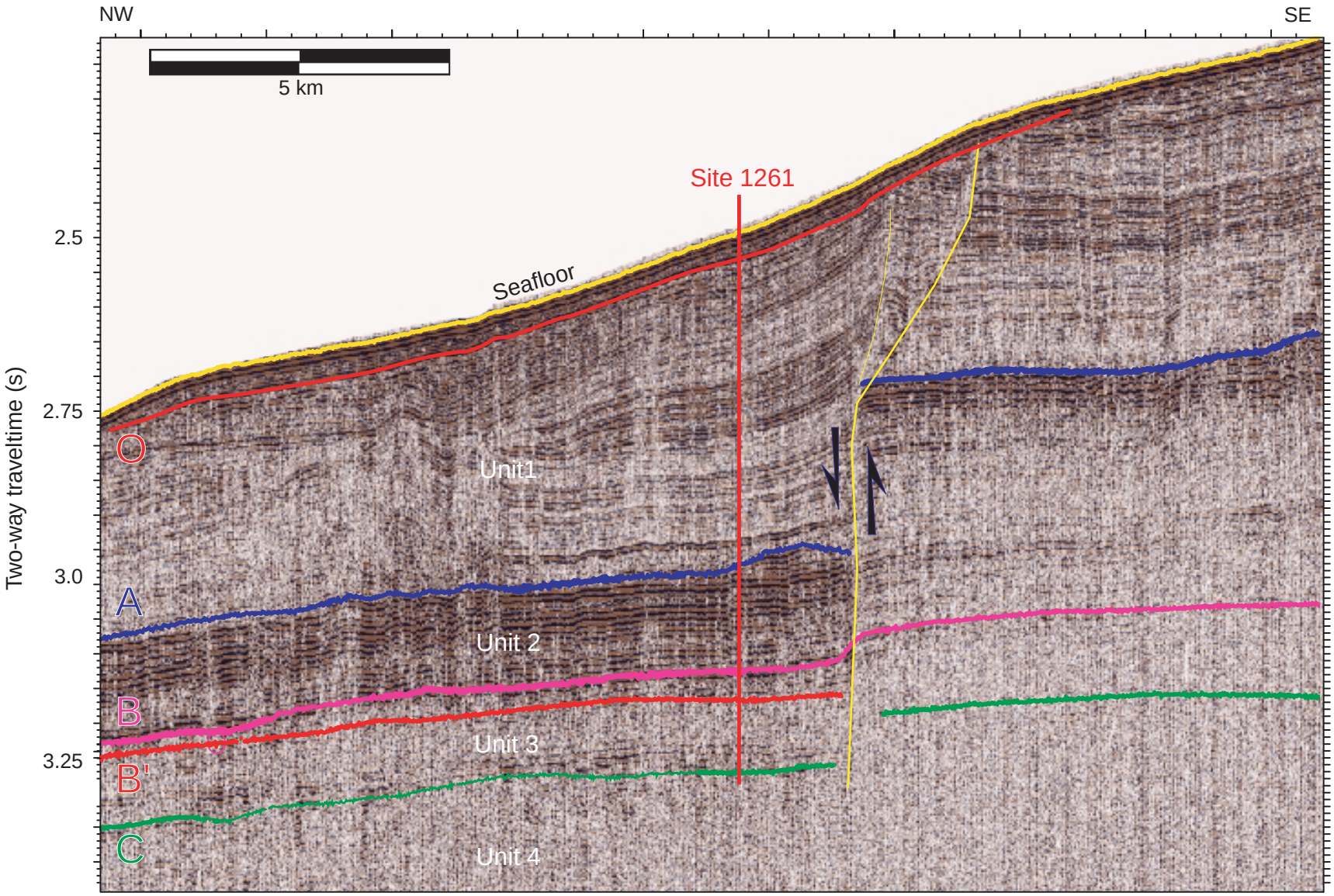

Figure F2. Industry multichannel seismic reflection line C2206a passing 8 km east of Site 1261. See Figure F1, p. 5, in Shipboard Scientific Party, this volume ("Site Survey and Underway Geophysics") for a location map for this line. The site location is projected onto the line at the point of closest passing.

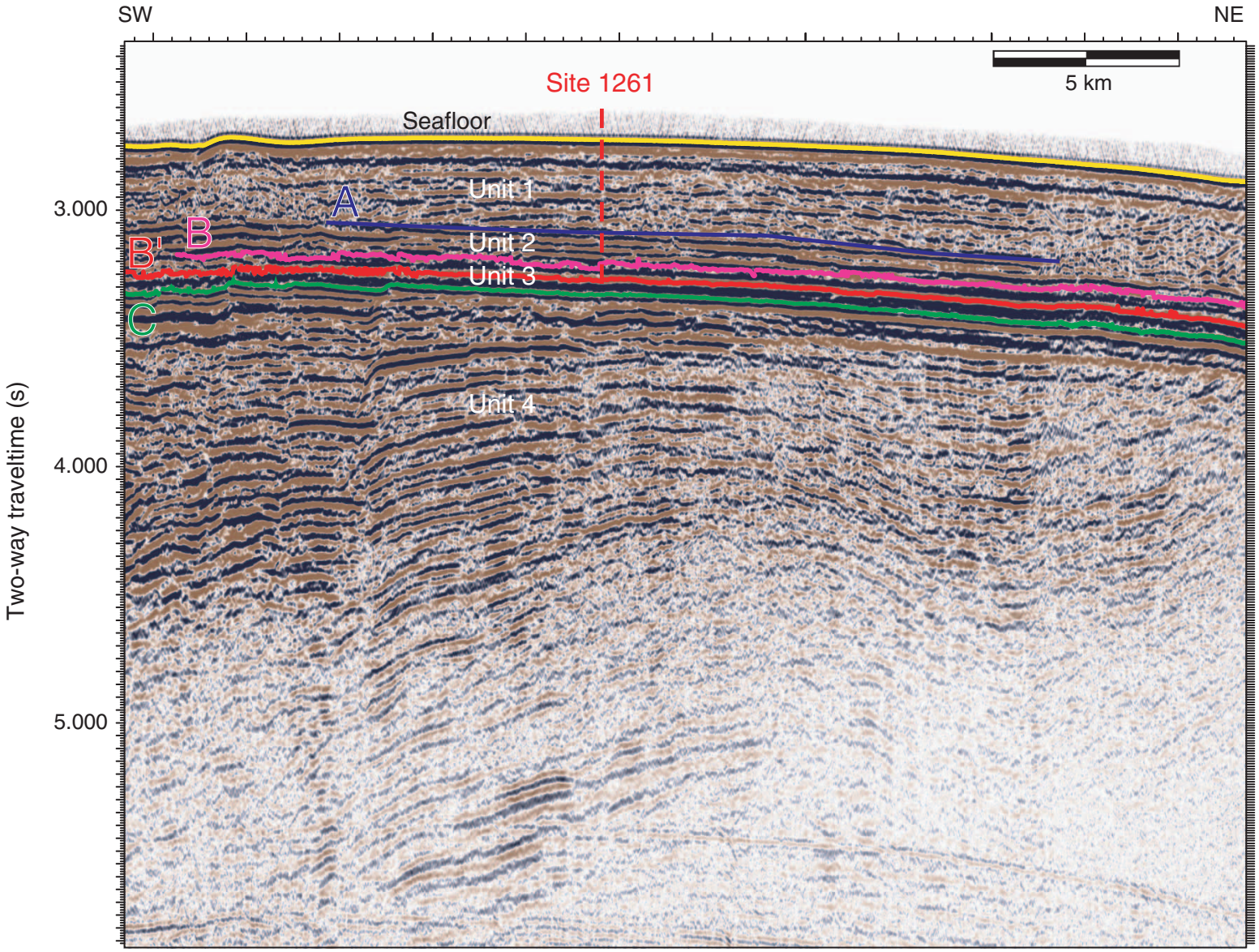

Figure F3. Comparison of core recovery, lithostratigraphic units, carbonate, and total organic carbon (TOC) content at Site 1261.

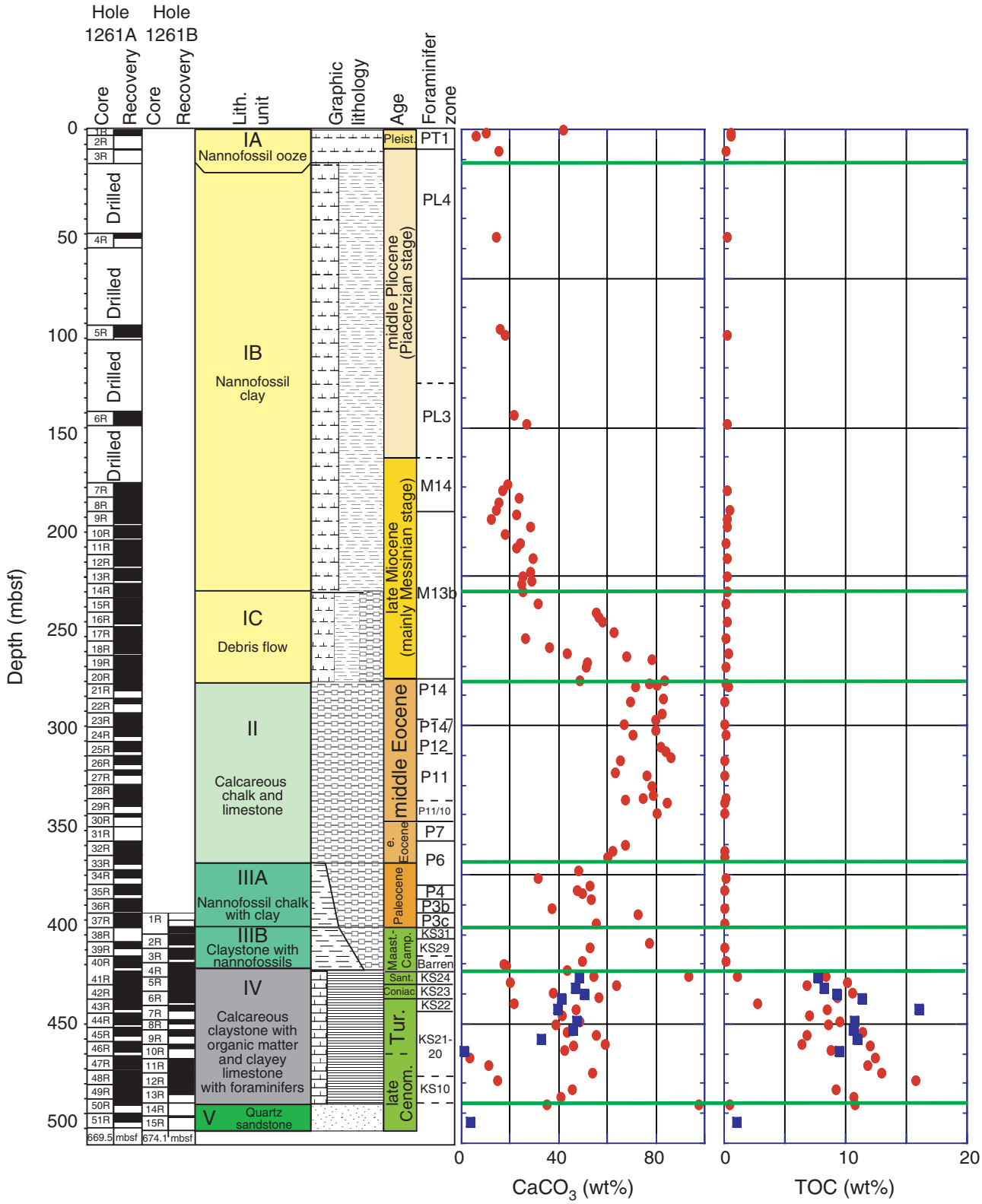

Figure F4. Summary of lithostratigraphic units.

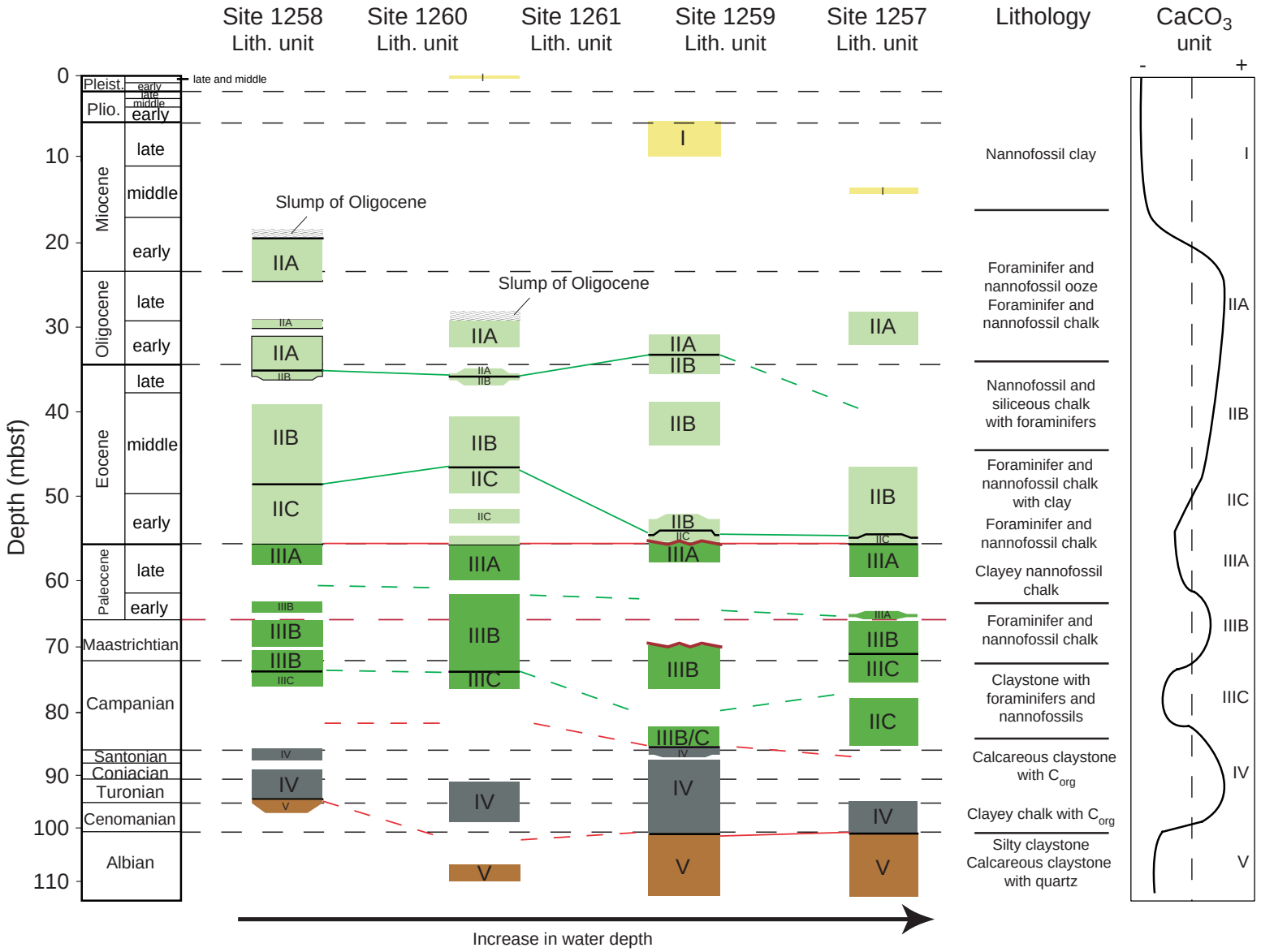

Figure F5. Close-up photographs of representative lithologies from Unit I at Site 1261. **A.** Nannofossil clay of Subunit IB (interval 207-1261A-7R-1, 55–69 cm). The white specks are foraminifers. **B.** Recumbent fold in the Miocene debris flow of Subunit IC (Interval 207-1261A-19R-2, 93–113 cm). (Continued on next page.)

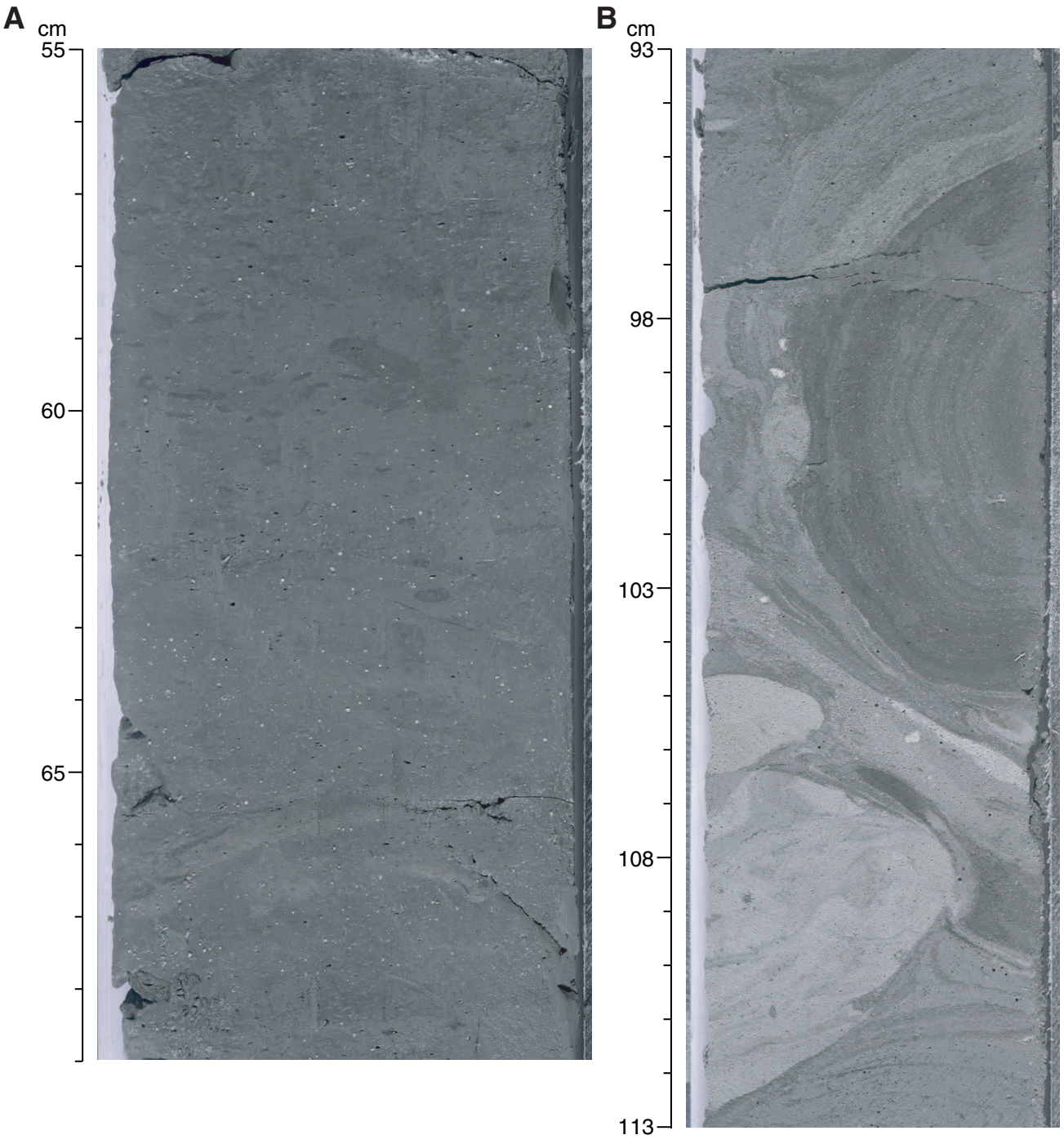

Figure F5 (continued). C. Distinct multicolored matrix-supported conglomerate (debris flow) characteristic of Subunit IC (interval 207-1261A-14R-5, 120–140 cm).

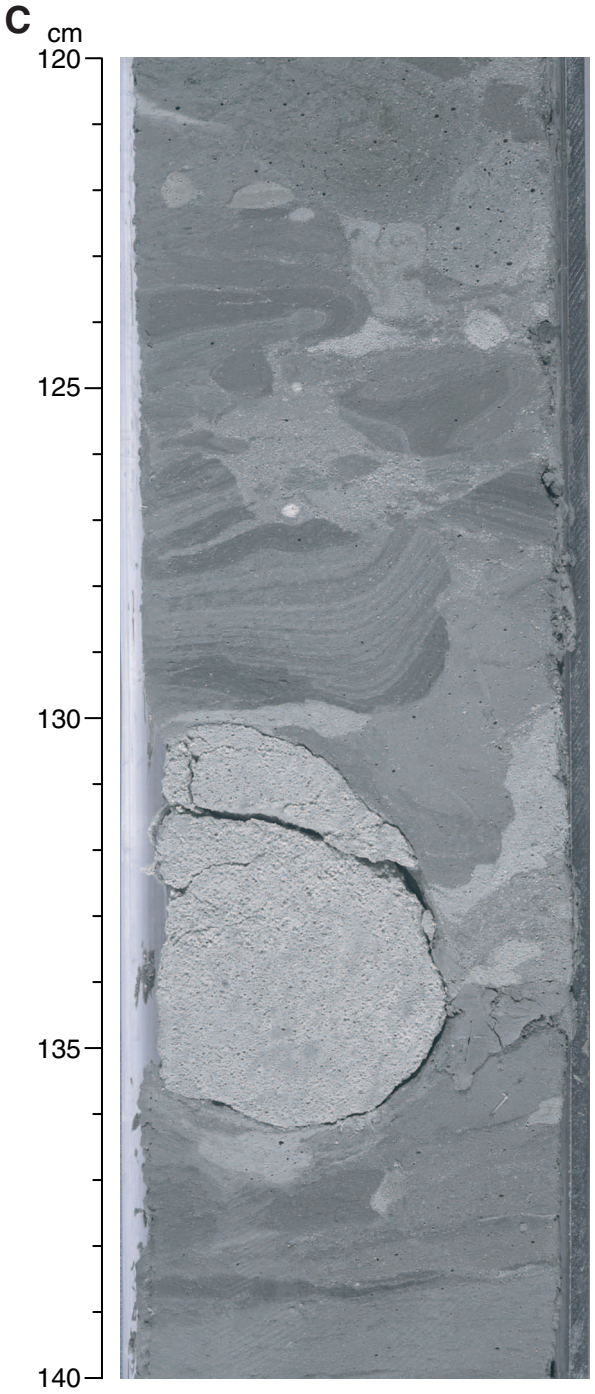

Figure F6. Close-up photographs of representative lithologies for Units II and III at Site 1261. **A.** Cyclic alternations between dark greenish gray calcareous chalks, light greenish gray limestones, and porcellanites seen in Unit II (interval 207-1261A-19R-2, 30–70 cm). **B.** P/E boundary (interval 207-1261A-33R-4, 120–140 cm). A 3-cm-thick greenish gray clay layer and superjacent 12-cm-thick reddish brown clay layer fall in a carbonate-poor interval that contains the P/E boundary. (Continued on next page.)

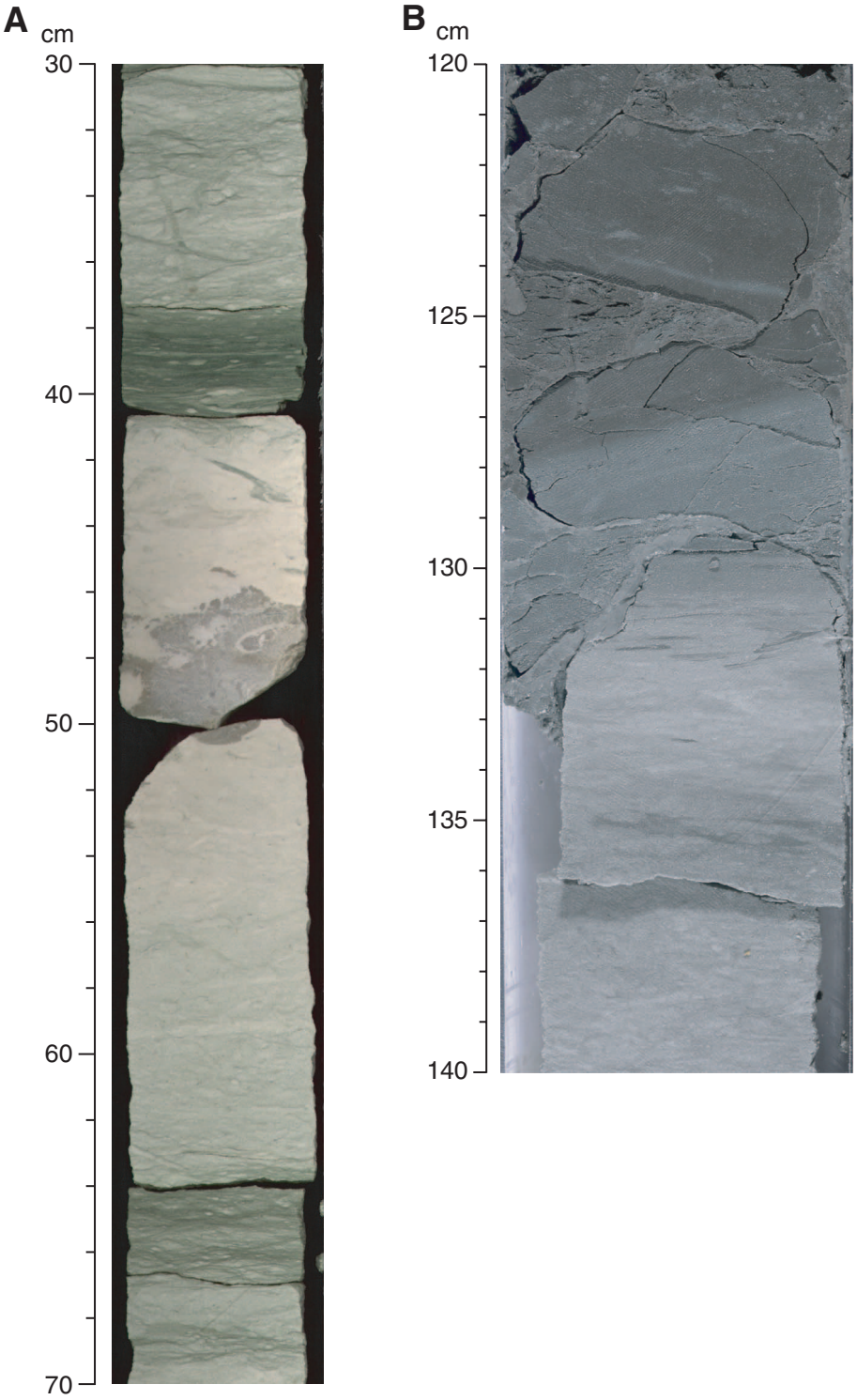

Figure F6 (continued). C. Transition from the glauconitic interval of Subunit IIIB clayey calcareous chalks into the black shale of Unit IV (note large-scale bioturbation of glauconite-rich clayey chalk in the laminated black shale) (interval 207-1261B-5R-4, 100–120 cm).

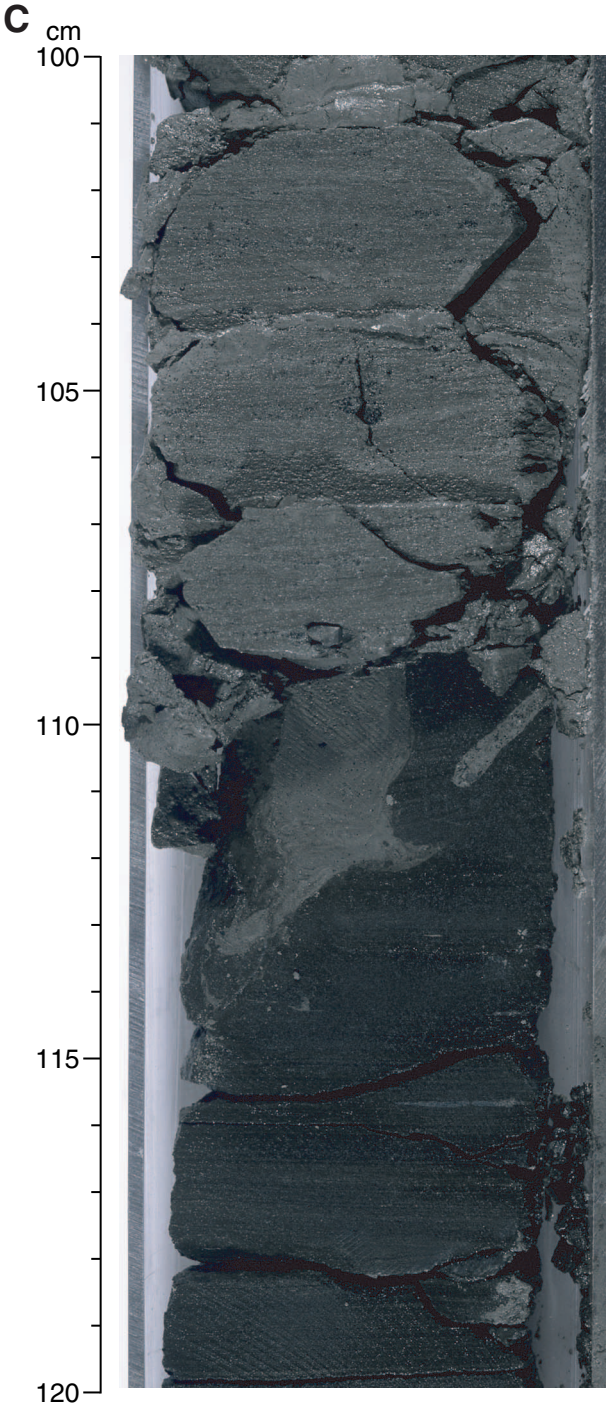

Figure F7. Close-up photographs of representative lithologies from the black shale of Unit IV. **A.** Transition between the two cyclic lithologies of laminated claystone with organic matter and laminated nannofossil chalk in the black shale of Unit IV (interval 207-1261A-47R-1, 84–100 cm). These two lithologies are separated by a bluish layer of coarse-grained diagenetic calcite. The nannofossil chalk is cut by a mineralized vein. **B.** Another bluish layer of coarse-grained diagenetic botryoidal calcite fan precipitated in a black claystone matrix (interval 207-1261B-48R-4, 67–87 cm). (Continued on next page.)

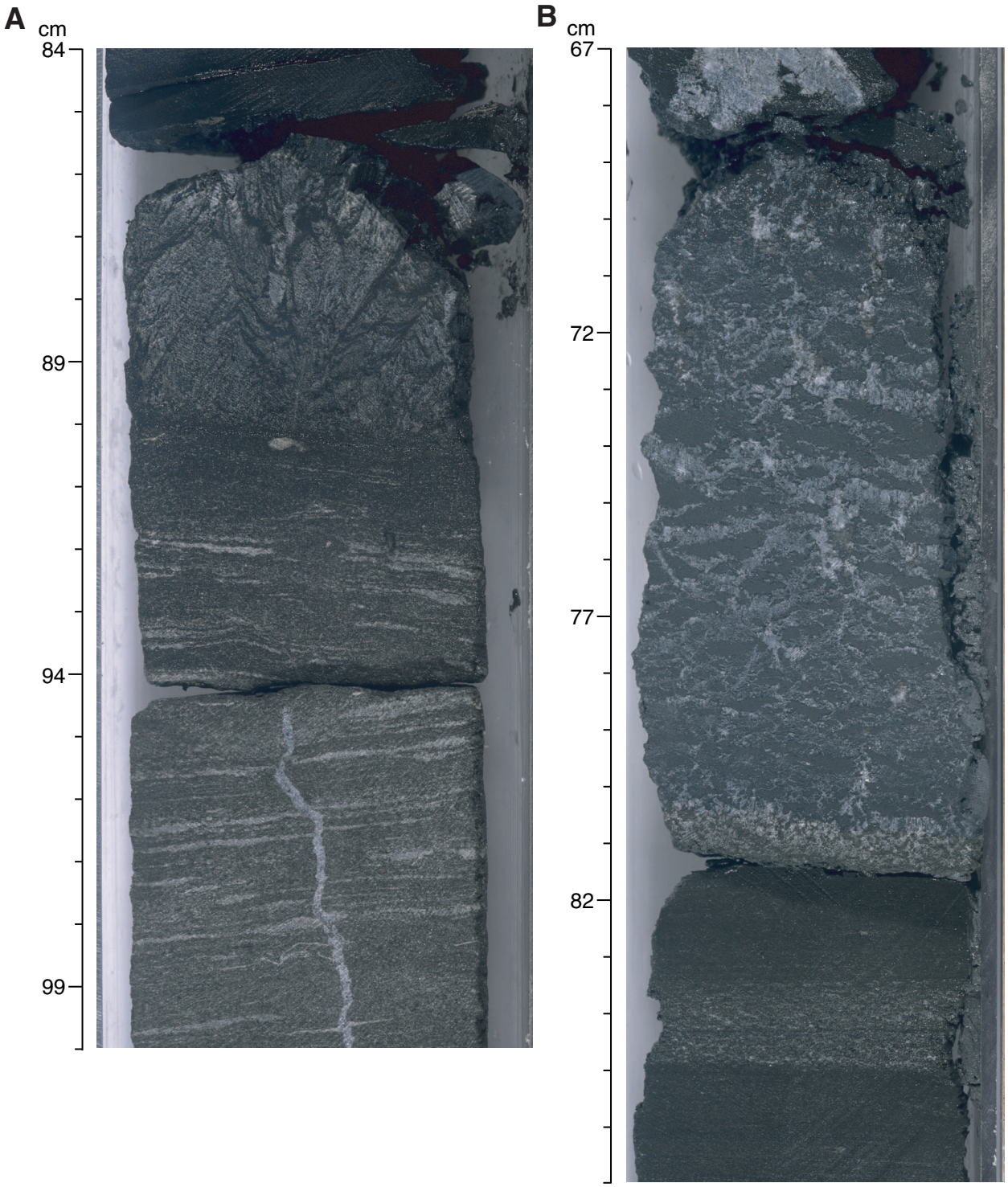

Figure F7 (continued). C. Sharp transition between the laminated black shales of Unit IV and the quartz sandstone of Unit V (interval 207-1261A-50R-3, 13–35 cm).

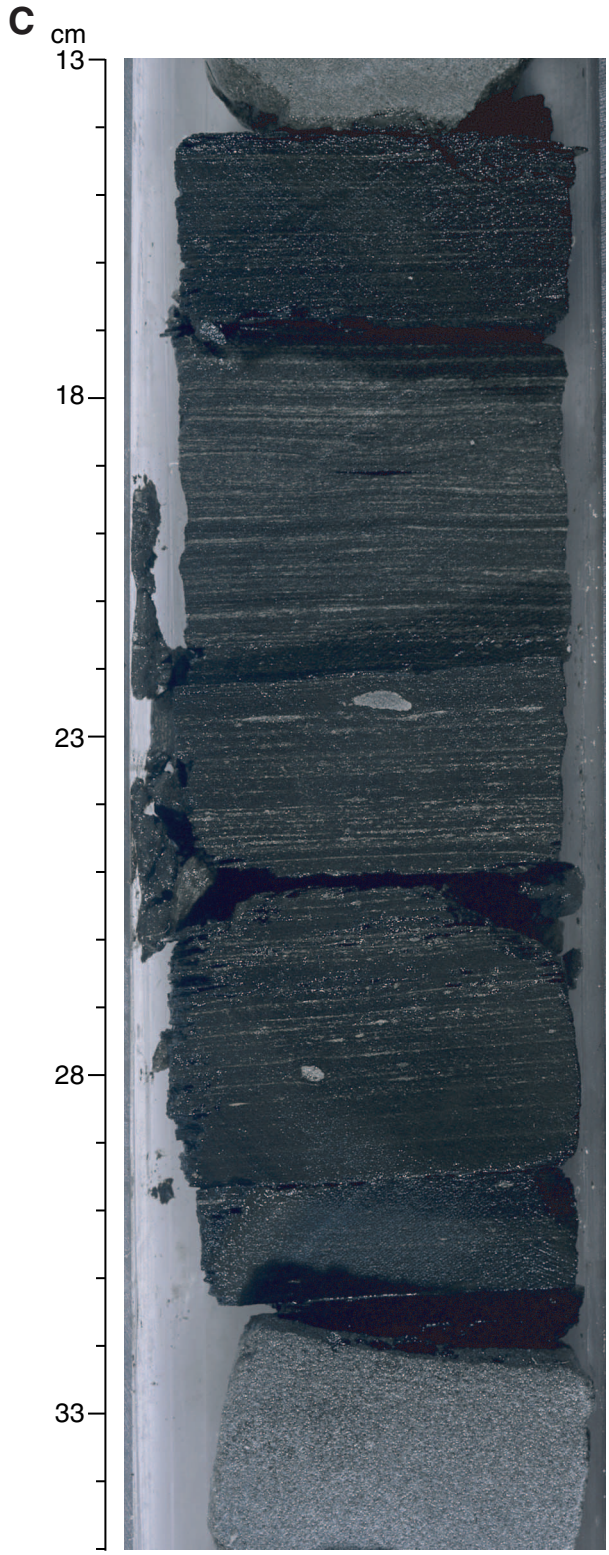

Figure F8. A. Calcareous microfossil and radiolarian biozones at Site 1261. Shaded boxes indicate the absence of microfossils suitable for dating. Dashed line indicates uncertain location of biozone boundary of >10 m. In A, the calcareous nannofossil zonation, Subzones NP9a and NP9b refer to nannofossil assemblages in Zone NP9 above and below the P/E boundary, respectively. (Continued on next page.)

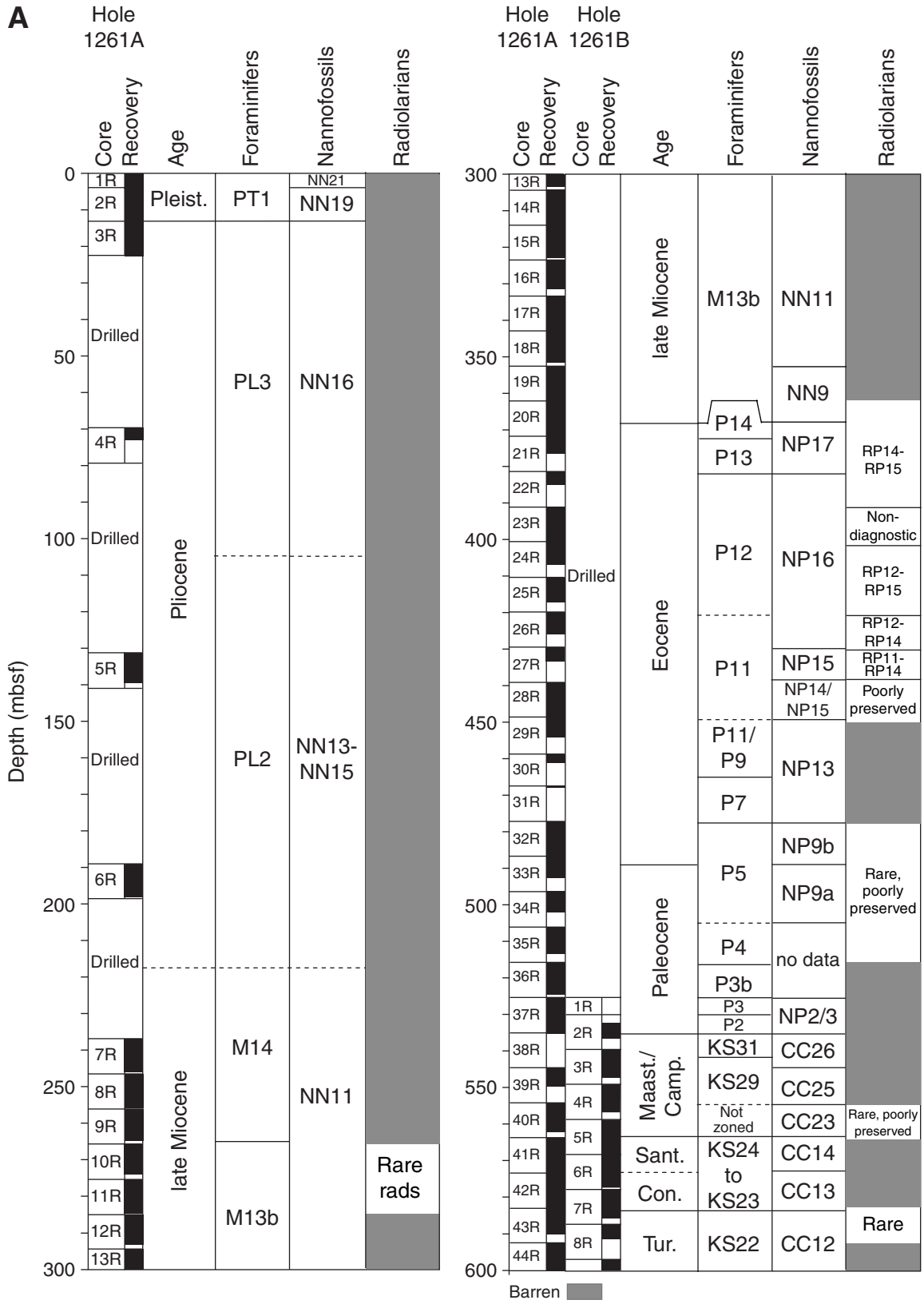

Figure F8 (continued). B. Calcareous microfossil and radiolarian biozones.

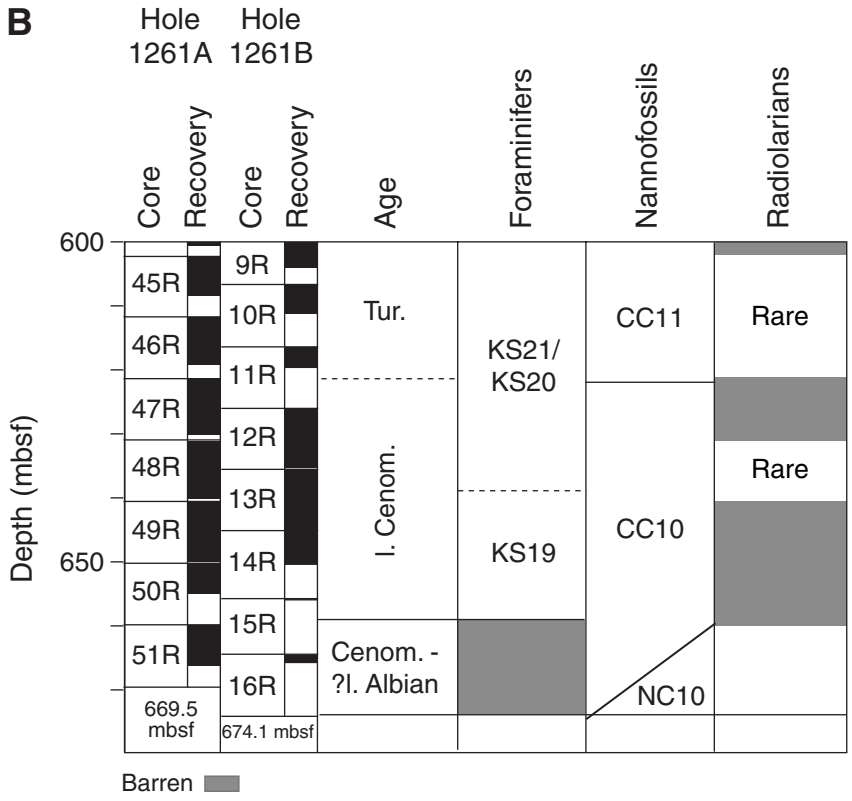

Figure F9. Shipboard paleomagnetic data and initial interpretations of inclination clusters in the Cretaceous–Miocene from Holes 1261A and 1261B. Visual color variations in the sediment succession generally correspond to changes in magnetic properties and are displayed as an exaggerated schematic column to the right of the shipboard lithostratigraphic units. The paleomagnetic data from the holes have been compared using the composite depth offsets, which rarely exceeded a relative displacement of 4 m at this site. Magnetic inclinations (blue points = Hole 1261A and Upper Cretaceous red = Hole 1261B) are from intact blocks (excluding measurements within 5 cm of the end of each blocks) after 15-mT demagnetization. The inclination data exclude measurements near the background noise limit of the cryogenic magnetometer (~3×10^{-5} A/m); therefore, measurements with intensities $<5 \times 10^{-5}$ A/m are not considered reliable. In addition, the upper 20 cm of each core, which commonly displays spurious high-intensity magnetization or downhole contamination, and the upper 5 cm of each section, which is influenced by magnetization carried by the blue end cap, are excluded. The displayed inclinations are either 3-point running means (solid circles), 2-point means (open circles), or single-level data (open triangles) (from the central portion of blocks between 10 and 15 cm long, or from isolated levels within a larger block in which the adjacent measurements were $<5 \times 10^{-5}$ A/m). The magnetic intensity column includes NRM (small orange dots = 21-point running mean) and after the 15-mT demagnetization (small black dots, where large blue dots are 101-point log-mean average) for Hole 1261A. Magnetic susceptibility data for Hole 1261A obtained using a magnetic susceptibility core logger (MSCL) are shown by green dots in the rightmost column. Shipboard assignment of polarity zones was based on clusters of magnetic inclinations from intact blocks (to right of polarity zone column), as delimited by the thin lines. Zones of positive inclinations (originally considered to be normal polarity zones) = black or medium gray, if reliability is less certain; negative or mixed inclinations (originally considered to be reversed polarity zones) = white or light gray, if reliability is less certain. Uncertain inclination characteristics or gaps in data coverage = cross hatched. The shipboard interpretations of polarity zones were not always supported by analyses of magnetic characteristics during progressive thermal demagnetization of minicores (Fig. **F10,** p. 52). F = foraminifers, N = nannofossils, R = radiolarians. (This figure is available in an **oversized format.**)

Figure F10. Magnetostratigraphy and characteristic directions of Campanian–middle Eocene sediments from Holes 1261A and 1261B based on shore-based analysis of minicores. The minicore data from the two holes have been merged using composite depth scales from each hole. Polarity ratings are graded according to reliability and number of vectors utilized in the characteristic direction. R = reliable reversed polarity, INT = indeterminate, N = reliable normal polarity) (relative placement of other points indicates degree of precision or uncertainty). Methods of polarity interpretation, polarity ratings, and derivation of characteristic inclinations and intensities are in "**Paleomagnetism**," p. 16, in the "Explanatory Notes" chapter. Polarity zones are assigned according to clusters of individual polarity interpretations. Normal polarity zones = dark gray; reversed polarity zones = white; uncertain polarity or gaps in data coverage = cross hatched. Assignments of polarity chrons are based on the polarity zone pattern and the constraints from microfossil biostratigraphy. (**Figure shown on next page.**)

Figure F10 (continued). (Caption shown on previous page.)

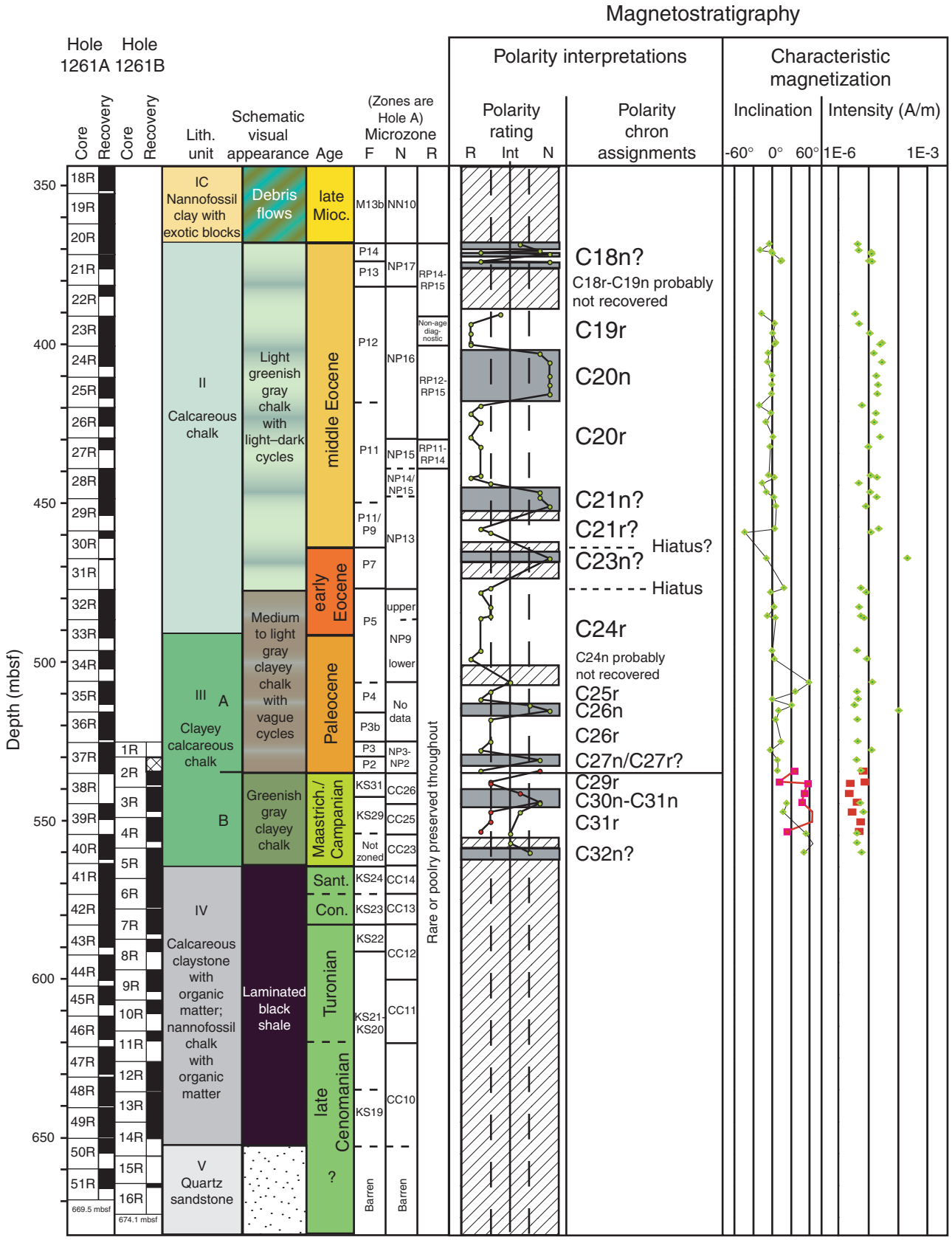

Figure F11. Composite and spliced gamma ray attenuation (GRA) bulk density data for the black shale sequence of Holes 1261A (black) and 1261B (blue). The composite data from Hole 1261B are offset by a constant (0.5 units) for illustration purposes. All data sets are smoothed with a 9-point Gaussian filter.

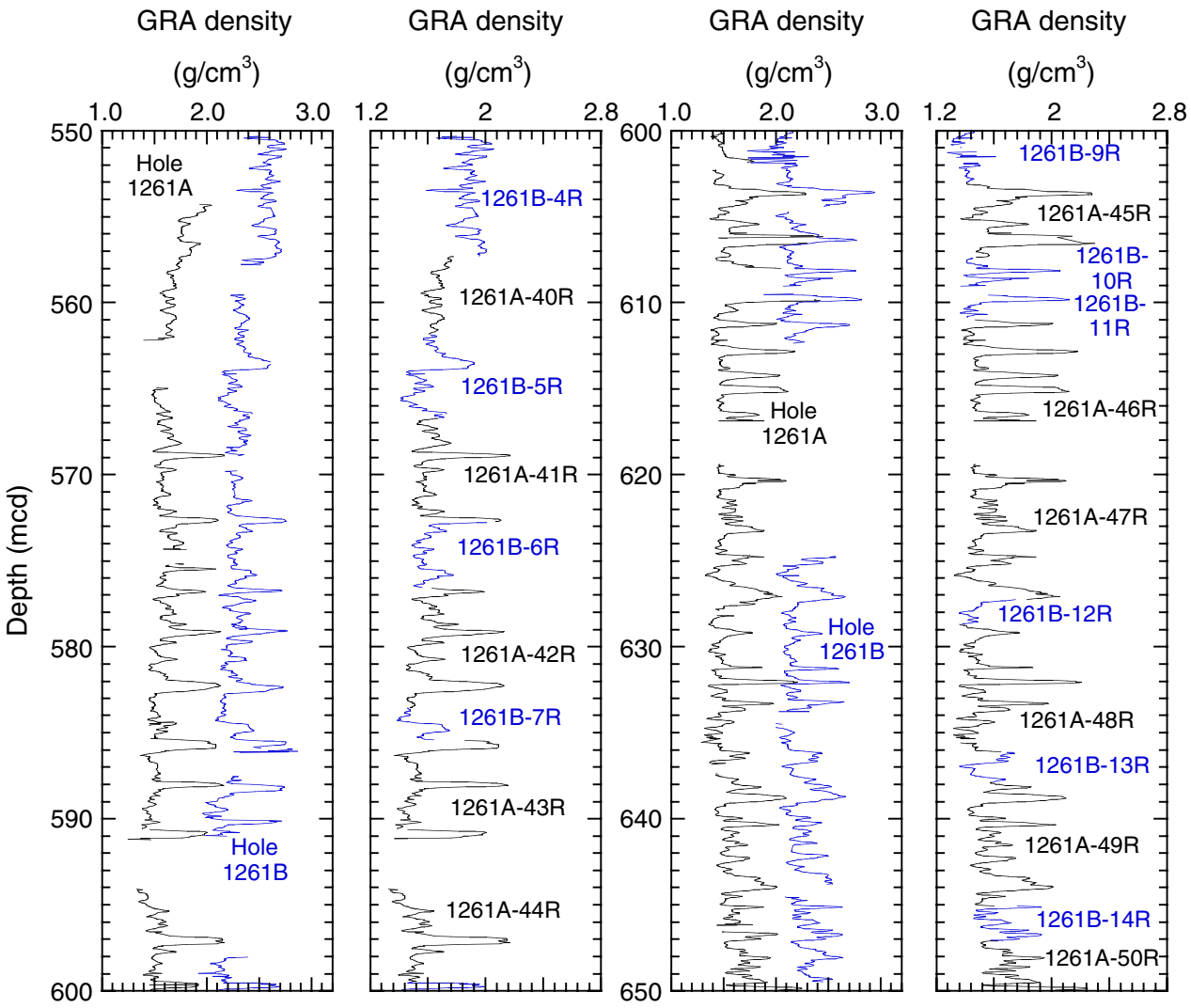

Figure F12. Age-depth plot combining all available biostratigraphic and magnetostratigraphic datums from Hole 1261A. Rates shown in black are calculated sedimentation rates for the five intervals with approximately linear sedimentation rates based on a linear fit to datums within each interval. Text in red is the estimated duration of six apparent breaks in sedimentation between those intervals of approximately constant sedimentation. The Albian age for Unit V represents a maximum age based on nannofossils (see Table T11, p. 89) but is consistent with ages estimated for Unit V at other sites.

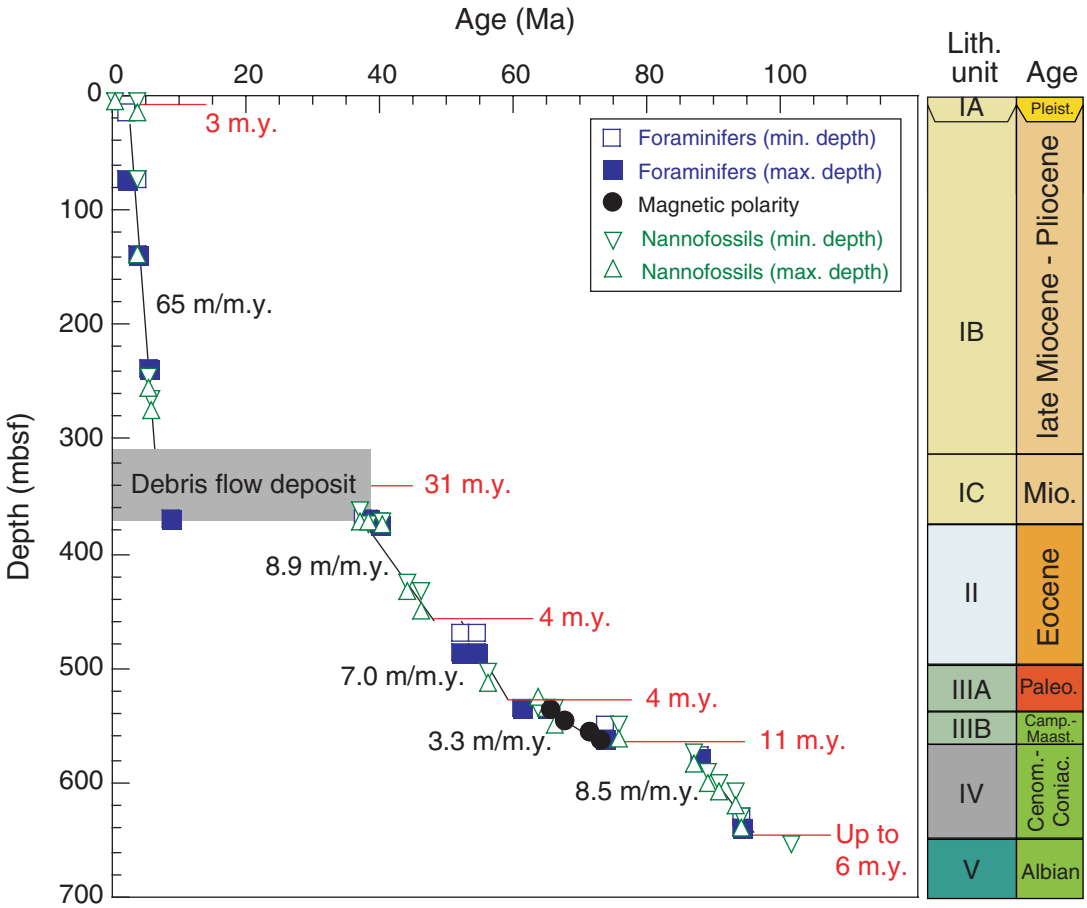

Figure F13. Rock-Eval van Krevelen-type diagram of sediment samples from Holes 1261A and 1261B. Organic matter appears to be predominantly Type II algal material for Unit IV. The value located in the gray shaded area in the graph belongs to Unit V. TOC = total organic carbon.

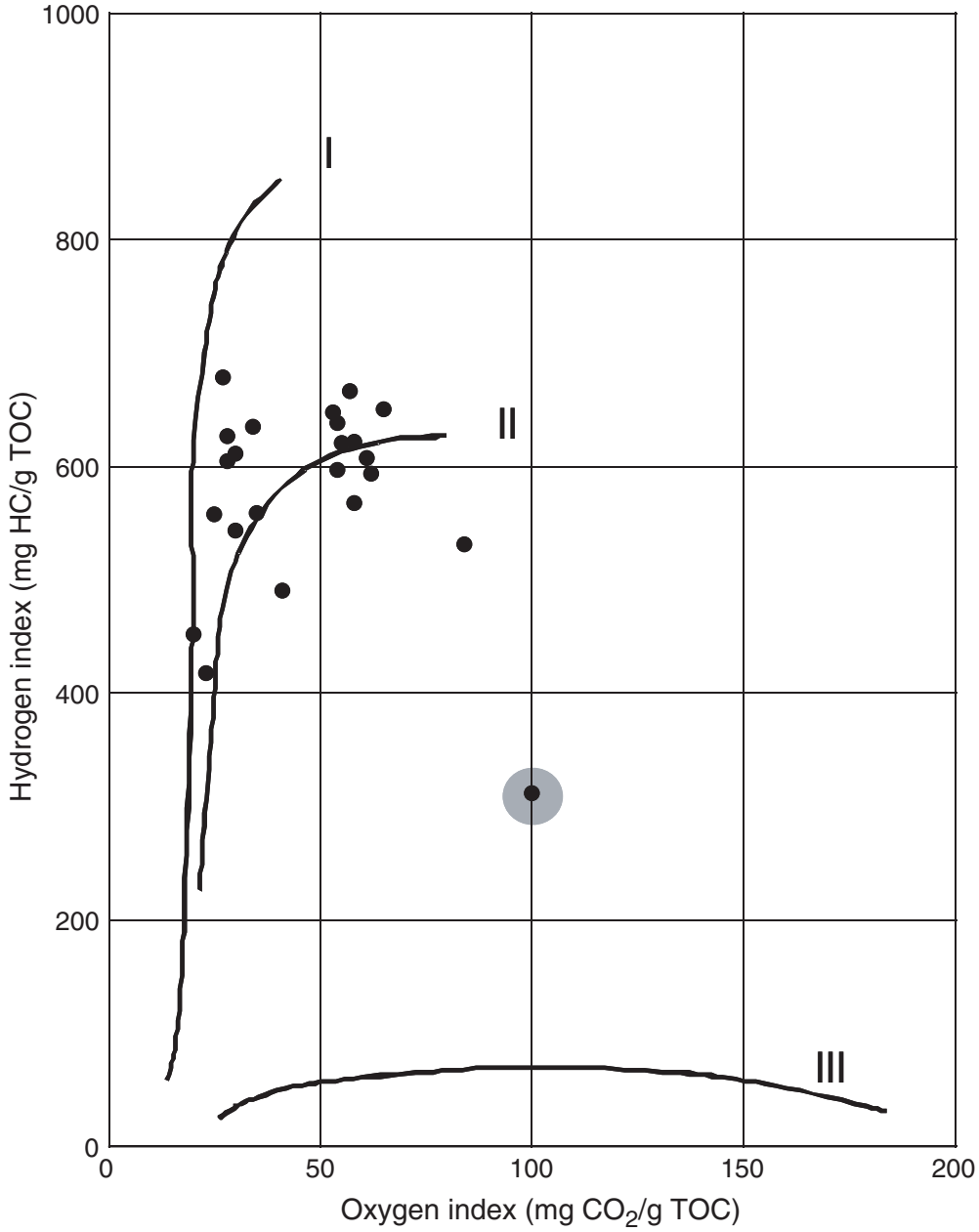

Figure F14. Comparison of concentrations of routine headspace gas (HS) and microbial methane analyses.

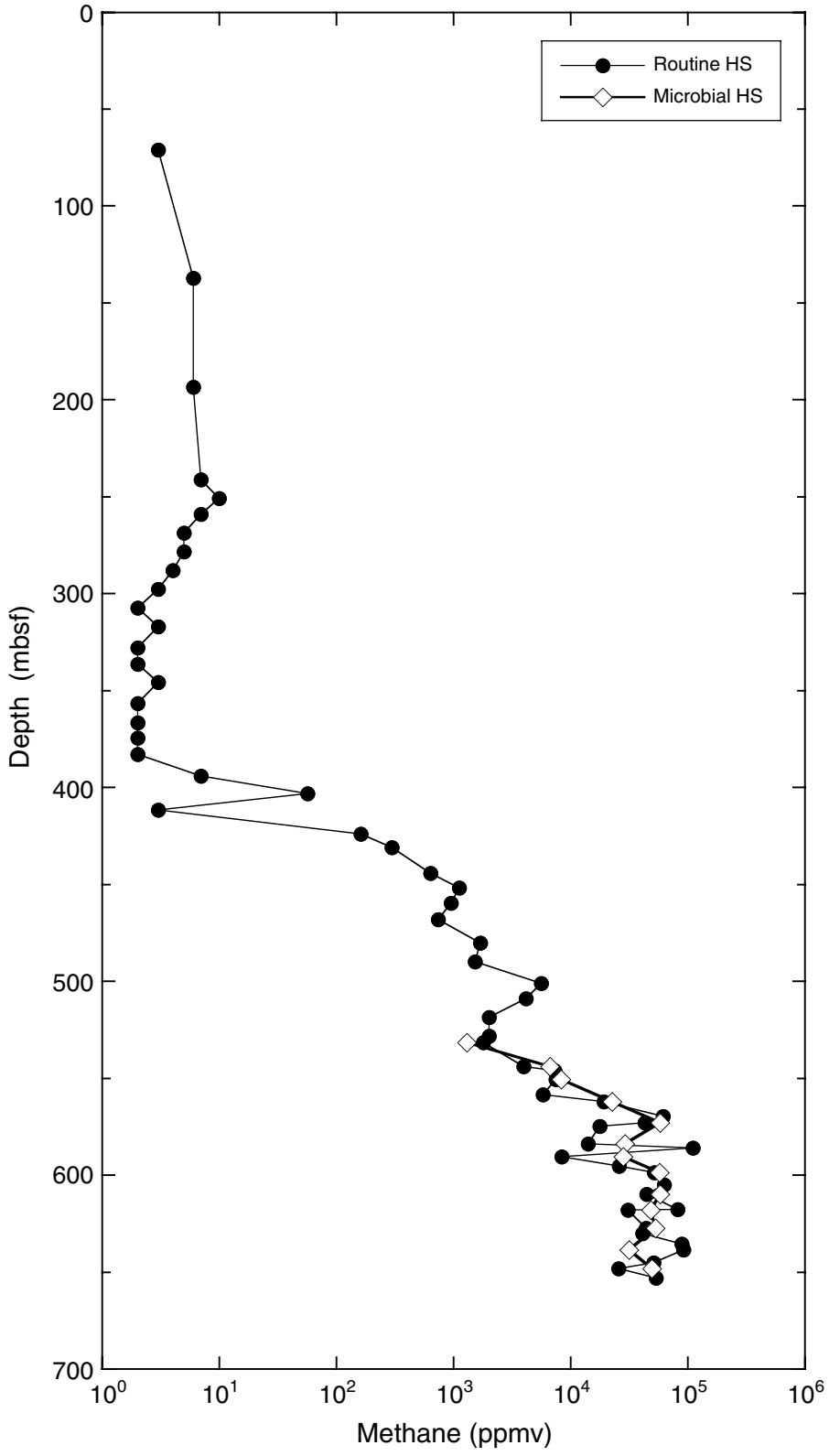

Figure F15. Interstitial water chemistry profiles. **A.** Salinity. **B.** Chloride. **C.** Sodium. **D.** Potassium. **E.** Alkalinity. **F.** Sulfate. **G.** Ammonium. **H.** Barium. (Continued on next two pages.)

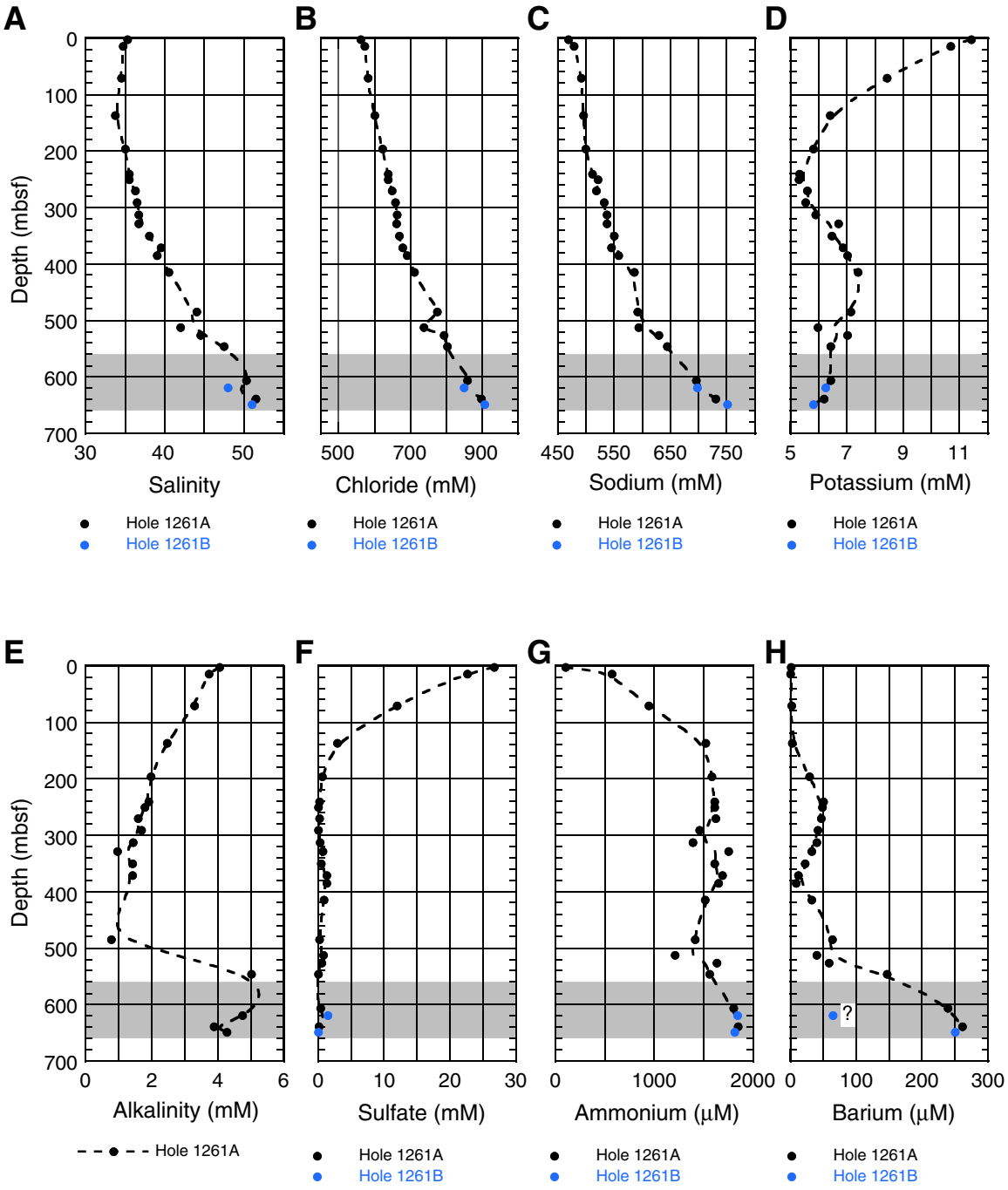

Figure F15 (continued). I. Calcium. **J.** Strontium. **K.** Magnesium. **L.** Lithium. **M.** Boron. **N.** Silicon. **O.** Iron. **P.** Manganese.

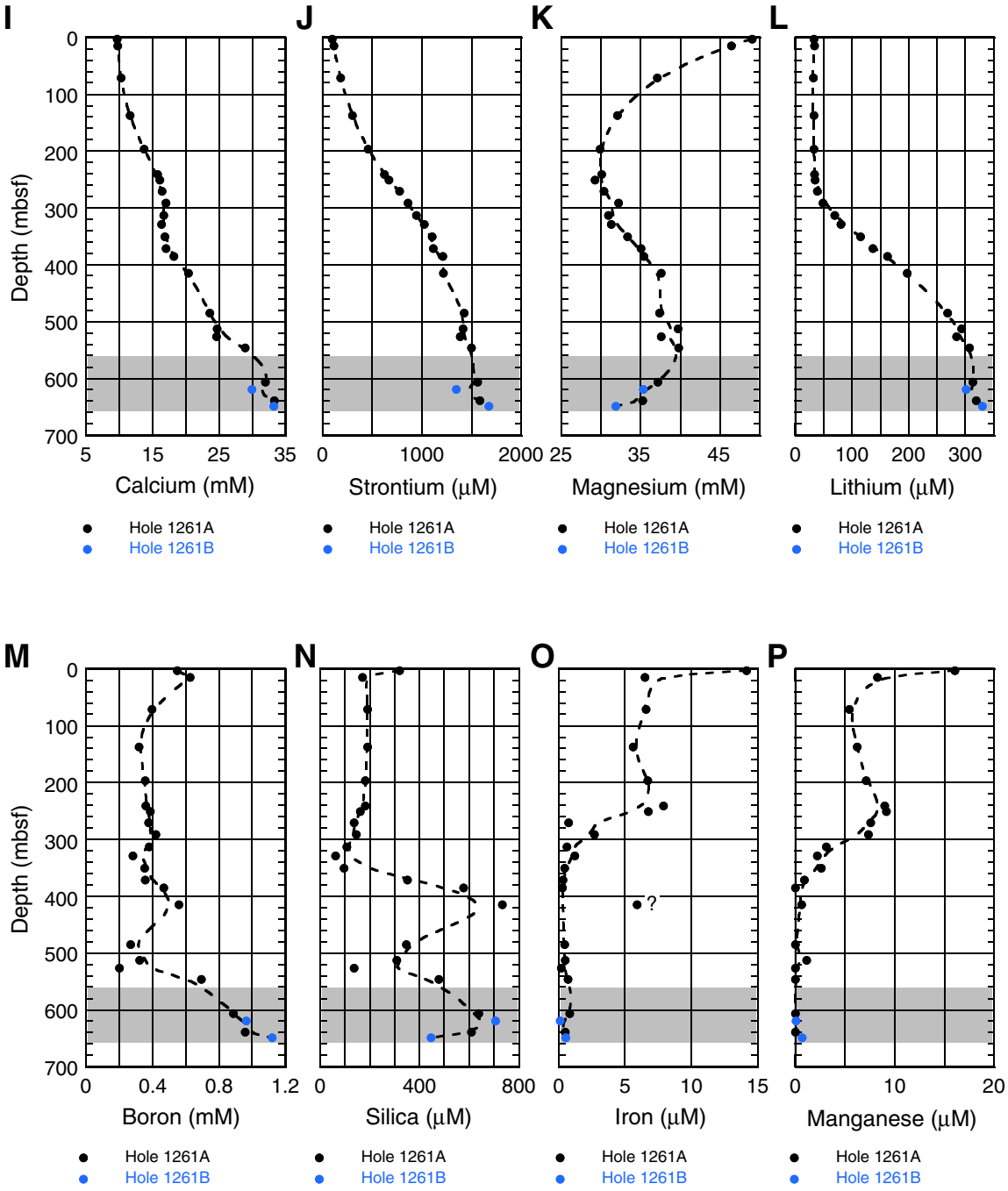

Figure F15 (continued). Element ratios. **Q.** Mg/Cl. **R.** K/Cl. **S.** Ca/Cl. **T.** Sr/Cl. **U.** Li/Cl. **V.** Na/Cl. Shaded bar = black shale Unit IV.

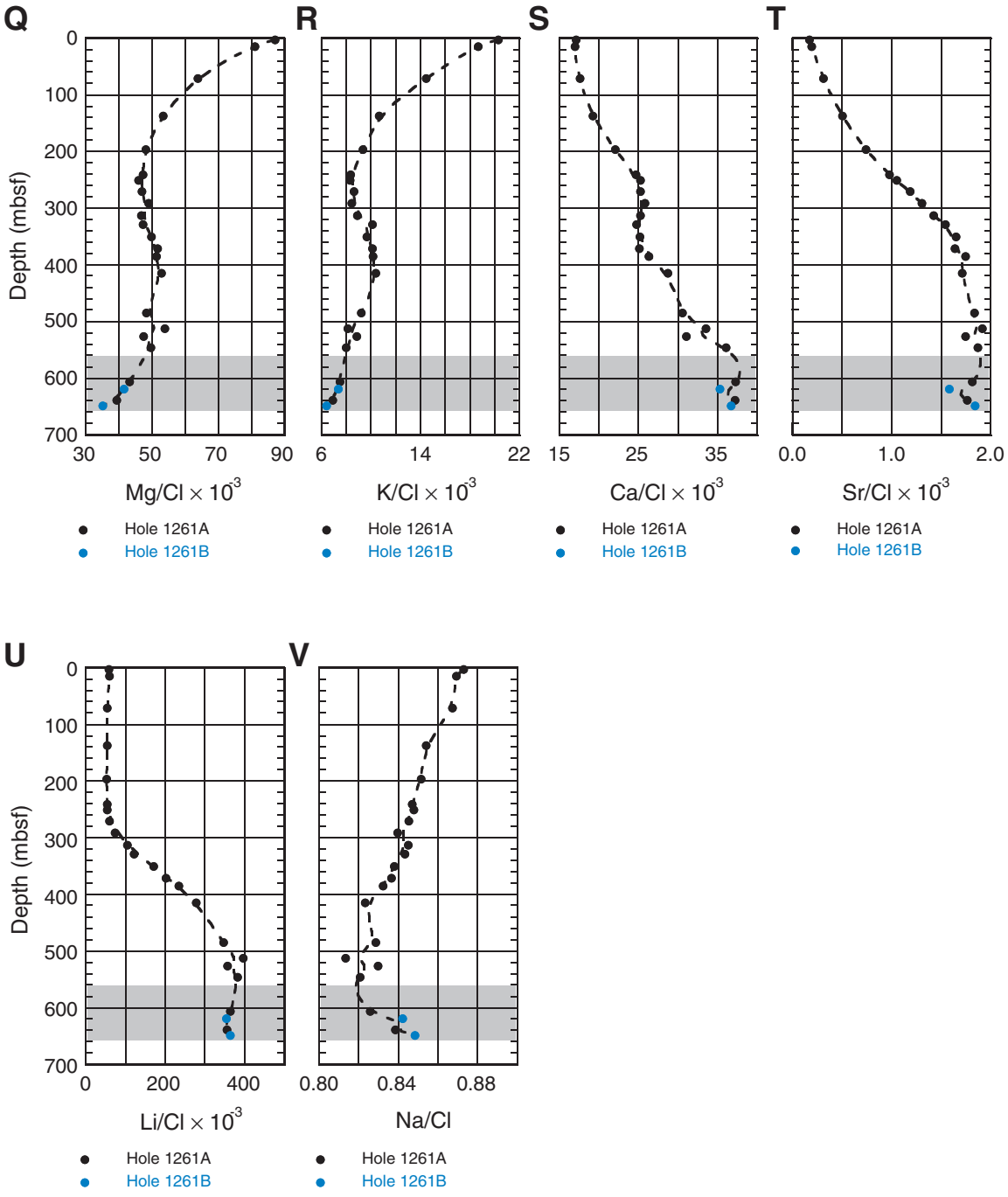

Figure F16. Mg/Cl vs. K/Cl.

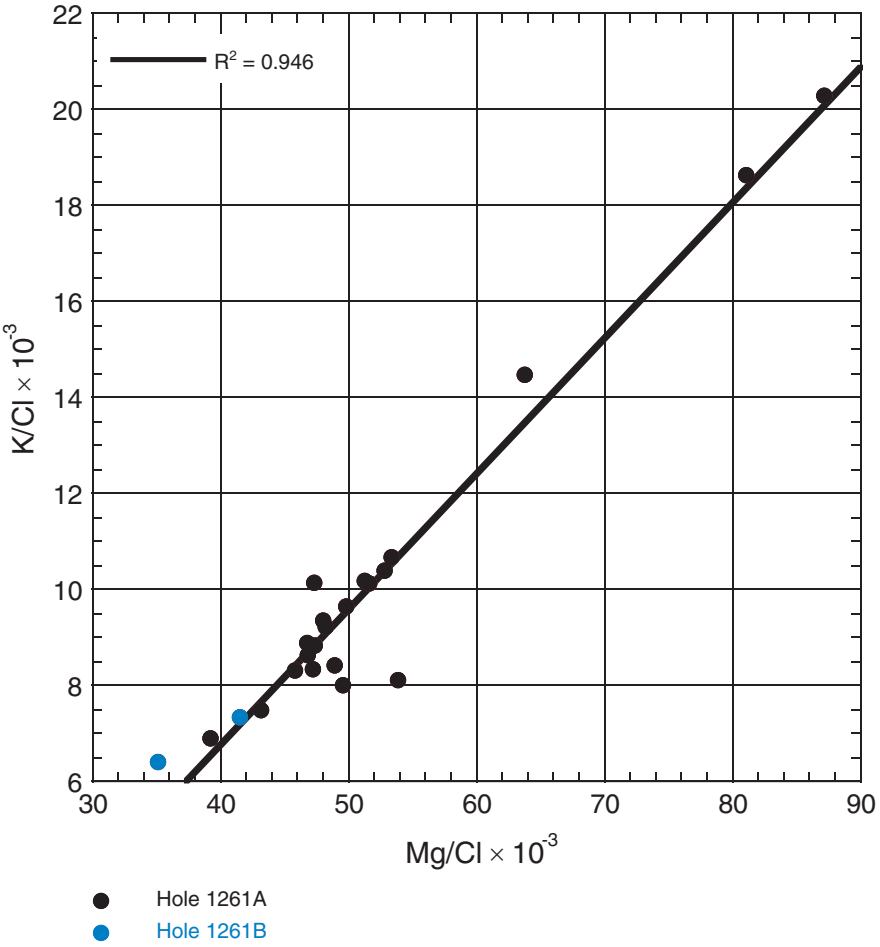

Figure F17. Sr vs. Ca.

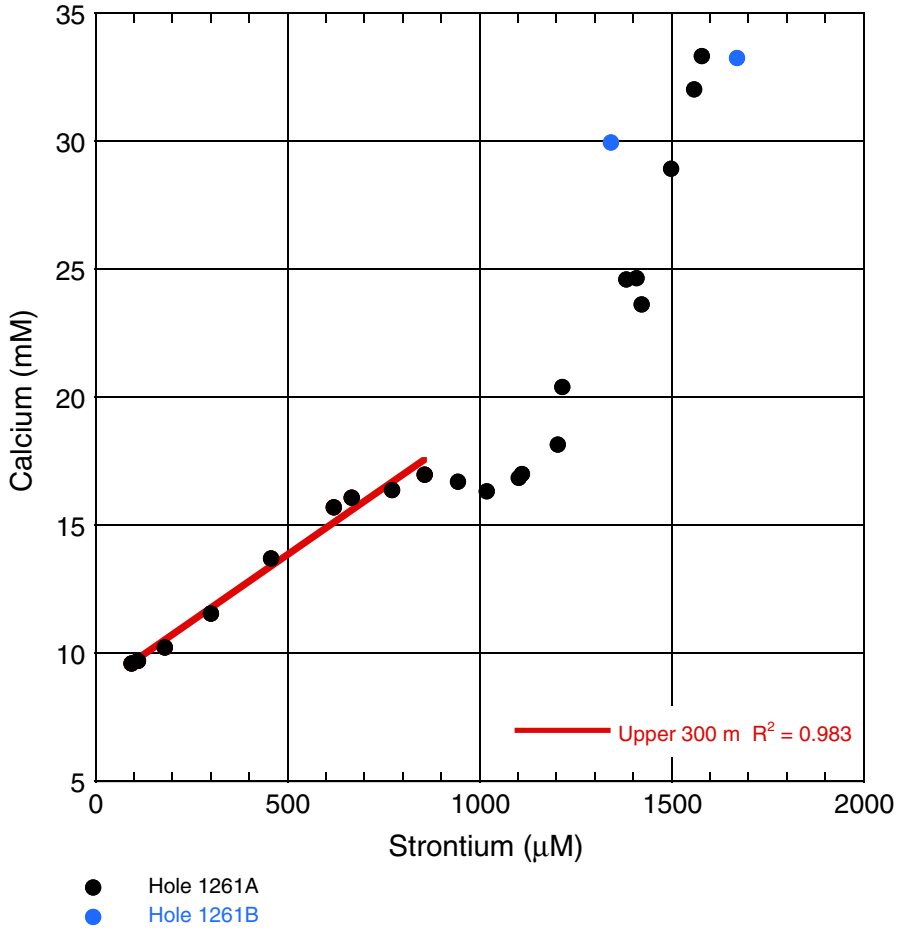

Figure F18. Bulk density, grain density, and porosity of discrete samples from Site 1261. Blue = Hole 1261A, green = Hole 1261B.

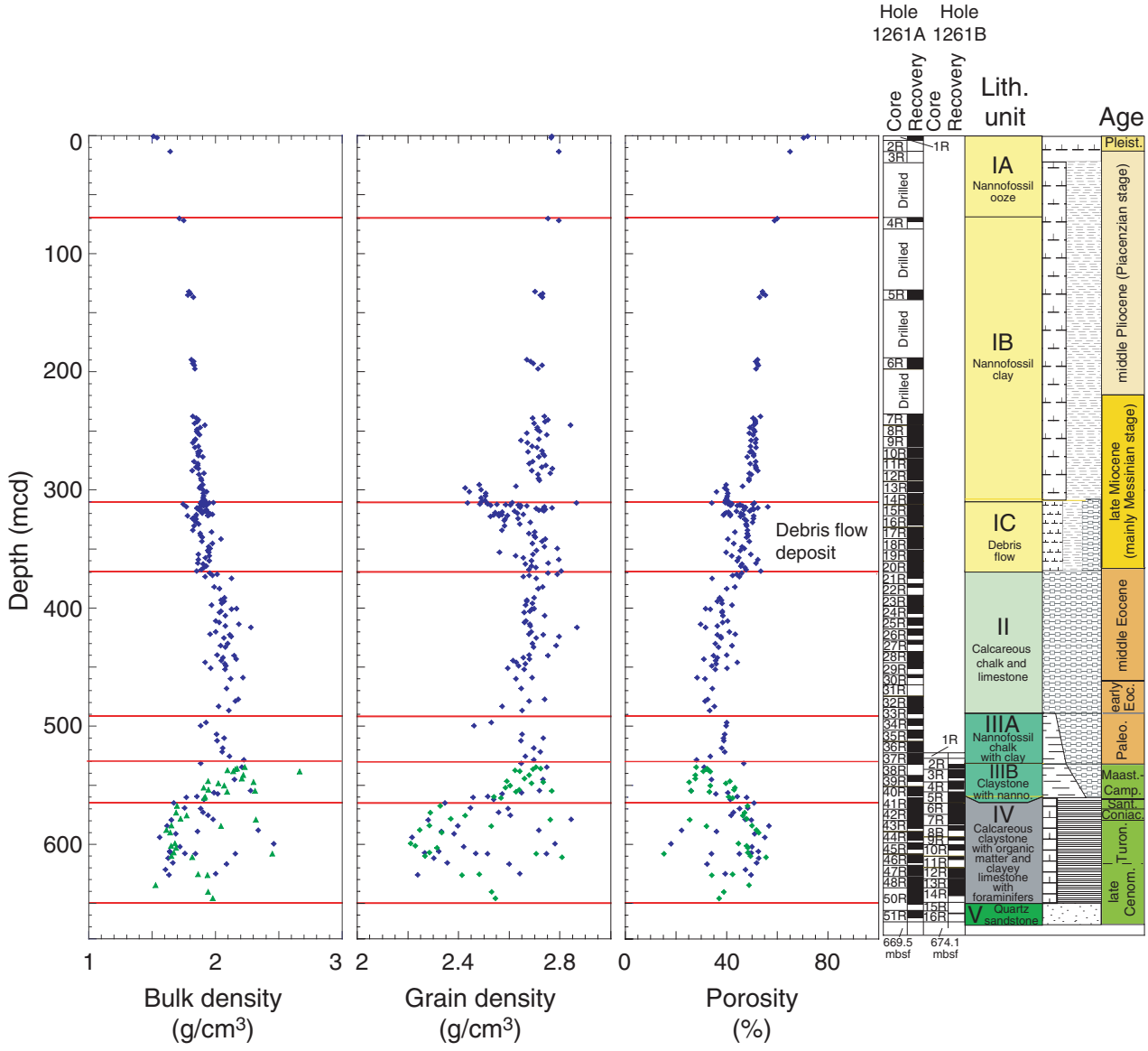

Figure F19. Acoustic velocity and velocity anisotropy measured in Hole 1261B.

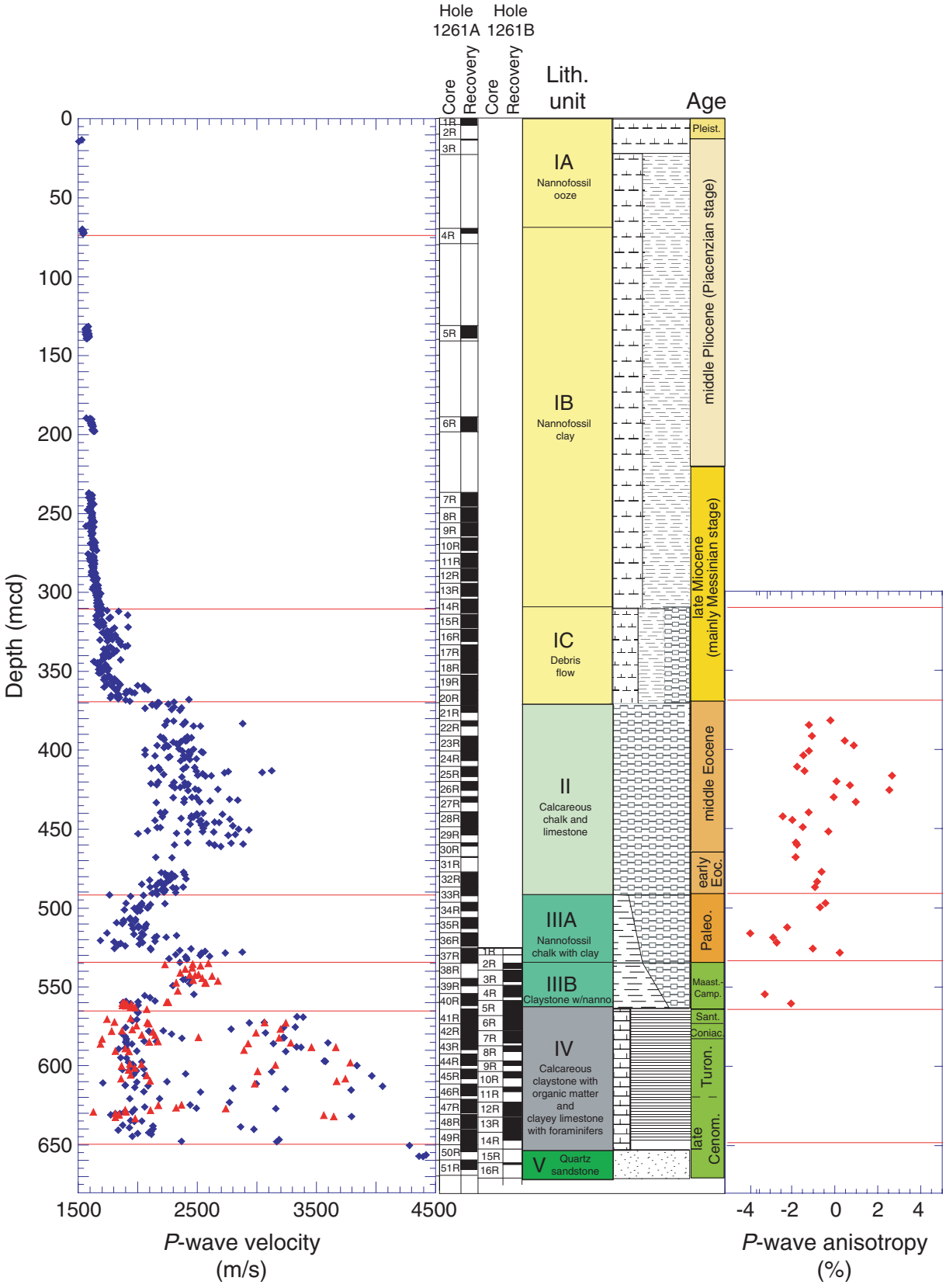

Figure F20. MST data with lithostratigraphic units from Holes 1261A (blue) and 1261B (green). Data have been smoothed using a 75-cm inverse-distance weighted moving window. NGR = natural gamma ray, GRA = gamma ray attenuation.

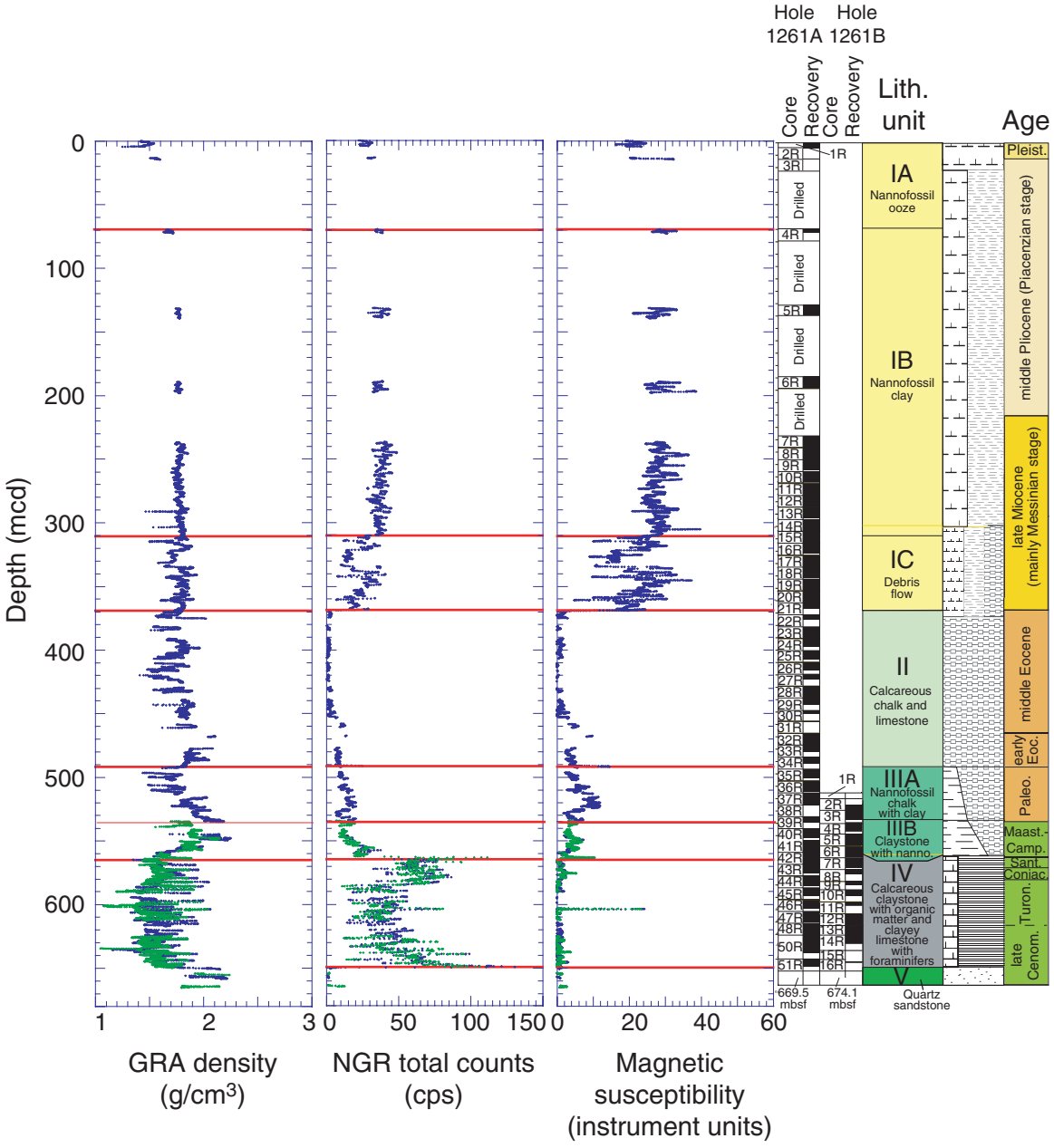

Figure F21. Summary of logging runs in Hole 1261B. MGT = Multi-Sensor Spectral Gamma Ray Tool, FMS = Formation MicroScanner, WST = Well Seismic Tool, P = pass.

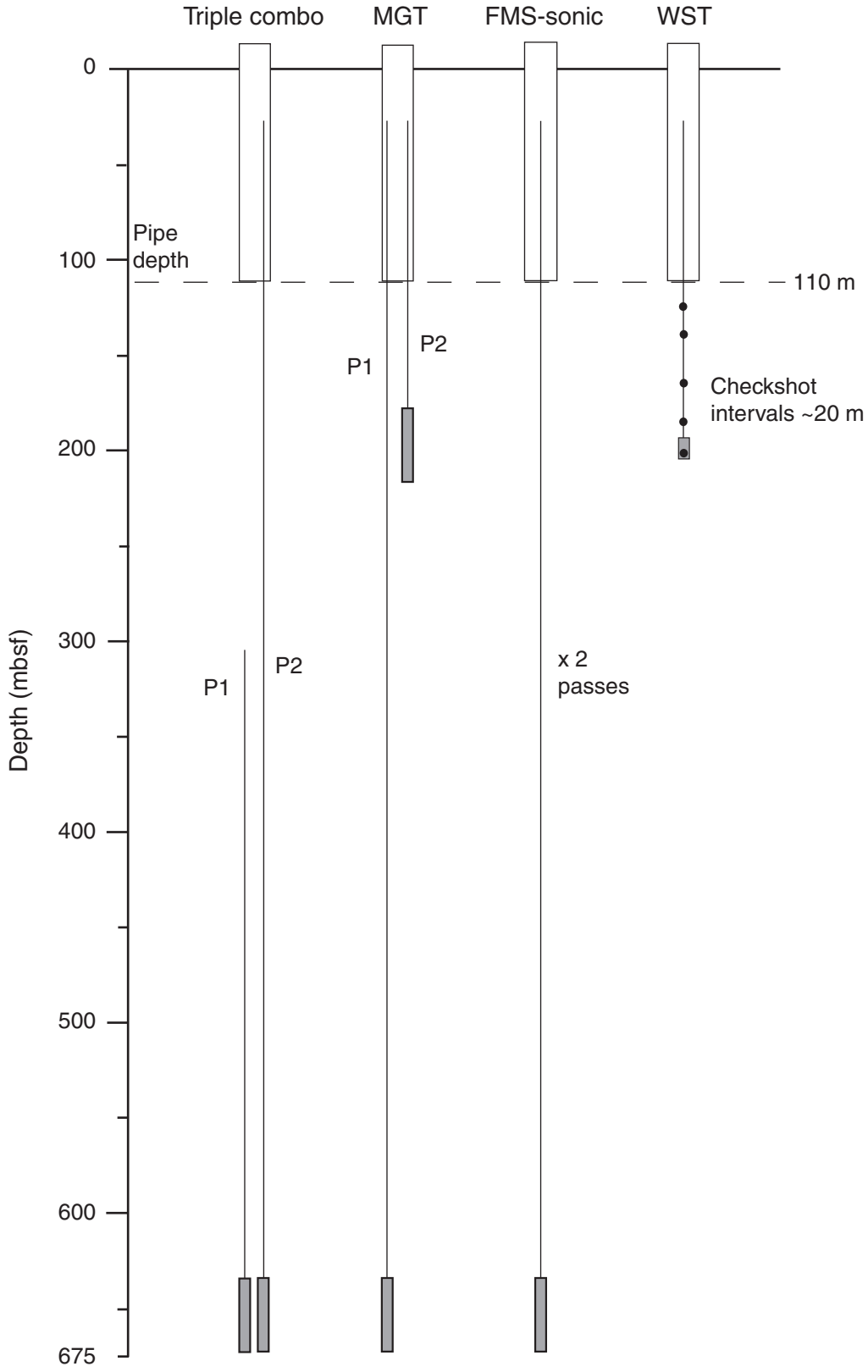

Figure F22. Borehole caliper logs from two passes of the triple combination (TC) and Formation MicroScanner (FMS)-sonic tool strings. P = pass.

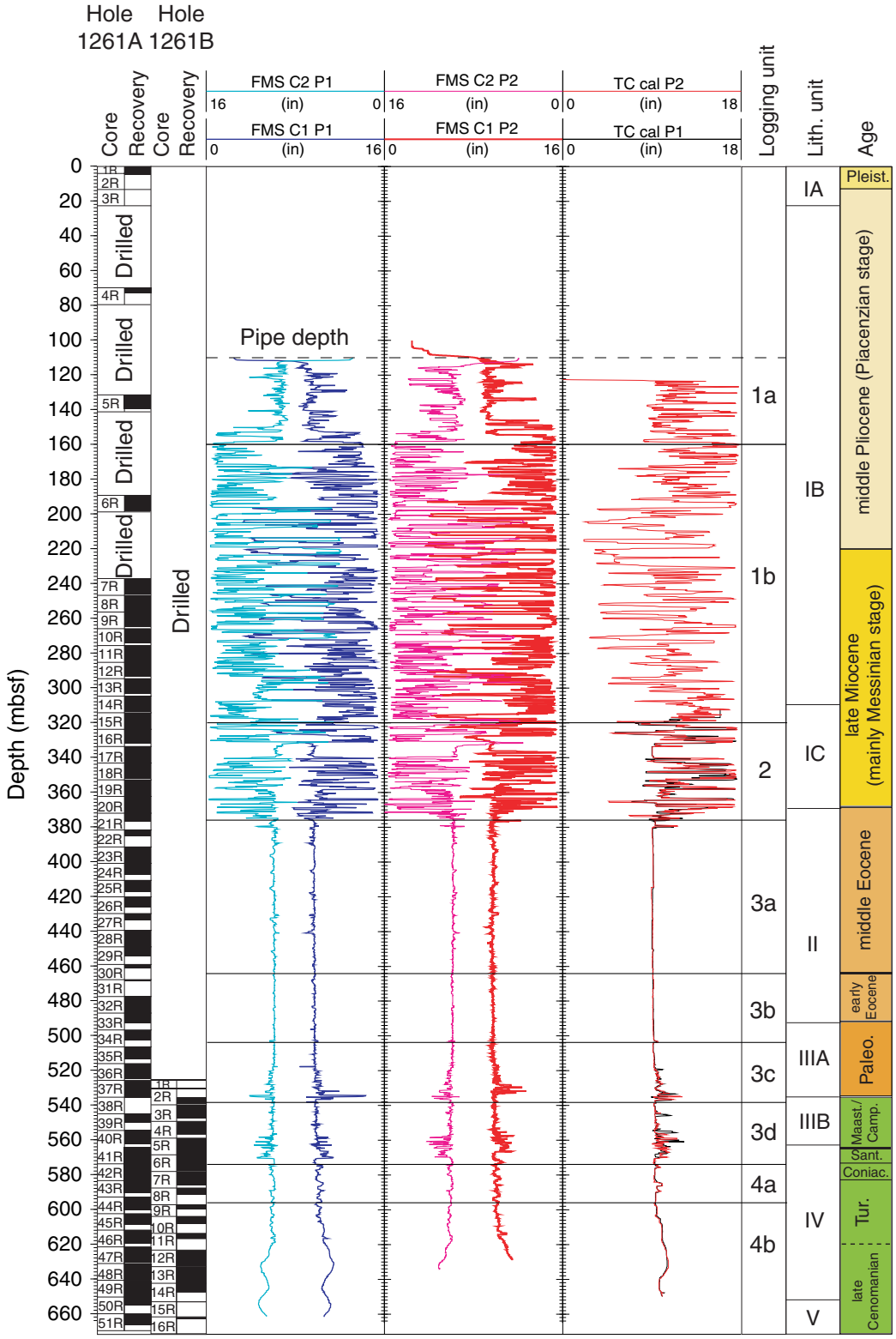

Figure F23. Geophysical logs from Hole 1261B and equivalent core physical properties from Hole 1261A. MGT = Multi-Sensor Spectral Gamma Ray Tool.

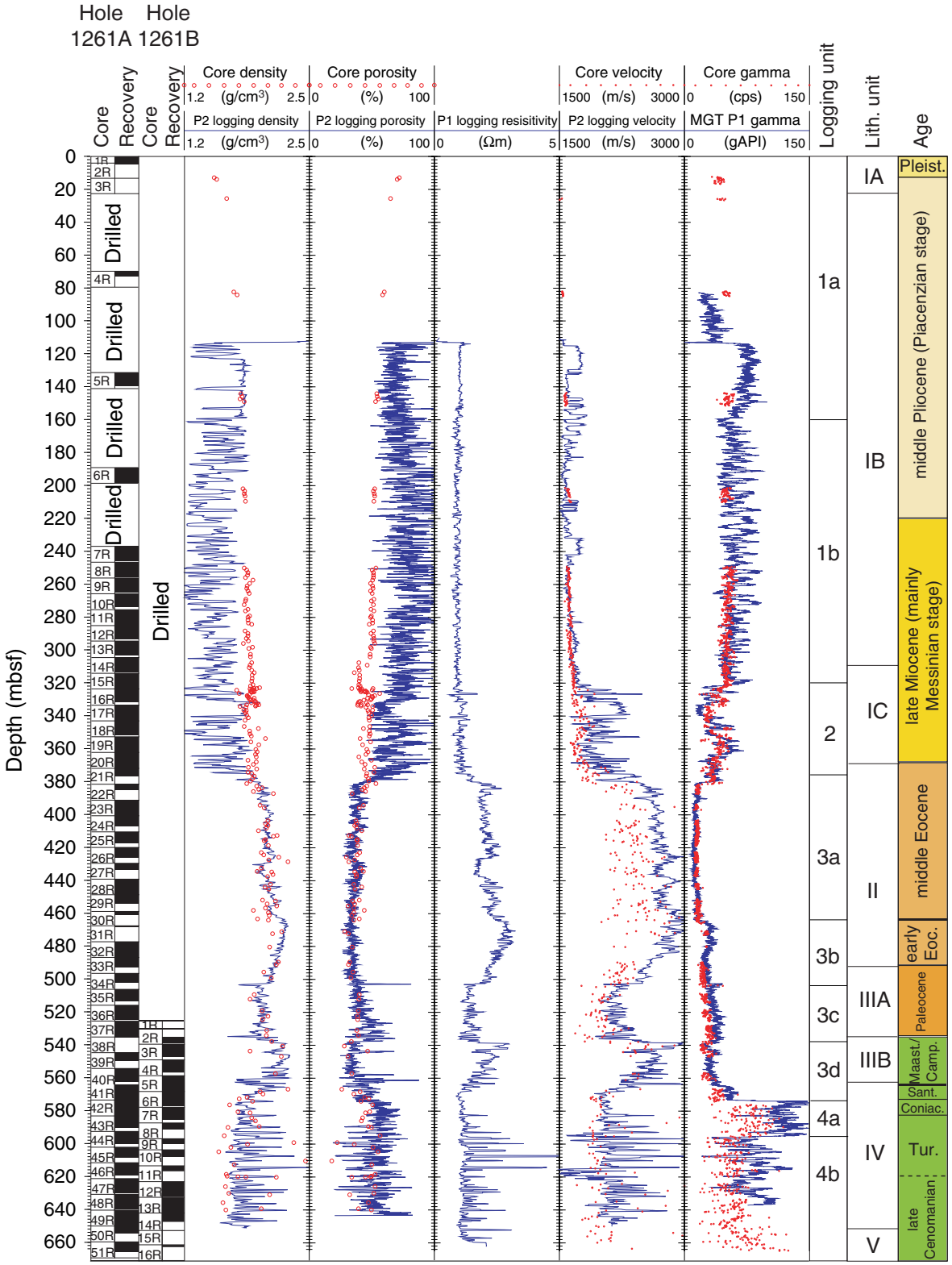

Figure F24. Geophysical logs, caliper data, and logging units from Hole 1261B. TC = triple combination, P = pass, FMS = Formation MicroScanner, MGT = Multi-Sensor Spectral Gamma Ray tool, HSGR = HNGS standard (total) gamma ray, PEF = photoelectric effect.

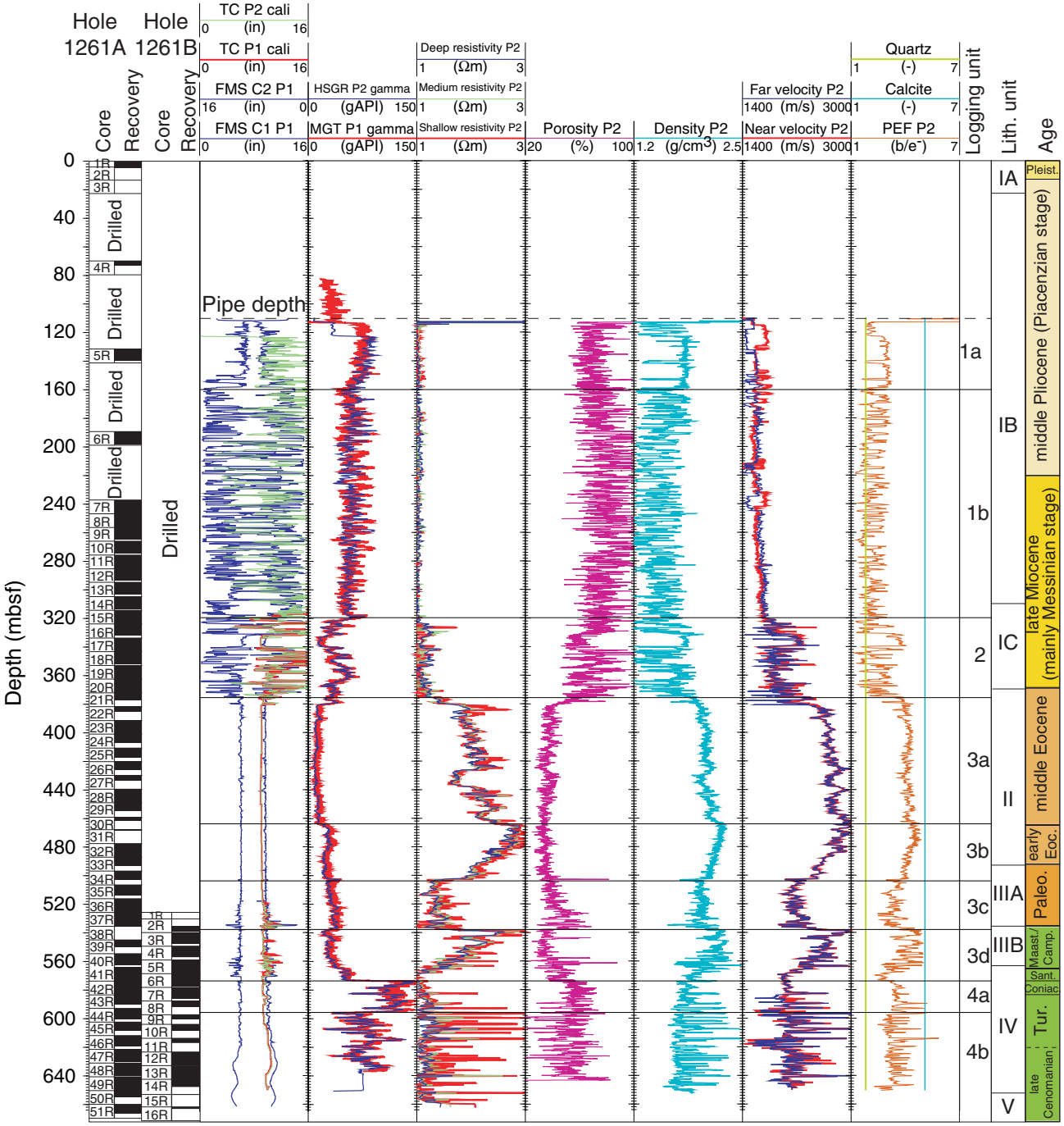

Figure F25. High-resolution MGT gamma ray logs from Hole 1261B. CGR = computed gamma ray.

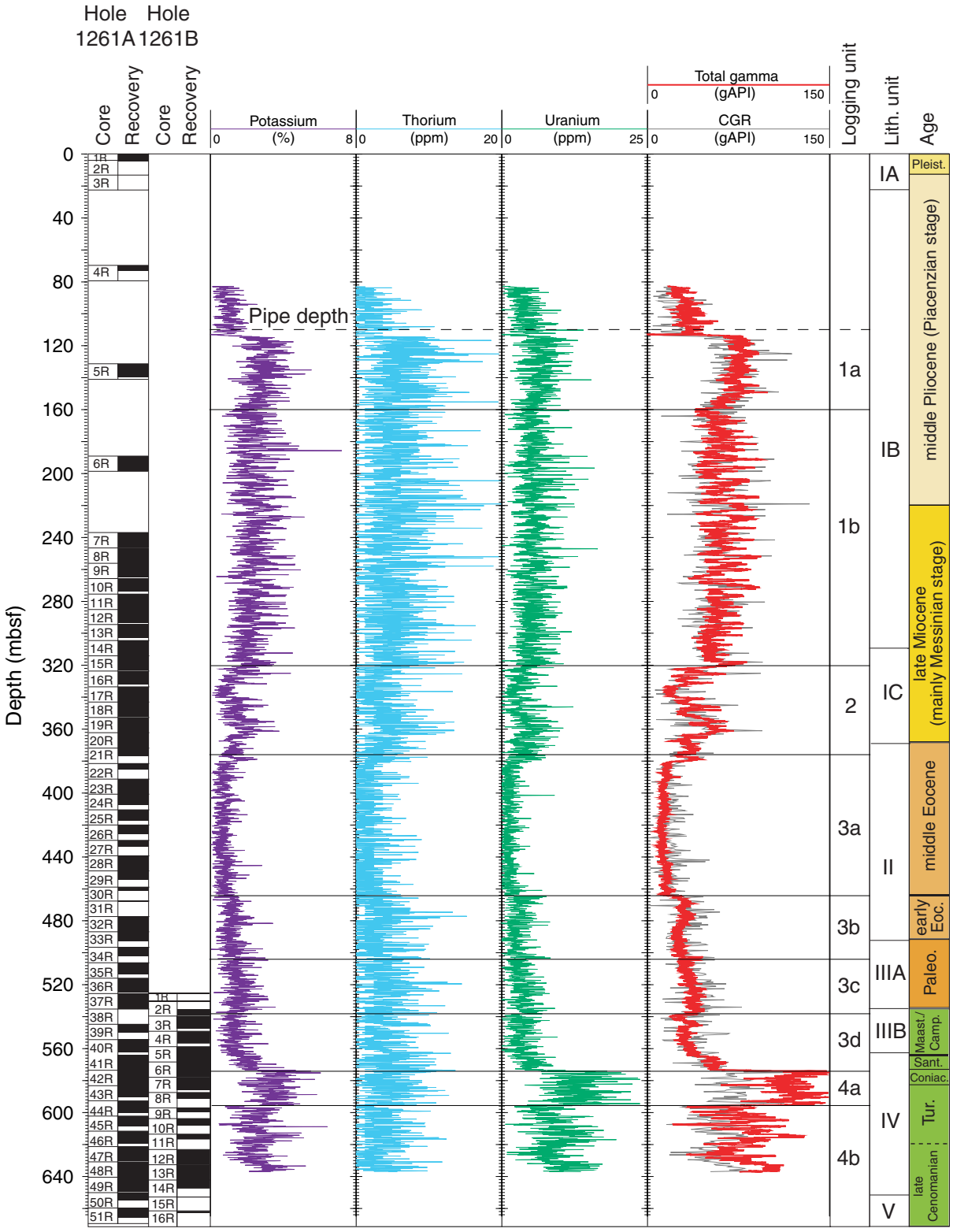

Figure F26. Triple combo (TC) caliper, Multi-Sensor Spectral Gamma Ray Tool (MGT) gamma, and core gamma ray data, highlighting the relationship between the clay-rich layers and under-gauge hole locations.

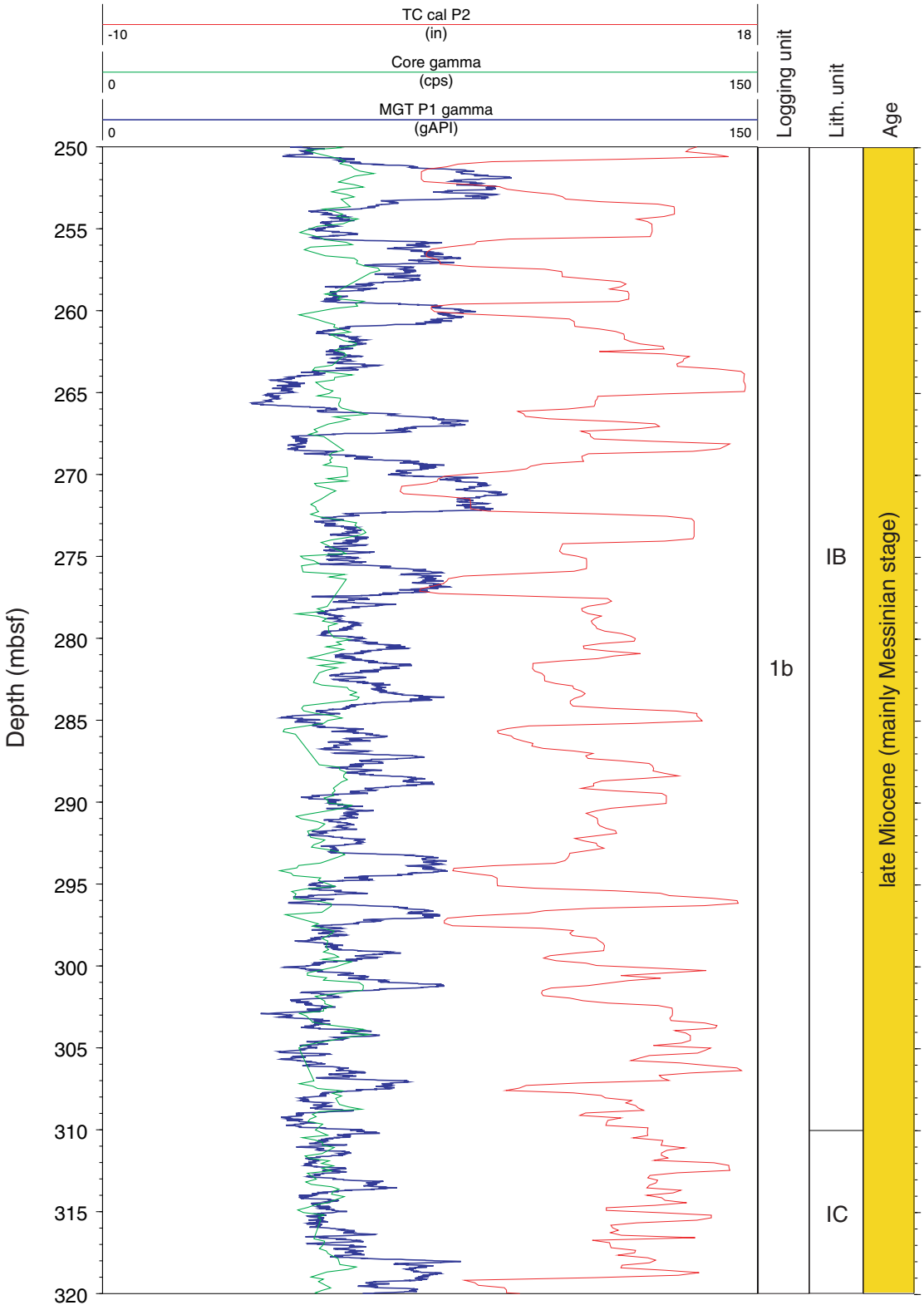

Figure F27. Triple combination (TC) logs and Formation MicroScanner (FMS) imagery through the chalk raft in the upper part of the debris flow of logging Unit 2 in Hole 1261B. Multi-Sensor Spectral Gamma Ray Tool, HSGR = HNGS standard (total) gamma ray, PEF = photoelectric effect.

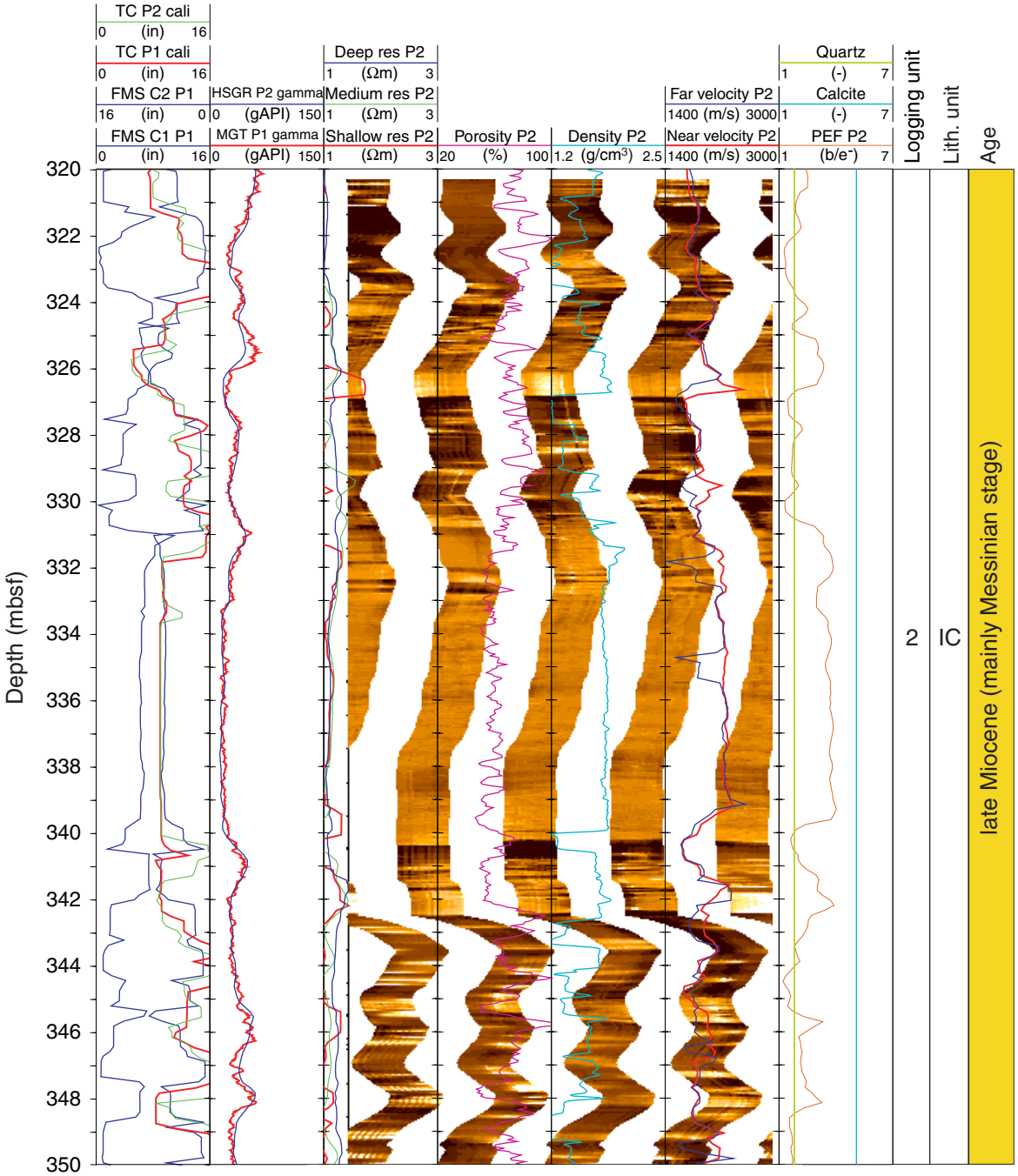

Figure F28. Stratigraphy of the black shale interval revealed by Formation MicroScanner (FMS) imagery and wireline-measured physical properties in logging Unit 3 in Hole 1261B. TC = triple combination, MGT = Multi-Sensor Spectral Gamma Ray Tool, HSGR = HNGS standard (total) gamma ray, PEF = photoelectric effect.

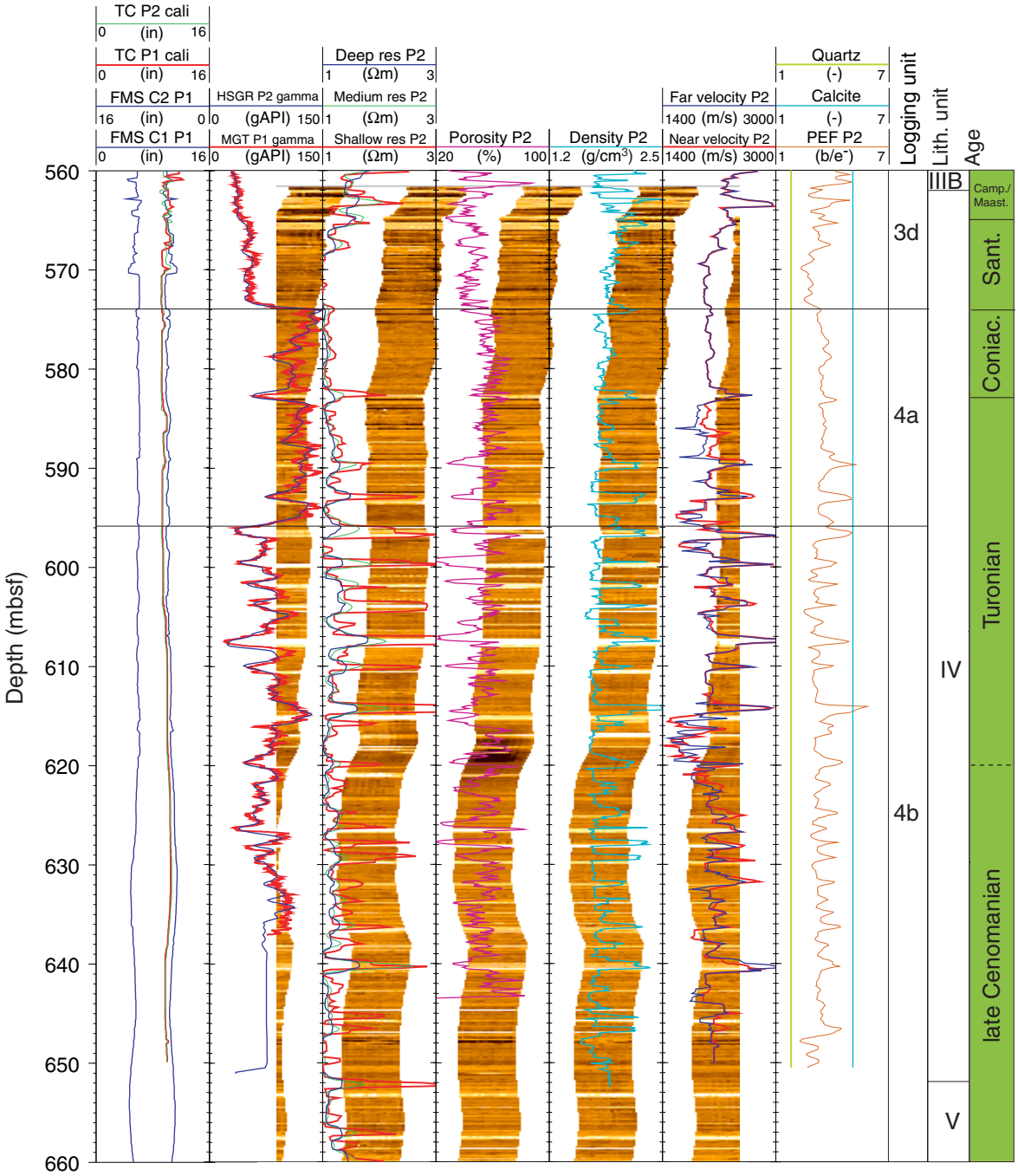

Figure F29. Comparison of core-measured total organic carbon (TOC) in Holes 1261A and 1261B and log-calculated TOC values through the black shale interval in Holes 1261B.

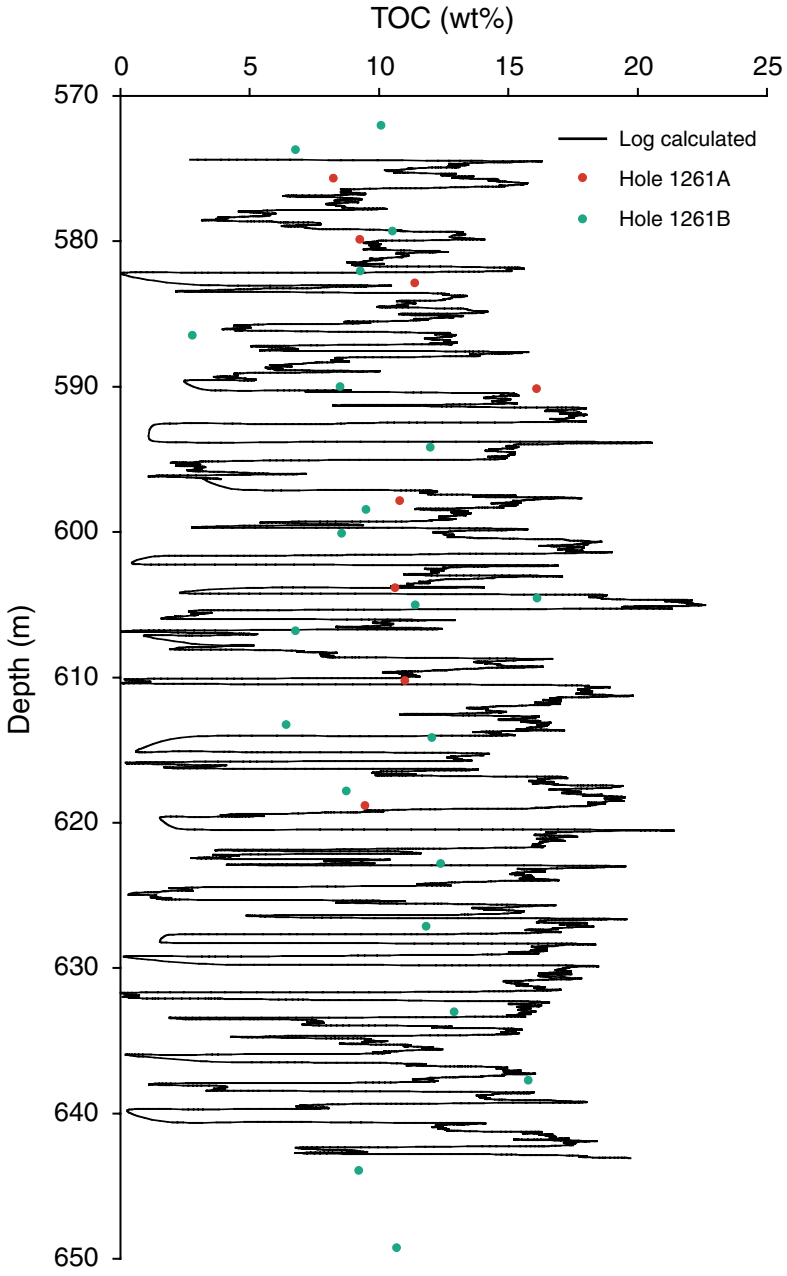

Figure F30. Formation density, velocity, impedance, and reflection coefficient series profiles obtained from downhole logging and core physical property measurements from Holes 1261A and 1261B.

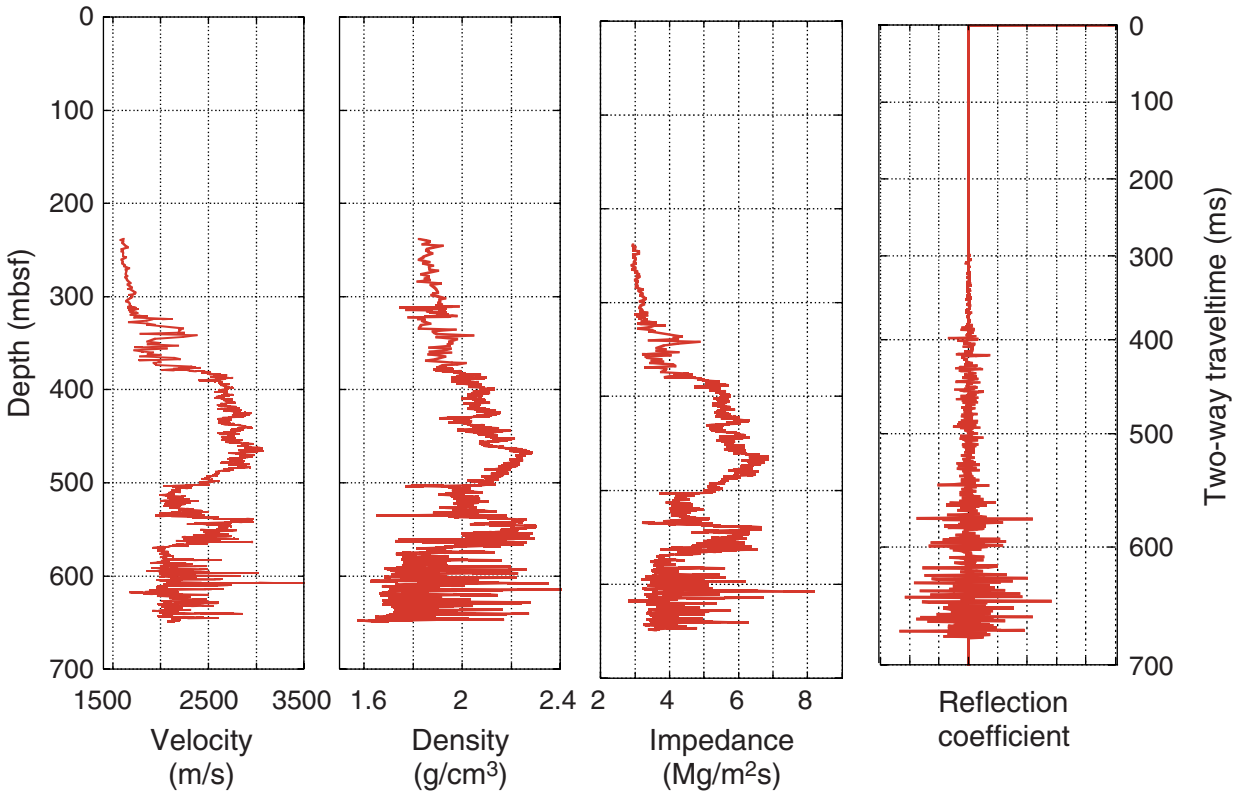

Figure F31. Part of seismic line M49-4-GeoB213 showing the key seismic stratigraphic reflectors, the calculated synthetic seismogram, and the associated impedance profile (derived from the density and velocity data) at Site 1261.

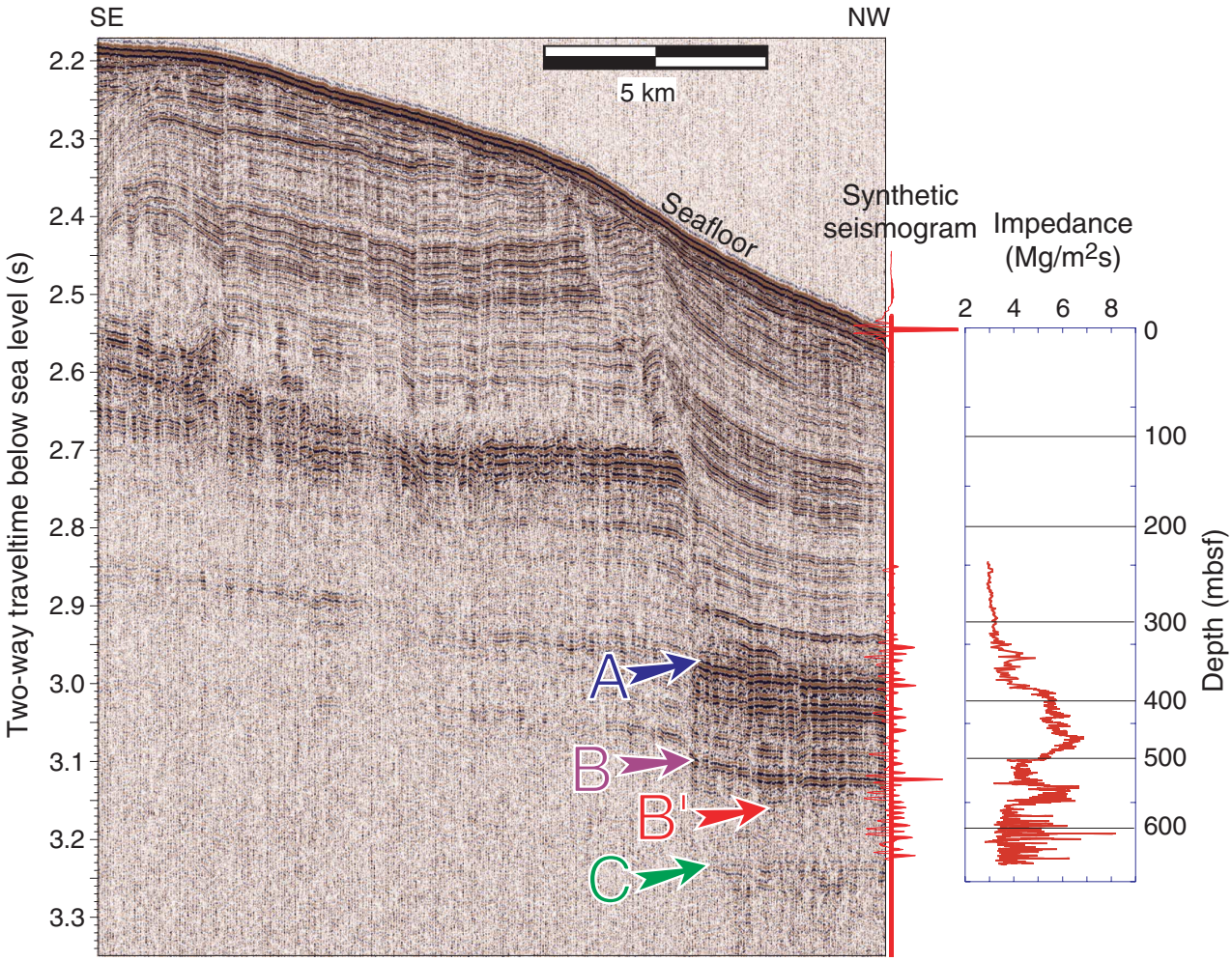

Table T1. Coring summary, Site 1261. (See table note. Continued on next page.)

Hole 1261A
Latitude: 9°2.9168′N
Longitude: 54°19.0384′W
Time on site: 152.80 (1547 hr, 16 Feb–0035 hr, 23 Feb 2003)
Time on hole: 67.88 (0147 hr, 16 Feb–1140 hr, 19 Feb 2003)
Seafloor (drill pipe measurement from rig floor, mbrf): 1911.1
Distance between rig floor and sea level (m): 11.4
Water depth (drill pipe measurement from sea level, m): 1899.7
Total depth (drill pipe measurement from rig floor, mbrf): 2580.6
Total penetration (meters below seafloor, mbsf): 669.5
Total length of cored section (m): 484.0
Total length of drilled intervals (m): 185.5
Total core recovered (m): 355.42
Core recovery (%): 73.4
Total number of cores: 51
Total number of drilled intervals: 4

Hole 1261B
Latitude: 9°2.9177′N
Longitude: 54°19.0491′W
Time on hole: 84.92 (1250 hr, 19 Feb–0035 hr, 23 Feb 2003)
Seafloor (drill pipe measurement from rig floor, mbrf): 1911.1
Distance between rig floor and sea level (m): 11.4
Water depth (drill pipe measurement from sea level, m): 1899.7
Total depth (drill pipe measurement from rig floor, mbrf): 2585.2
Total penetration (meters below seafloor, mbsf): 674.1
Total length of cored section (m): 148.8
Total length of drilled intervals (m): 525.3
Total core recovered (m): 92.49
Core recovery (%): 62.2
Total number of cores: 16
Total number of drilled intervals: 1

Core	Date (Feb 2003)	Local time (hr)	Depth (mbsf) Top	Depth (mbsf) Bottom	Length (m) Cored	Length (m) Recovered	Recovery (%)	Remarks
207-1261A-								
1R	16	2010	0.0	3.9	3.9	3.90	100.0	
2R	16	2100	3.9	13.2	9.3	0.71	7.6	
3R	16	2135	13.2	22.5	9.3	1.62	17.4	
			*****Drilled from 22.5 to 69.7 mbsf*****					
4R	17	0115	69.7	79.3	9.6	3.26	34.0	
			*****Drilled from 79.3 to 131.4 mbsf*****					
5R	17	0420	131.4	141.1	9.7	8.15	84.0	
			*****Drilled from 141.1 to 189.1 mbsf*****					
6R	17	0700	189.1	198.7	9.6	9.10	94.8	
			***** Drilled from 198.7 to 236.9 mbsf*****					
7R	17	0935	236.9	246.5	9.6	9.18	95.6	
8R	17	1030	246.5	256.2	9.7	9.27	95.6	
9R	17	1120	256.2	265.8	9.6	8.61	89.7	
10R	17	1210	265.8	275.4	9.6	8.28	86.3	
11R	17	1300	275.4	285.1	9.7	9.56	98.6	
12R	17	1340	285.1	294.7	9.6	8.16	85.0	
13R	17	1425	294.7	304.4	9.7	8.90	91.8	
14R	17	1505	304.4	314.0	9.6	9.11	94.9	
15R	17	1550	314.0	323.6	9.6	9.05	94.3	
16R	17	1625	323.6	333.3	9.7	8.01	82.6	
17R	17	1710	333.3	342.9	9.6	9.84	102.5	
18R	17	1800	342.9	352.5	9.6	8.85	92.2	
19R	17	1840	352.5	362.1	9.6	9.70	101.0	
20R	17	1915	362.1	371.8	9.7	9.59	98.9	
21R	17	2000	371.8	381.4	9.6	3.76	39.2	
22R	17	2040	381.4	391.1	9.7	3.70	38.1	
23R	17	2135	391.1	400.7	9.6	9.87	102.8	
24R	17	2225	400.7	410.3	9.6	6.46	67.3	
25R	17	2315	410.3	419.9	9.6	6.84	71.3	
26R	17	2355	419.9	429.5	9.6	5.99	62.4	
27R	18	0055	429.5	439.1	9.6	3.94	41.0	
28R	18	0236	439.1	448.7	9.6	9.89	103.0	
29R	18	0410	448.7	458.3	9.6	5.54	57.7	
30R	18	0525	458.3	467.6	9.3	2.86	30.8	

Table T1 (continued).

Core	Date (Feb 2003)	Local time (hr)	Depth (mbsf) Top	Depth (mbsf) Bottom	Length (m) Cored	Length (m) Recovered	Recovery (%)	Remarks
31R	18	0630	467.6	477.2	9.6	0.58	6.0	
32R	18	0755	477.2	486.8	9.6	9.99	104.1	
33R	18	0920	486.8	496.5	9.7	5.94	61.2	K/T recovered
34R	18	1040	496.5	506.1	9.6	5.82	60.6	
35R	18	1210	506.1	515.7	9.6	7.25	75.5	
36R	18	1320	515.7	525.3	9.6	8.71	90.7	
37R	18	1420	525.3	535.0	9.7	10.01	103.2	
38R	18	1530	535.0	544.6	9.6	0.05	0.5	
39R	18	1655	544.6	554.2	9.6	5.11	53.2	
40R	18	1825	554.2	563.8	9.6	8.00	83.3	
41R	18	1940	563.8	573.4	9.6	9.90	103.1	
42R	18	2050	573.4	583.0	9.6	9.69	100.9	
43R	18	2205	583.0	592.6	9.6	7.15	74.5	
44R	18	2320	592.6	602.2	9.6	7.94	82.7	
45R	19	0045	602.2	611.8	9.6	6.06	63.1	
46R	19	0220	611.8	621.4	9.6	7.41	77.2	
47R	19	0335	621.4	631.0	9.6	8.81	91.8	
48R	19	0450	631.0	640.6	9.6	8.97	93.4	
49R	19	0600	640.6	650.2	9.6	9.18	95.6	
50R	19	0735	650.2	659.8	9.6	4.69	48.9	
51R	19	0920	659.8	669.5	9.7	2.46	25.4	
				Cored totals:	484.0	355.42	73.4	
				Drilled total:	185.5			
				Total:	669.5			
207-1261B-								
			*****Drilled from 0.0 to 525.3 mbsf*****					
1R	20	1335	525.3	530.0	4.7	0.00	0.0	No recovery
2R	20	1425	530.0	539.6	9.6	4.29	44.7	
3R	20	1515	539.6	549.2	9.6	7.81	81.4	
4R	20	1620	549.2	558.8	9.6	7.77	80.9	
5R	20	1705	558.8	568.4	9.6	9.54	99.4	
6R	20	1750	568.4	578.0	9.6	9.43	98.2	
7R	20	1835	578.0	587.6	9.6	7.86	81.9	
8R	20	1935	587.6	597.2	9.6	3.82	39.8	
9R	20	2030	597.2	606.8	9.6	7.02	73.1	
10R	20	2115	606.8	616.4	9.6	4.59	47.8	
11R	20	2205	616.4	626.0	9.6	3.26	34.0	
12R	20	2255	626.0	635.6	9.6	9.45	98.4	
13R	20	2345	635.6	645.2	9.6	9.58	99.8	
14R	21	0040	645.2	654.8	9.6	5.27	54.9	
15R	21	0145	654.8	664.5	9.7	1.32	13.6	
16R	21	0520	664.5	674.1	9.6	1.48	15.4	
				Cored totals:	148.8	92.49	62.2	
				Drilled total:	525.3			
				Total:	674.1			

Note: K/T = Cretaceous/Tertiary.

Table T2. Lithostratigraphic units and subunits, Site 1261.

Unit/ subunit	Hole, core, section, interval (cm)	Depth (mbsf)	Thickness (mbsf)	Age	Lithology
	207-				
IA	1261A-1R-1, 0, through 4R-1, 0	0.00–69.70	69.70	Pleistocene–middle Pliocene	Nannofossil ooze
	*	—			
IB	1261A-4R-1, 0, through 14R-5, 15	69.70–310.55	240.85	middle Pliocene–late Miocene	Nannofossil clay
	*	—			
IC	1261A-14R-5, 15, through 20R-5, 117	310.55–369.27	58.72	late Miocene	Clayey nannofossil ooze
	*	—			
II	1261A-20R-5, 117 to 33R-4, 128	369.27–491.70	122.43	Eocene	Calcareous chalk with clay
	*	—			
IIIA	1261A-33R-4, 128, through 39R-1, 0	491.70–544.60	52.90	Paleocene	Nannofossil chalk with clay
	1261B-2R-1, 0, through 2R-3, 83	<530.00–533.83	>3.83		
IIIB	1261A-39R-1, 0, through 41R-1, 33	544.60–564.13	19.53	Maastrichtian–Campanian	Clayey nannofossil chalk
	1261B-2R-3, 83, through 5R-4, 109	533.83–563.30	29.47		
IV	1261A-41R-1, 33, through 50R-3, 32	564.13–653.52	89.39	Santonian–late Cenomanian	Calcareous claystone with organic matter; nannofossil chalk with organic matter
	1261B-5R-4, 109, through 14R-4, 51	563.30–650.21	86.91		
V	1261A-50R-3-32, through 51R-2, 114	653.52–662.26	8.74	Cenomanian–Albian	Quartz sandstone
	1261B-14R-4, 51, through 16R-1, 148	650.21–665.98	15.77		

Note: * = not recovered from Hole 1261B. — = not assigned.

Table T3. Datum levels for calcareous nannofossils, Hole 1261A.

Core, section, interval (cm)	Depth (mbsf) Top	Depth (mbsf) Bottom	Depth (mcd) Top	Depth (mcd) Bottom	Datum	Species	Zone	Age	Age (My)
207-1261A-									
1R-CC, 12–17	3.85	4.61	3.85	4.61	B	*Emiliania huxleyi*	NN21	late Pleistocene	0.3
2R-CC, 66–71	3.85	4.61	3.85	4.61	T	*Pseudoemiliania lacunosa*	NN19	Pleistocene	0.4
3R-CC, 18–23	4.61	14.77	4.61	14.77	T	*Sphenolithus* sp.	NN16	early Pliocene	3.7
5R-CC, 8–13	72.91	139.50	72.91	139.50	T	*Reticulofenestra pseudoumbilica*		early Pliocene	3.8
7R-CC, 25–30	198.12	246.03	198.12	246.03	T	*Discoaster quinqueramus*	NN11	late Miocene	5.5
9R-CC, 21–28	264.74	274.03	264.74	274.03	B	*Nicklithus amplificus*	NN11 (CN9bB)	late Miocene	6.0
20R-5, 118–118	369.28	369.28	369.28	369.28	B	*Discoaster berggrenii*	NN11	late Miocene	8.3
20R-CC, 11–16	362.15	371.64	362.15	371.64	T	*Chiasmolithus grandis*	NP17	middle Eocene	37.1
20R-CC, 11–16	371.64	375.50	371.64	375.50	B	*Dictyococcites bisectus*	NP17	middle Eocene	38.5
21R-CC, 23–29	371.64	375.50	371.64	375.50	T	*Chiasmolithus solitus*	NP16	middle Eocene	40.4
27R-CC, 0–6	425.53	433.38	425.53	433.38	T	*Chiasmolithus gigas*	NP15 (= CP13b)	middle Eocene	44.0
27R-CC, 0–6	433.38	448.94	433.38	448.94	B	*Chiasmolithus gigas*	NP15 (= CP13b)	middle Eocene	46.1
33R-4, 128–128	491.70	491.70	491.70	491.70	X	*Zygrhablithus bijugatus*/ fasciculiths	NP9	Paleocene/Eocene boundary	55.0
34R-CC, 0–5	502.29	513.30	502.29	513.30	B	*Discoaster multiradiatus*	NP9	late Paleocene	56.2
37R-CC, 0–3	535.02	535.31	535.02	535.31	B	*Chiasmolithus danicus*	NP3	early Paleocene	63.8
37R-CC, 24–29	535.26	535.31	535.26	535.31	K/T disconformity	Approximate K/T boundary		Cretaceous/Tertiary boundary	65.0
38R-CC, 0–5	535.00	549.58	535.00	549.58	B	*Micula murus*	CC26/26	late Maastrichtian	66.2
40R-6, 55–57	549.58	562.21	549.58	562.27	T	*Uniplanarius trifidum*	CC23	late Campanian	76.0
41R-CC, 21–22	573.69	583.04	574.60	583.95	B	*Micula decussata*	CC14	late Coniacian	87.2
43R-CC, 12–17	590.10	600.49	591.38	601.90	B	*Marthasterites furcatus*	CC13	early Coniacian	89.3
44R-6, 65–70	600.49	608.11	601.90	608.08	B	*Eiffellithus eximius*	CC12	late Turonian	91.0
45R-CC, 5–7	608.11	619.06	608.08	616.96	B	*Eprolithus eptapetalus*	CC11	early Turonian	93.2
48R-CC, 11–15	630.17	639.93	628.07	636.99	T	*Axopodorhabdus albianus*	CC10	late Cenomanian	94.0
50R-3, 0–2	653.20	653.22	649.41	649.43	B	*Eiffellithus turriseiffelii*	NC10a	late Albian	101.7

Note: B = bottom, T = top, X = crossover in relative abundance, K/T = Cretaceous/Tertiary.

Table T4. Distribution of planktonic foraminifers, Hole 1261A. (This table is available in an **oversized format.**)

Table T5. Datum levels for planktonic foraminifers, Site 1261.

Core, section, interval (cm)	Depth (mbsf)		Depth (mcd)		Datum	Species	Zone	Age	Age (Ma)
	Top	Bottom	Top	Bottom					
207-1261A-									
3R-CC, 18–23	14.77	72.91	14.77	72.91	B	*Globorotalia truncatulinoides**	PL1	late Pliocene and Pleistocene	1.9
5R-CC, 8–13	72.91	139.50	72.91	139.50	T	*Globorotalia margaritae**	PL2	early Pliocene	3.6
20R-5, 116–119	369.26	369.30	369.26	369.30	B	*Globorotalia plesiotumida**	M13b	late Miocene	8.6
20R-5, 120–122	369.26	369.30	369.26	369.30	T	*Acarinina* and *Morozovella* spp.*	P14	middle Eocene	37.5–38.5
21R-2, 84–86	371.64	374.12	371.64	374.12	T	*Orbulinoides beckmanni*	P13	middle Eocene	40.1
31R-1, 56–58	468.16	487.14	468.16	487.14	B	*Morozovella aragonensis**	P7	early Eocene	52.3
32R-CC, 19–24	468.16	487.14	468.16	487.14	T	*Morozovella velascoensis* group	P5	late Paleocene	54.7
37R-7, 52–55	534.82	535.02	534.82	535.02	B	*Praemurica uncinata*	P2	early Paleocene	61.2
38R-CC, 0–5	535.00	535.26	535.00	535.26	T	*Abathomphalus mayaroensis*	KS31	Maastrichtian	65.0
39R-CC, 16–22	549.58	562.21	549.58	562.21	B	*Globotruncana aegyptiaca**	KS29–31	late Campanian–Maastrichtian	73.8
42R-3, 106–108	577.33	579.32	578.99	580.98	B	*Contusotruncana fornicata*	KS24–23	Santonian	88.0
48R-CC, 11–15	630.17	639.93	628.07	636.99	T	*Rotalipora* spp.	KS19	Cenomanian	94.0
207-1261B-									
2R-3, 78–79	533.78	534.24	538.38	538.84	B	*Praemurica uncinata*	P2 and KS31	early Paleocene	61.2
2R-3, 124–129	533.78	534.24	538.38	538.84	T	*Abathomphalus mayaroensis*	KS31	Maastrichtian	65.0
6R-7, 58–63	577.78	585.63	579.04	586.23	B	*Contusotruncana fornicata*	KS24	Santonian	88.0
11R-CC, 14–19	619.61	635.41	612.62	634.03	B	*Whiteinella* spp.	KS22–20	Turonian	95.4

Notes: Top and bottom depth values refer to the range of possible depth in the core within which the datum is believed to fall. B = bottom, T = top. * = datums that probably reflect incomplete ranges of the foraminifer marker species.

Table T6. Datum levels, ages, and preservation of samples for calcareous nannofossils, Site 1261.

Core, section, interval (cm)	Depth (mbsf)	Zone	Age	Preservation	Group abundance
207-1261A-					
1R-CC, 12–17	3.85	NN21	Quaternary	G	C
2R-1, 66–71	4.56	NN19	Quaternary	G	C
3R-CC, 18–23	14.77	NN16	Pliocene	G	C
4R-CC, 15–20	72.91	NN16	Pliocene	G	C
5R-CC, 8–13	139.50	NN13	Pliocene	G	C
6R-CC, 0–8	198.12	NN13	Pliocene	G	C
7R-CC, 25–30	246.03	NN11	late Miocene	G	C
8R-CC, 0–5	255.72	NN11	late Miocene	G	C
9R-CC, 21–28	264.74	NN11	late Miocene	G	C
10R-CC, 14–19	274.03	NN11	late Miocene	G	C
11R-CC, 0–5	284.91	NN11	late Miocene	G	C
12R-CC, 12–19	293.19	NN11	late Miocene	G	C
13R-6, 135–140	303.55	NN11	late Miocene	G	C
14R-7, 41–47	313.31	NN11	late Miocene	G	C
15R-CC, 0–5	323.00	NN6	middle Miocene	M	C
16R-6, 48–51	331.58	NN4	middle Miocene	M	C
17R-6, 0–1	340.80				
17R-CC, 0–5	343.09	NN11	late Miocene	G	C
18R-CC, 5–9	351.65	NN11	late Miocene	G	C
19R-CC, 9–14	362.15	NN9	late Miocene	G	C
20R-CC, 11–16	371.64	NP17	middle Eocene	P	F
21R-CC, 23–29	375.50	NP17	middle Eocene	P	F
22R-3, 65–70	385.05	NP16	middle Eocene	P	F
23R-CC, 21–25	400.93	NP16	middle Eocene	P	R
24R-CC, 4–9	406.97	NP16	middle Eocene	P	F
25R-5, 95–100	417.09	NP16	middle Eocene	P	F
26R-CC, 0–5	425.53	NP16	middle Eocene	P	F
27R-CC, 0–6	433.38	NP15	middle Eocene	M	C
28R-CC, 17–22	448.94	NP15	middle Eocene	P	R
29R-CC, 9–14	454.19	NP13	early Eocene	P	R
30R-2, 145–150	461.11	NP13	early Eocene	P	R
31R-1, 56–58	468.16	NP13	early Eocene	P	R
32R-CC, 19–24	487.14	NP9	early Eocene	P	F
33R-CC, 0–5	492.69	NP9	Paleocene	M	C
34R-CC, 0–5	502.29	NP9	Paleocene	M	C
35R-CC, 0–5	513.30				
36R-6, 120–121	524.44				
37R-CC, 24–29	535.26	NP2	Paleocene	M	C
38R-CC, 0–5	535.00	CC26	Maastrichtian	M	C
39R-CC, 16–22	549.58	CC25	Maastrichtian	M	C
40R-6, 55–60	562.21	CC23	Campanian	M	C
41R-CC, 8–12	573.56	CC14	Coniacian	M	C
42R-CC, 10–15	583.04	CC13	Coniacian	M	F
43R-CC, 12–17	590.10	CC12	Turonian	M	R
44R-6, 65–70	600.49	CC12	Turonian	G	C
45R-3, 138–152	606.36	CC11	Turonian	M	C
46R-CC, 0–3	619.06	CC11	Turonian	G	C
47R-CC, 14–18	630.17	CC10	Cenomanian	G	C
48R-CC, 11–15	639.93	CC10	Cenomanian	G	C
49R-CC, 0–2	649.59	CC10	Cenomanian	P	C
50R-3, 0–2	653.20	CC10	Cenomanian	P	C
207-1261B-					
2R-3, 124–129	534.24	NP2	early Paleocene	M	F
3R-6, 79–81	547.39	NP2	early Paleocene	M	F
4R-CC, 11–16	556.92	CC23	Campanian	G	C
5R-8, 58–63	568.29	CC14	Coniacian		
6R-7, 58–63	577.78	CC13	Coniacian		
7R-CC, 0–3	585.63	CC12	Turonian	M	R
8R-3, 62–65	591.22	CC12	Turonian		
9R-CC, 12–17	603.95	CC11	Turonian	M	R
10R-CC, 10–15	611.34	CC11	Turonian	M	R
11R-CC, 14–19	619.61			P	R
12R-CC, 17–21	635.41			M	R
14R-2, 0–2	646.70	CC10	Cenomanian	P	R
14R-3, 0–2	648.20	CC10	Cenomanian	M	F
15R-1, 0–3	654.80				

Notes: Preservation: G = good, M = moderate, P = poor. Abundance: C = common, F = few, R = rare.

Table T7. Distribution of planktonic foraminifers, Hole 1261B.

Core, section, interval (cm)	Depth (mbsf)	Zone	Age	Preservation	Group abundance	*Clavihedbergella simplex*	*Hedbergella delrioensis*	*Globigerinelloides caseyi*	*Heterohelix globulosa*	*Heterohelix moremani*	*Globigerinelloides* sp. 1	*Whiteinella baltica*	*Whiteinella inornata*	*Hedbergella planispira*	*Archaeoglobigerina blowi*	*Archaeoglobigerina bosquensis*	*Contusotruncana fornicata*	*Archaeoglobigerina cretacea*	*Dicarinella concavata*	*Marginotruncana pseudolinneiana*	*Marginotruncana sinuosa*	*Whiteinella archaeocretacea*	*Globotruncana aegyptiaca*	*Globotruncana arca*	*Globotruncana linneiana*	*Rugoglobigerina rugosa*	*Globotruncana esnehensis*	*Pseudoguembelina costulata*	*Globotruncana insignis*	*Globotruncana ventricosa*	*Globotruncanita stuarti*	*Pseudotextularia elegans*	*Rugoglobigerina rotundata*	*Abathomphalus mayaroensis*	*Gansserina gansseri*	*Heterohelix labellosa*	*Parasubbotina pseudobulloides*	*Praemurica inconstans*	*Praemurica uncinata*	*Pseudotextularia deformis*	*Racemiguembelina fructicosa*	*Parasubbotina varianta*	*Morozovella praeangulata*	*Subbotina triloculinoides*
207-1261B-																																											
2R-1, 1–2	530.01	P2	early Paleocene	P	F																																				X	X	X
2R-1, 14–15	530.14	P2	early Paleocene	P	F																																		X	X		X	X	X
2R-1, 125–126	531.25	P2	early Paleocene	P	F																																			X			X	X	X
2R-2, 0–2	531.50	P2	early Paleocene	P	C																																		X	X	X		X	X	
2R-2, 109–110	532.59	P2	early Paleocene	P	A																																		X	X	X		X		
2R-3, 0–2	533.00	P2	early Paleocene	P	A																																		X	X	X				
2R-3, 51–52	533.51	P2	early Paleocene	P	C																																		X	X	X				
2R-3, 78–79	533.78	P2 and KS31	early Paleocene	P	C																					X	X	X		X			X	X	X	X	X	X	X	X				
2R-3, 124–129	534.24	KS31	Maastrichtian	P	C				X														X		X					X		X	X	X									
3R-6, 79–81	547.39	Undefined	late Campanian–Maastrichtian	P	C				X																X				X	X	X												
4R-1, 140–141	550.60	KS29–31	late Campanian–Maastrichtian	P	C				X														X		X	X	X		X														
4R-2, 77–81	551.47	KS29	late Campanian	P	C												X						X	X		X	X	X														
4R-CC, 11–16	556.92	KS29	late Campanian	P	C				X														X	X	X	X																
5R-8, 58–63	568.29	KS23–KS24	Santonian	G	C				X						X		X	X	X	X	X	X																				
6R-7, 58–63	577.78	KS23–KS24	Santonian	M	F				X						X	X	X																									
7R-CC, 0–3	585.63	Undefined	No age assignment	P	R				X																																		
8R-3, 62–65	591.22	Undefined	No age assignment	P	R				X					X																													
9R-CC, 12–17	603.95	Undefined	Turonian?	P	R				X			X																															
10R-CC, 10–15	611.34	KS22–KS20	Turonian	P	F	X	X		X			X																															
11R-CC, 14–19	619.61	KS22–KS20	Turonian	P	R							X	X																														
12R-CC, 17–21	635.41			B	B																																					
14R-2, 0–2	646.70	Undefined	No age assignment	P	F		X	X	X	X	X																															
14R-3, 0–2	648.20	Undefined	No age assignment	P	F	X	X																																			
15R-1, 0–3	654.80			B	B																																					
16R-1, 98–99	665.48			B	B																																					

Notes: Preservation: G = good, M = moderate, P = poor, B = barren. Abundance: A = abundant, C = common, F = few, R = rare, B = barren.

Table T8. Characteristic directions of minicores, Holes 1261A and 1261B. (See table notes. Continued on next page.)

Core, section, interval (cm)	PMAG code	Depth (mcd)	Polarity Label	Polarity Code	Chron/ subchron	Declination (°)	Inclination (°)	Intensity (mA/m)	MAD (°)	N	Temperature steps used in least square analysis (°C) 1	2	3	4	5	6	7	8	9	10	11	12	13
207-1261A-																							
20R-5, 132	205.132	369.42	N?	1		327.5	–4.0	4.48E–03	9.6	4	240	240	270	270	Org	Tied							
20R-7, 43	207.043	371.43	NP	3	C18n?	65.0	–18.3	4.90E–03	4.3	5	150	150	200	200	250	Org	Tied						
21R-1, 17	211.017	371.97	RP	–3		294.5	–0.4	1.30E–02	4.7	3	300	350	400	Org	Tied								
21R-1, 68	211.068	372.48	N	4		323.8	1.4	1.31E–02	3.9	6	150	200	250	300	350	400	Org	Tied					
21R-3, 14	213.014	374.72	RP	–3		144.4	16.2	1.08E–02	2.3	3	250	300	350	Org	Tied								
21R-3, 30	213.030	374.88	N	4	C18n?	9.3	14.1	1.36E–02	16.2	7	200	240	270	300	330	360	400	Org	Tied				
23R-1, 27	231.027	391.37	R?	–1		76.6	–16.0	3.65E–03	10.4	6	150	150	200	200	240	240	Org	Tied					
23R-3, 37	233.037	394.47	R	–4	C19r	246.3	4.9	4.96E–03	4.8	4	300	350	400	400	Org	Tied							
23R-5, 38	235.038	397.48	R	–4		55.4	1.3	1.16E–02	2.2	4	200	250	300	350	Org	Tied							
23R-7, 35	237.035	400.45	R	–4		359.9	6.5	2.91E–02	2.8	7	200	240	270	300	330	360	400	Org	Tied				
24R-1, 24	241.024	400.94	R	–4		253.2	4.7	2.58E–02	2.7	6	150	200	250	300	350	400	Org	Tied					
24R-3, 31	243.031	403.71	NP	3	C20n	315.3	–5.5	1.58E–02	5.9	7	150	200	250	250	300	350	400	Org	Tied				
24R-5, 32	245.032	406.52	N	4		170.8	–6.7	2.99E–02	2.0	7	200	240	270	300	330	360	400	Org	Tied				
25R-1, 51	251.051	410.81	N	4		155.4	0.3	1.91E–02	3.1	6	150	200	250	300	350	400	Org	Tied					
25R-3, 49	253.049	413.63	N	4		306.4	–0.1	2.19E–02	2.1	6	150	200	250	300	350	400	Org	Tied					
25R-5, 38	255.038	416.52	N	4		286.7	–0.4	2.03E–02	2.5	7	200	240	270	300	330	360	400	Org	Tied				
26R-1, 23	261.023	420.13	RP	–3	C20r	134.2	–19.8	6.25E–03	4.8	3	350	400	400	Org	Tied								
26R-3, 7	263.007	422.57	R	–4		286.0	–1.4	1.84E–02	3.1	5	200	250	300	350	400	Org	Tied						
26R-5, 40	265.040	425.40	RP	–3		242.8	–9.7	1.62E–02	3.4	6	240	270	300	330	360	400	Org	Tied					
27R-1, 52	271.052	430.02	R	–4		105.4	1.9	2.54E–02	0.9	4	200	250	300	350	Org	Tied							
27R-3, 58	273.058	433.08	RP	–3		57.8	–2.8	1.02E–02	4.7	4	250	300	350	400	Org	Tied							
28R-1, 53	281.053	439.63	R	–4		219.3	4.4	2.00E–02	2.3	5	240	270	300	330	360	Org	Tied						
28R-3, 48	283.048	442.08	RP	–3		142.2	–5.1	1.22E–02	7.1	4	250	300	350	400	Org	Tied							
28R-5, 36	285.036	444.56	RPP	–2		281.9	–15.0	4.85E–03	5.1	4	250	250	300	300	Org	Tied							
28R-7, 14	287.014	447.34	NP	3	C21n?	56.0	–8.5	1.17E–02	1.3	2	360	400	Org	Tied									
29R-1, 23	291.023	448.93	NP	3		104.3	3.5	1.95E–02	1.2	2	350	400	Org	Tied									
29R-3, 10	293.010	451.80	N	4		134.7	6.5	8.55E–03	3.5	5	200	250	300	350	400	Org	Tied						
30R-1, 54	301.054	458.84	RP	–3	C21r?	268.4	4.8	2.29E–02	2.7	5	240	270	300	330	360	Org	Tied						
30R-2, 33	302.033	459.99	RPP	–2		149.7	–43.1	1.25E–02	0.0	1	400	Org	Tied										
					Hiatus?																		
31R-1, 51	311.051	468.11	N	4	C23n?	26.8	–8.3	2.12E–01	1.2	3	330	360	400	Org	Tied								
					Hiatus																		
32R-1, 20	321.020	477.40	RPP	–2	C24r	147.3	19.2	5.76E–03	0.4	2	300	300	Org	Tied									
32R-2, 8	322.008	478.78	RP	–3		123.7	–1.9	8.59E–03	7.5	3	200	250	300	Org	Tied								
32R-5, 21	325.021	483.41	RPP	–2		133.0	4.0	4.93E–03	2.2	4	300	300	330	330	Org	Tied							
32R-7, 4	327.004	486.24	RPP	–2		114.6	–7.2	5.74E–03	7.1	4	250	250	300	300	Org	Tied							
33R-1, 4	331.004	486.84	RP	–3		277.5	5.7	7.47E–03	7.4	3	250	300	350	Org	Tied								
34R-1, 58	341.058	497.08	RP	–3		181.5	0.5	4.24E–03	10.8	4	250	250	300	300	Org	Tied							
34R-3, 21	343.021	499.73	R	–4		22.2	4.2	9.32E–03	5.6	7	200	240	270	300	330	330	400	Org	Tied				
					Gap in coverage																		
35R-1, 95	351.095	507.05	INT	0		51.3	59.3	1.38E–02	4.9	2	350	400	Org	Tied									
35R-3, 88	353.088	509.98	RPP	–2		274.4	37.4	4.26E–03	1.7	2	300	300	Org	Tied									
35R-5, 26	355.026	512.36	RP	–3		253.0	0.9	4.59E–03	19.0	4	200	250	300	300	Org	Tied							
35R-6, 5	356.005	513.30	NPP	2	C26n	263.5	31.5	3.53E–03	3.3	2	150	150	Org	Tied									
36R-1, 25	361.025	515.95	N	4		225.2	10.8	1.10E–01	2.4	3	330	360	400	Org	Tied								
36R-3, 7	363.007	518.77	RPP	–2	C26r	218.2	6.1	4.32E–03	0.0	2	300	300	Org	Tied									
37R-1, 35	371.035	525.65	RPP	–2		163.0	14.4	4.52E–03	2.0	2	300	300	Org	Tied									

Table T8 (continued).

Core, section, interval (cm)	PMAG code	Depth (mcd)	Polarity			Chron/ subchron	Declination (°)	Inclination (°)	Intensity (mA/m)	MAD (°)	*N*	Temperature steps used in least square analysis (°C)												
			Label	Code								1	2	3	4	5	6	7	8	9	10	11	12	13
37R-3, 5	373.005	528.35	RP	–3			101.2	–2.5	1.31E–02	4.9	5	240	270	300	330	360	Org	Tied						
37R-5, 12	375.012	531.42	NP	3		C27n	301.7	9.2	4.17E–03	7.1	3	250	300	300	Org	Tied								
37R-7, 49	377.049	534.79	RP	–3		C27r?	187.3	8.8	5.80E–03	8.8	11	200	240	240	270	270	300	300	330	330	360	360	Org	Tied
39R-1, 42	391.042	545.02	NP	3		C31n?	332.3	23.6	5.41E–03	1.3	3	300	300	300	Org	Tied								
39R-3, 18	393.018	547.78	N?	1		C31r?	167.8	17.9	6.93E–03	6.4	2	150	200	Org	Tied									
40R-1, 32	401.032	554.52	INT	0			19.1	54.3	4.27E–03	5.9	4	200	200	250	250	Org	Tied							
40R-3, 35	403.035	557.51	INT	0			57.3	64.5	4.27E–03	3.7	3	250	250	300	Org	Tied								
40R-5, 31	405.031	560.47	NPP	2		C32n?	352.7	51.0	6.00E–03	2.2	4	270	270	300	300	Org	Tied							
207-1261B-																								
2R-1, 25	21.025	534.85	NP	3		?	238.0	36.1	6.51E–03	5.6	6	150	200	250	250	300	300	Org	Tied					
2R-3, 72	23.072	538.32	RPP	–2		C29r	183.7	11.9	7.49E–03	9.3	2	250	300	Org	Tied									
2R-3, 117	23.117	538.77	RPP	–2			311.8	57.2	2.41E–03	4.6	2	250	250	Org	Tied									
3R-1, 79	31.079	541.87	N?	1			334.9	51.3	2.25E–03	0.0	1	200	Org	Tied										
3R-3, 58	33.058	544.66	NP	3		C31n?	233.0	47.7	4.08E–03	4.6	5	150	200	200	250	250	Org	Tied						
3R-5, 66	35.066	547.74	RPP	–2		C31r	35.6	64.7	2.83E–03	11.3	4	200	200	250	250	Org	Tied							
4R-1, 59	41.059	550.83	RPP	–2			313.5	64.4	5.47E–03	7.7	4	200	200	240	240	Org	Tied							
4R-3, 62	43.062	553.86	RP	–3			283.3	24.2	4.88E–03	6.5	6	200	200	250	250	300	300	Org	Tied					

Notes: PMAG = paleomagnetism, MAD = maximum angular deviation, R = reversed polarity, N = normal polarity. RP and NP = less precise reversed and normal polarity assignments, respectively. RPP and NPP = sample did not achieve adequate cleaning during demagnetization but polarity was obviously reversed or normal, respectively. Orig. = origin. Black = normal polarity, white = reversed polarity, gray = intermediate or questionable polarity, yellow = gap in coverage or hiatus. Examples of interpretation of progressive demagnetization plots and methods of computation of the characteristic directions are given in **"Paleomagnetism,"** p. 16, in the "Explanatory Notes" chapter.

Table T9. Composite depths, Site 1261.

Core	Depth (mbsf)	Offset (m)	Depth (mcd)	Depth shifted
207-1261A-				
1R	0.0	0.00	0.00	N
2R	3.9	0.00	3.90	N
3R	13.2	0.00	13.20	N
4R	69.7	0.00	69.70	N
5R	131.4	0.00	131.40	N
6R	189.1	0.00	189.10	N
7R	236.9	0.00	236.90	N
8R	246.5	0.00	246.50	N
9R	256.2	0.00	256.20	N
10R	265.8	0.00	265.80	N
11R	275.4	0.00	275.40	N
12R	285.1	0.00	285.10	N
13R	294.7	0.00	294.70	N
14R	304.4	0.00	304.40	N
15R	314.0	0.00	314.00	N
16R	323.6	0.00	323.60	N
17R	333.3	0.00	333.30	N
18R	342.9	0.00	342.90	N
19R	352.5	0.00	352.50	N
20R	362.1	0.00	362.10	N
21R	371.8	0.00	371.80	N
22R	381.4	0.00	381.40	N
23R	391.1	0.00	391.10	N
24R	400.7	0.00	400.70	N
25R	410.3	0.00	410.30	N
26R	419.9	0.00	419.90	N
27R	429.5	0.00	429.50	N
28R	439.1	0.00	439.10	N
29R	448.7	0.00	448.70	N
30R	458.3	0.00	458.30	N
31R	467.6	0.00	467.60	N
32R	477.2	0.00	477.20	N
33R	486.8	0.00	486.80	N
34R	496.5	0.00	496.50	N
35R	506.1	0.00	506.10	N
36R	515.7	0.00	515.70	N
37R	525.3	0.00	525.30	N
38R	535.0	0.00	535.00	N
39R	544.6	0.00	544.60	N
40R	554.2	0.00	554.20	N
41R	563.8	0.91	564.71	Y
42R	573.4	1.66	575.06	Y
43R	583.0	1.28	584.28	Y
44R	592.6	1.41	594.01	N
45R	602.2	–0.03	602.17	Y
46R	611.8	–2.10	609.70	Y
47R	621.4	–2.10	619.30	N
48R	631.0	–2.94	628.06	Y
49R	640.6	–3.33	637.27	Y
50R	650.2	–3.79	646.41	Y
51R	659.8	–3.79	656.01	N
207-1261B-				
1R	525.3	0.00	525.30	N
2R	530.0	4.60	534.60	Y
3R	539.6	1.48	541.08	Y
4R	549.2	1.04	550.24	Y
5R	558.8	0.63	559.43	Y
6R	568.4	1.26	569.66	Y
7R	578.0	0.60	578.60	Y
8R	587.6	–0.19	587.41	Y
9R	597.2	0.60	597.80	Y
10R	606.8	–2.18	604.62	Y
11R	616.4	–6.99	609.41	Y
12R	626.0	–1.38	624.62	Y
13R	635.6	–1.24	634.36	Y
14R	645.2	–0.75	644.45	Y
15R	654.8	–0.75	654.05	N
16R	664.5	–0.75	663.75	N

Note: N = no, Y = yes.

Table T10. Splice tie points, Site 1261.

Hole, core, section, interval (cm)	Depth (mbsf)	Depth (mcd)		Hole, core, section, interval (cm)	Depth (mbsf)	Depth (mcd)
207-				207-		
1261B-4R-6, 5	556.25	557.29	Tie to	1261A-40R-3, 12.5	557.29	557.29
1261A-40R-6, 17.5	561.84	561.84	Tie to	1261B-5R-3, 52.5	561.21	561.84
1261B-5R-6, 85	566.06	566.69	Tie to	1261A-41R-2, 47.5	565.78	566.69
1261A-41R-6, 52.5	571.83	572.74	Tie to	1261B-6R-3, 7.5	571.48	572.74
1261B-6R-5, 90	575.30	576.56	Tie to	1261A-42R-1, 150	574.90	576.56
1261A-42R-6, 112.5	581.90	583.56	Tie to	1261B-7R-4, 45	582.96	583.56
1261B-7R-5, 82.5	584.81	585.41	Tie to	1261A-43R-1, 112.5	584.13	585.41
1261A-43R-5, 107.5	589.93	591.21	Append to	1261A-44R-1, 0	592.60	594.01
1261A-44R-4, 120	598.04	599.45	Tie to	1261B-9R-2, 15	598.85	599.45
1261B-9R-4, 75	602.40	603.00	Tie to	1261A-45R-1, 82.5	603.03	603.00
1261A-45R-4, 90	607.40	607.37	Tie to	1261B-10R-2, 125	609.55	607.37
1261B-10R-3, 140	611.20	609.02	Append to	1261B-11R-1, 0	616.40	609.41
1261B-11R-2, 7.5	617.98	610.99	Tie to	1261A-46R-1, 128.5	613.09	610.99
1261A-46R-5, 135	618.99	616.89	Append to	1261A-47R-1, 0	621.40	619.30
1261A-47R-6, 67.5	629.35	627.25	Tie to	1261B-12R-2, 117.5	628.63	627.25
1261B-12R-3, 112.5	630.08	628.70	Tie to	1261A-48R-1, 63.5	631.64	628.70
1261A-48R-6, 60	639.05	636.11	Tie to	1261B-13R-2, 22.5	637.35	636.11
1261B-13R-3, 52.5	639.09	637.85	Tie to	1261A-49R-1, 57	641.18	637.85
1261A-49R-6, 30	648.38	645.05	Tie to	1261B-14R-1, 60	645.80	645.05
1261B-14R-2, 112.5	647.83	647.08	Tie to	1261A-50R-1, 66	650.87	647.08
1261A-50R-3, 140	654.60	650.81				

Table T11. Biostratigraphic datums used to calculate sedimentation rates, Hole 1261A.

Core, section, interval (cm)	Depth (mbsf) Minimum	Depth (mbsf) Maximum	Datum type	Taxon	Nannofossil zone	Foraminifer zone	Age (Ma)	Epoch
207-1261A-								
1R-CC, 12–17	3.85	4.61	Base	*Emiliania huxleyi*	NN21		0.26	late Pleistocene
2R-CC, 12–17	3.85	4.61	Top	*Pseudoemiliania lacunosa*	NN19		0.42	Pleistocene
3R-CC, 18–23	4.61	14.77	Top	*Sphenolithus* sp.	NN16		3.66	early Pliocene
3R-CC, 18–23	14.77	72.91	Base	*Globorotalia truncatulinoides**		PL1	1.92	late Pliocene and Pleistocene
5R-CC, 8–13	72.91	139.50	Top	*Globorotalia margaritae**		PL2	3.58	early Pliocene
5R-CC, 8–13	72.91	139.50	Top	*Reticulofenestra pseudoumbilicus*	NN13–15		3.8	early Pliocene
7R-1, 50–54	237.40	238.90	Base	*Sphaeroidinella dehiscens*		PL2	5.54	early Pliocene
8R-CC, 0–5	246.03	255.72	Top	*Discoaster quinqueramus*	NN11		5.54	late Miocene
9R-CC, 21–28	264.74	274.03	Base	*Nicklithus amplificus*	NN11		6	late Miocene
20R-CC, 11–16	362.15	371.64	Top	*Chiasmolithus grandis*	NP17		37.1	middle Eocene
20R-5, 116–119	369.26	369.30	Base	*Globorotalia plesiotumida**		M13b	8.58	late Miocene
20R-5, 120–122	369.26	369.30	Top	*Acarinina* and *Morozovella* spp.*		P14	37.5-38.5	middle Eocene
21R-2, 84–86	371.64	374.12	Top	*Orbulinoides beckmanni*		P13	40.1	middle Eocene
20R-CC, 11–16	371.64	375.50	Base	*Dictyococcites bisectus*	NP17		38.5	middle Eocene
21R-CC, 23–29	371.64	375.50	Top	*Chiasmolithus solitus*	NP16		40.4	middle Eocene
27R-CC, 0–6	425.53	433.38	Top	*Chiasmolithus gigas*	NP15		44	middle Eocene
27R-CC, 0–6	433.38	448.94	Base	*Chiasmolithus gigas*	NP15		46.1	middle Eocene
31R-1, 56–58	468.16	487.14	Base	*Morozovella aragonensis**		P7	52.3	early Eocene
32R-CC, 19–24	468.16	487.14	Top	*Morozovella velascoensis* group		P5	54.7	late Paleocene
34R-CC, 0–5	502.29	513.30	Base	*Discoaster multiradiatus*	NP9		56.2	late Paleocene
37R-7, 52–55	534.82	535.02	Base	*Praemurica uncinata*		P2	61.2	early Paleocene
38R-CC, 0–5	535.00	535.26	Top	*Abathomphalus mayaroensis*		KS31	65	Maastrichtian
38R-CC, 0–5	535.00	549.58	Base	*Micula murus*	CC26/26		66.2	late Maastrichtian
37R-CC, 0–3	535.02	535.31	Base	*Chiasmolithus danicus*	NP3		63.8	early Paleocene
37R-CC, 24–29	535.26	535.31		Approximate K/T boundary (nannofossils)			65	K/T boundary
39R-CC, 16–22	549.58	562.21	Base	*Globotruncana aegyptiaca**		KS29–31	73.8	late Campanian–Maastrichtian
40R-6, 55–57	549.58	562.21	Top	*Uniplanarius trifidum*	CC23		76	late Campanian
41R-CC, 21–22	573.69	583.04	Base	*Micula decussata*	CC14		87.2	late Coniacian
42R-3, 106–108	577.33	579.32	Base	*Contusotruncana fornicata*		KS24-23	88	Coniacian
43R-CC, 12–17	590.10	600.49	Base	*Marthasterites furcatus*	CC13		89.3	early Coniacian
44R-6, 65–70	600.49	608.11	Base	*Eiffellithus eximius*	CC12		91	late Turonian
45R-CC, 5–7	608.11	619.06	Base	*Eprolithus eptapetalus*	CC11		93.2	early Turonian
48R-CC, 11–15	630.17	639.93	Top	*Rotalipora* spp.		KS19	94	Cenomanian
48R-CC, 11–15	630.17	639.93	Top	*Axopodorhabdus albianus*	CC10		94	late Cenomanian
50R-3, 0–2	653.20		Base	*Eiffellithus turriseiffelii*	NC10a		101.7	late Albian

Notes: The minimum and maximum depths represent uncertainty in the depth range calculated based on the distance to the relevant subjacent or superjacent sample examined. See "Biostratigraphy," p. 10. * = datum probably does not reflect a true range termination because of either coring gaps or preservational problems. K/T = Cretaceous/Tertiary.

Table T12. Preliminary Campanian–Maastrichtian magnetostratigraphic datums used to calculate sedimentation rates, Hole 1261A.

Polarity chron	Base of chron (mbsf)	Age (Ma)
C29r	534.4	65.58
C31n	544.0	67.61
C31r	555.0	71.07
C32n	560.8	73.00

Note: See **"Paleomagnetism,"** p. 19.

Table T13. Linear sedimentation rates and mass accumulation rates, Hole 1261A.

Epoch	Core, section, interval (cm)	Top		Bottom		Thickness (m)	Duration (m.y.)	LSR*		DBD (g/cm^3)	MAR ($g/cm^2/ky$)
		Depth (mbsf)	Age (Ma)	Depth (mbsf)	Age (Ma)			(m/m.y.)	(cm/k.y.)		
	207-1261A-										
late Miocene–Pliocene	3R-CC, 18 to 9R-CC, 28	14.77	3.66	264.81	6	>250.04	2.34	65	6.5	1.3	8.5
middle Eocene	20R-CC, 11 to 27R-CC, 6	371.64	37.1	433.44	46.1	>61.80	9	8.9	0.89	1.63	1.5
early Eocene–early Paleocene	31R-1, 56 to 37R-7, 55	468.16	52.3	534.85	61.2	>66.69	8.9	7.0	0.70	1.69	1.2
Maastrichtian–late Campanian	38R-CC, 0 to 40R-6, 57	535.00	65	562.23	76	>27.23	11	3.3	0.33	1.37	0.5
Coniacian–Cenomanian	41R-CC, 21 to 48R-CC, 15	573.69	87.2	639.97	94	>66.28	6.8	8.5	0.85	1.63	1.4

Notes: DBD represents the average of the dry bulk densities (DBD) measured on discrete samples for each interval of apparently constant sedimentation. * = linear sedimentation rate (LSR) does not match the slope calculated using the endpoints of each interval as listed because the LSR reported was estimated from a linear fit to all biostratigraphic and paleomagnetic datums within each interval of apparently constant sedimentation. MAR = mass accumulation rate.

Table T14. Total carbon, inorganic carbon, carbonate, total organic carbon, and total nitrogen concentrations and carbon/nitrogen ratios, Site 1261. (**See table notes.** Continued on next page.)

Hole, core, section, interval (cm)	Depth (mbsf)	TC (wt%)	IC (wt%)	$CaCO_3$ (wt%)	TOC (wt%)	N (wt%)	C/N (atomic)
207-							
Unit I (nannofossil ooze and clay):							
1261A-1R-1, 13–14	0.13		5.00	41.63			
1261A-1R-2, 48–49	1.98	1.68	1.17	9.74	0.51	0.07	8.94
1261A-2R-1, 49–50	4.39	1.21	0.72	6.01	0.49	0.06	9.13
1261A-3R-1, 70–71	13.90	1.96	1.80	14.98	0.16	0.04	4.29
1261A-4R-2, 69–70	71.89	1.91	1.68	13.99	0.23	0.05	5.17
1261A-5R-2, 48–49	133.38		1.86	15.53			
1261A-5R-5, 49–50	137.89	2.35	2.16	17.95	0.19	0.06	3.92
1261A-6R-2, 64–65	191.24		2.59	21.58			
1261A-6R-6, 63–64	197.24	3.37	3.18	26.49	0.19	0.06	3.98
1261A-7R-1, 74–75	237.64		2.24	18.64			
1261A-7R-4, 75–76	242.15	2.23	1.98	16.49	0.25	0.05	5.34
1261A-8R-1, 35–36	246.85		2.83	23.60			
1261A-8R-3, 73–74	250.23		1.81	15.06			
1261A-8R-6, 72–73	254.72	2.10	1.68	14.02	0.42	0.09	5.53
1261A-9R-2, 75–76	258.45		2.69	22.43			
1261A-9R-4, 75–76	261.45	1.60	1.42	11.86	0.18	0.08	2.54
1261A-10R-1, 75–76	266.55	3.54	3.37	28.04	0.17	0.05	4.19
1261A-10R-4, 75–76	271.05		2.12	17.65			
1261A-11R-2, 75–76	277.65	3.02	2.86	23.85	0.16	0.05	3.73
1261A-11R-4, 76–77	280.66		2.68	22.33			
1261A-12R-2, 90–91	287.50	3.65	3.48	28.95	0.17	0.05	4.17
1261A-13R-2, 79–81	296.99		3.37	28.09			
1261A-13R-4, 63–65	299.83	3.23	2.98	24.85	0.25	0.04	6.55
1261A-13R-6, 78–80	302.98		3.47	28.93			
1261A-14R-1, 65–66	305.05		2.97	24.70			
1261A-14R-4, 74–75	309.64	3.27	3.01	25.07	0.26	0.05	6.47
1261A-15R-3, 70–71	317.70	3.88	3.76	31.29	0.12	0.04	3.01
1261A-16R-1, 55–56	324.15		6.60	55.01			
1261A-16R-3, 80–81	327.40		6.73	56.03			
1261A-16R-5, 80–81	330.40	7.15	6.91	57.58	0.24	0.01	21.29
1261A-17R-3, 70–71	337.00		7.51	62.58			
1261A-17R-6, 80–81	341.60	3.30	3.15	26.23	0.15	0.05	3.57
1261A-18R-3, 109–110	346.99		4.33	36.06			
1261A-18R-6, 108–109	351.48	5.46	5.18	43.16	0.28	0.04	9.06
1261A-19R-1, 115–116	353.65		8.10	67.44			
1261A-19R-2, 83–84	354.83		9.39	78.22			
1261A-19R-4, 51–52	357.31		6.18	51.48			
1261A-19R-6, 70–71	360.50	6.18	6.10	50.80	0.08	0.01	7.38
1261A-20R-5, 87–88	368.97		5.79	48.20			
Unit II (calcareous chalk with clay):							
1261A-20R-5, 140–142	369.50		10.02	83.50			
1261A-20R-7, 40–41	371.40	9.29	9.22	76.84	0.07	0.01	7.50
1261A-21R-1, 73–74	372.53		9.65	80.36			
1261A-21R-2, 9–10	373.37	8.87	8.56	71.33	0.31	0.03	14.14
1261A-22R-1, 23–24	381.63		9.95	82.91			
1261A-22R-2, 54–55	383.44	8.32	8.28	69.01	0.04	0.00	12.35
1261A-23R-1, 93–94	392.03		9.89	82.36			
1261A-23R-4, 64–65	396.24		9.57	79.69			
1261A-23R-6, 39–40	398.99	7.99	8.02	66.84	0.00	0.01	
1261A-24R-2, 14–15	402.34		9.58	79.81			
1261A-24R-5, 16–17	406.36	8.60	8.45	70.37	0.15	0.00	73.28
1261A-25R-3, 83–84	413.97		9.83	81.86			
1261A-25R-5, 53–54	416.67	9.97	10.08	83.93		0.00	
1261A-26R-1, 73–74	420.63		10.28	85.63			
1261A-26R-3, 38–39	422.88	7.79	7.79	64.86	0.00	0.01	0.33
1261A-27R-1, 132–133	430.82		7.59	63.24			
1261A-27R-3, 71–72	433.21	9.09	9.14	76.16	0.00	0.00	
1261A-28R-1, 94–95	440.04		9.39	78.23			
1261A-28R-6, 107–108	446.77		9.42	78.43			
1261A-28R-7, 72–73	447.92	9.06	8.95	74.54	0.11	0.07	1.86
1261A-29R-1, 23–24	448.93		8.04	66.93			
1261A-29R-3, 10–11	451.80	10.11	10.12	84.32	0.00	0.00	
1261A-30R-1, 50–51	458.80	9.49	9.61	80.03	0.00	0.00	

Table T14 (continued).

Hole, core, section, interval (cm)	Depth (mbsf)	TC (wt%)	IC (wt%)	$CaCO_3$ (wt%)	TOC (wt%)	N (wt%)	C/N (atomic)
1261A-32R-2, 87–88	479.57		8.03	66.86			
1261A-32R-5, 83–84	484.03	7.46	7.42	61.83	0.04	0.01	6.84
1261A-33R-1, 97–98	487.77	7.15	7.19	59.88	0.00	0.01	0.00
Unit III (clayey calcareous chalk):							
1261A-34R-1, 91–92	497.41		5.72	47.61			
1261A-34R-4, 116–117	502.18	3.86	3.78	31.47	0.08	0.02	3.87
1261A-35R-1, 89–90	506.99		6.29	52.43			
1261A-35R-3, 88–89	509.98	5.74	5.71	47.52	0.03	0.01	3.02
1261A-35R-5, 27–28	512.37		5.94	49.48			
1261A-36R-1, 58–59	516.28		6.35	52.91			
1261A-36R-5, 71–72	522.45	4.37	4.45	37.09	0.00	0.02	0.00
1261A-37R-1, 62–63	525.92		8.71	72.58			
1261A-37R-5, 70–71	532.00	6.61	6.61	55.03	0.00	0.01	0.06
1261A-39R-1, 74–75	545.34		9.26	77.11			
1261A-39R-3, 74–75	548.34	6.36	6.30	52.48	0.06	0.01	5.66
1261A-40R-3, 34–35	557.50	6.02	5.94	49.44	0.08	0.01	16.04
1261A-40R-4, 117–118	559.83		2.07	17.25			
1261A-40R-5, 31–32	560.47		2.22	18.52			
1261A-41R-1, 32–33	564.12		5.20	43.29			
Unit IV (laminated black shales):							
1261A-41R-3, 126–127	568.06	12.25	11.21	93.36	1.04	0.03	40.06
1261A-41R-3, 144–145	568.24	14.82	6.49	54.07	8.33	0.30	32.36
1261B-6R-1, 33–34	568.73	13.59	5.83	48.58	7.76	0.29	31.59
1261A-41R-6, 71–72	572.01	12.46	2.39	19.89	10.07	0.43	27.13
1261A-41R-CC, 21–22	573.69	14.36	7.61	63.40	6.75	0.30	25.99
1261B-6R-5, 123–124	575.63	13.82	5.60	46.65	8.22	0.28	33.96
1261A-42R-5, 2–3	579.29	14.99	4.48	37.32	10.51	0.43	28.64
1261B-7R-2, 37–38	579.85	15.31	6.08	50.68	9.23	0.30	36.00
1261A-42R-6, 124–125	582.01	16.01	6.74	56.12	9.27	0.30	35.83
1261B-7R-4, 36–37	582.84	16.31	4.95	41.20	11.36	0.42	31.19
1261A-43R-3, 47–48	586.44	5.32	2.56	21.35	2.76	0.14	23.38
1261A-43R-CC, 1–2	589.99	14.07	5.60	46.65	8.47	0.26	38.02
1261B-8R-2, 101–102	590.11	20.81	4.72	39.34	16.09	0.40	47.05
1261A-44R-2, 3–4	594.13	11.97	4.93	41.12	7.04	0.25	32.49
1261B-9R-1, 63–64	597.83	16.48	5.69	47.38	10.79	0.33	38.47
1261A-44R-5, 10–11	598.44	15.32	5.83	48.59	9.49	0.29	37.92
1261A-44R-6, 23–24	600.07	13.16	4.63	38.59	8.53	0.30	32.99
1261B-9R-5, 66–67	603.81	16.11	5.50	45.80	10.61	0.34	36.04
1261A-45R-2, 103–104	604.53	16.10	5.42	45.21	10.68	0.37	34.10
1261A-45R-3, 2–3	605.00	16.61	5.22	43.46	11.39	0.37	35.88
1261A-45R-4, 27–28	606.77	13.37	6.61	55.04	6.76	0.22	36.64
1261B-10R-3, 38–39	610.18	14.90	3.92	32.66	10.98	0.40	32.08
1261A-46R-2, 1–2	613.22	13.46	7.07	58.86	6.39	0.20	37.42
1261A-46R-2, 91–92	614.12	17.54	5.50	45.82	12.04	0.38	36.66
1261A-46R-5, 16–17	617.80	13.82	5.09	42.44	8.73	0.29	35.31
1261B-11R-2, 90–91	618.80	9.56	0.11	0.92	9.45	0.33	33.14
1261A-47R-2, 1–2	622.80	12.74	0.37	3.11	12.37	0.45	32.07
1261A-47R-4, 137–138	627.09	13.11	1.29	10.71	11.82	0.43	31.96
1261A-48R-2, 47–48	632.97	19.34	6.45	53.75	12.89	0.38	40.03
1261A-48R-5, 73–74	637.68	17.51	1.75	14.54	15.76	0.44	41.91
1261A-49R-3, 32–33	643.90	14.60	5.41	45.04	9.19	0.30	35.87
1261A-49R-6, 113–114	649.21	15.56	4.89	40.74	10.67	0.35	35.36
1261A-50R-3, 12–13	653.32	12.12	11.70	97.44	0.42	0.02	22.65
1261A-50R-3, 17–19	653.37	14.89	4.16	34.66	10.73	0.36	34.74
Unit V (quartz sandstone):							
1261B-16R-1, 99–100	665.49	1.46	0.45	3.76	1.01	0.03	38.35

Notes: TC = total carbon, IC = inorganic carbon, TOC = total organic carbon. Atomic C/N ratios are calculated from concentrations of organic carbon and total nitrogen.

Table T15. Rock-Eval pyrolysis analyses of sediment samples, Site 1261.

Hole, core, section, interval (cm)	Depth (mbsf)	TOC (wt%)	T_{max} (°C)	S_1	S_2	S_3	HI	OI
207-								
Unit IV (laminated black shales):								
1261A-41R-3, 126–127	568.06	1.04	400	0.37	5.54	0.88	532	84
1261A-41R-3, 144–145	568.24	8.33	395	5.33	49.49	5.18	594	62
1261A-41R-6, 71–72	572.01	10.07	402	3.49	60.17	5.51	597	54
1261A-42R-5, 2–3	579.29	10.51	399	3.67	63.99	6.42	608	61
1261A-42R-6, 124–125	582.01	9.27	397	5.01	61.89	5.33	667	57
1261B-7R-4, 36–37	582.84	11.36	395	7.01	70.75	6.60	622	58
1261B-8R-2, 101–102	590.11	16.09	395	10.52	104.32	8.60	648	53
1261A-44R-2, 3–4	594.13	7.04	389	4.97	45.84	4.64	651	65
1261B-9R-1, 63–64	597.83	10.79	397	5.70	67.06	6.00	621	55
1261B-9R-5, 66–67	603.81	10.61	395	6.53	60.34	6.24	568	58
1261A-45R-2, 103–104	604.53	10.68	393	6.46	68.32	5.84	639	54
1261A-45R-3, 2–3	605.00	11.39	397	3.97	71.48	3.70	627	28
1261B-10R-3, 38–39	610.18	10.98	398	3.96	74.61	3.01	679	27
1261A-46R-2, 91–92	614.12	12.04	395	7.67	67.34	4.29	559	35
1261B-11R-2, 90–91	618.80	9.45	394	3.29	46.53	1.95	452	20
1261A-47R-2, 1–2	622.80	12.37	397	2.32	51.82	2.88	418	23
1261A-47R-4, 137–138	627.09	11.82	393	4.05	71.56	3.31	605	28
1261A-48R-2, 47–48	632.97	12.89	393	5.44	78.95	3.97	612	30
1261A-48R-5, 73–74	637.68	15.76	399	4.60	88.00	4.70	558	25
1261A-49R-3, 32–33	643.90	9.19	400	2.48	45.14	3.81	491	41
1261A-49R-6, 113–114	649.21	10.67	400	5.50	67.77	3.64	635	34
1261A-50R-3, 17–19	653.37	10.73	399	2.20	58.43	3.23	544	30
Unit V (quartz sandstone):								
1261B-16R-1–100	665.49	1.01	412	0.34	3.16	1.02	312	100

Note: TOC = total organic carbon. HI = milligrams of hydrocarbon-like material (S_2) per gram of organic carbon; OI = milligrams of CO_2 (S_3) per gram of organic carbon. See **"Organic Geochemistry,"** p. 27, in the "Explanatory Notes" chapter for definitions of T_{max}, S_1, S_2, and S_3.

Table T16. Headspace analyses of interstitial and microbial gases, Site 1261.

Hole, core, section, interval (cm)	Depth (mbsf)	Routine safety monitoring				Microbial study			
		C_1 (ppmv)	C_2 (ppmv)	C_3 (ppmv)	C_1/C_2	C_1 (ppmv)	C_2 (ppmv)	C_3 (ppmv)	C_1/C_2
207-									
Unit I (nannofossil ooze and clay):									
1261A-4R-1, 140–145	71.10	3							
1261A-5R-5, 0–5	137.40	6							
1261A-6R-4, 0–5	193.60	6							
1261A-7R-4, 0–5	241.40	7							
1261A-8R-4, 0–5	251.00	10							
1261A-9R-3, 0–5	259.20	7							
1261A-10R-3, 0–5	268.80	5							
1261A-11R-3, 0–5	278.40	5							
1261A-12R-3, 0–5	288.10	4							
1261A-13R-3, 0–5	297.70	3							
1261A-14R-3, 0–5	307.40	2							
1261A-15R-3, 0–5	317.00	3							
1261A-16R-4, 0–5	328.10	2							
1261A-17R-3, 0–5	336.30	2							
1261A-18R-3, 0–5	345.90	3							
1261A-19R-4, 0–5	356.80	2							
1261A-20R-4, 0–5	366.60	2							
Unit II (calcareous chalk with clay):									
1261A-21R-2, 128–130	374.56	2							
1261A-22R-2, 0–5	382.90	2							
1261A-23R-2, 148–150	394.08	7							
1261A-24R-2, 118–120	403.38	57							
1261A-25R-1, 132–134	411.62	3							
1261A-26R-4, 0–5	424.00	161							
1261A-27R-2, 0–2	431.00	299							
1261A-28R-4, 108–110	444.18	638	1		912				
1261A-29R-3, 0–2	451.70	1,113	1		795				
1261A-30R-2, 0–2	459.66	955	1		796				
1261A-31R-1, 57–58	468.17	738	1		820				
1261A-32R-3, 0–5	480.20	1,697	2		849				
1261A-33R-2, 145–150	489.75	1,538	1		1,099				
Unit III (clayey calcareous chalk):									
1261A-34R-3, 145–150	500.95	5,646	5		1,046				
1261A-35R-3, 0–1	509.10	4,165	5		926				
1261A-36R-3, 0–5	518.70	2,018	2		939				
1261A-37R-3, 0–1	528.30	2,018	3		701				
1261B-2R-2, 0–5	531.50	1,805	4		430	1,292	1		897
1261B-3R-3, 145–150	544.05	3,957	3		1,319	6,660	5		1,257
1261A-39R-2, 0–5	546.10	7,266	7		1,118				
1261B-4R-1, 145–150	550.65	7,522	6		1,233	8,341	7		1,180
1261A-40R-4, 0–2	558.60	5,828	8		757				
1261B-5R-3, 152–153	562.20	19,297	20		970	22,626	22		1,033
Unit IV (laminated black shales):									
1261A-41R-4, 148–150	569.78	61,774	140	12	440				
1261B-6R-3, 148–150	572.88	43,271	88	7	493	57,778	135	11	429
1261A-42R-2, 0–2	574.90	17,776	34		521				
1261B-7R-5, 0–2	583.98	14,150	36		396	29,237	62	4	470
1261A-43R-3, 0–2	585.97	111,037	234	15	474				
1261B-8R-3, 0–2	590.60	8,402	15		556	28,251	53		535
1261A-44R-3, 0–2	595.36	26,083	65	4	401				
1261B-9R-2, 0–2	598.70	51,687	87	4	595	57,172	86	4	664
1261A-45R-2, 146–148	604.96	62,777	160	9	391				
1261B-10R-2, 148–150	609.78	44,464	115	8	388	57,938	98	5	588
1261A-46R-4, 145–147	617.62	81,931	147	9	559				
1261B-11R-2, 0–2	617.90	30,989	47		655	48,335	80	6	607
1261B-12R-2, 0–2	627.45	43,868	90	8	486	53,016	78	5	676
1261A-47R-CC, 14–18	630.17	41,212	94	9	438				
1261A-48R-3, 148–150	635.48	88,624	112	7	788				
1261B-13R-3, 0–2	638.56	91,881	94	7	973	31,612	36		868
1261A-49R-3, 145–150	645.03	51,117	85	7	603				
1261B-14R-3, 0–2	648.20	25,718	39		659	49,294	59		829
1261A-50R-2, 145–150	653.15	53,844	71		759				

Note: C_1 = methane, C_2 = ethane, C_3 = propane.

Table T17. Interstitial water analyses, Site 1261.

Core, section, interval (cm)	Depth (mbsf)	Depth (mcd)	Salinity	Alkalinity (mM)	pH	Cl^- (mM)	$*SO_4^{2-}$ (mM)	NH_4^+ (µM)	$*H_4SiO_4$ (µM)	B (mM)	Li^+ (µM)	Sr^{2+} (µM)	Ca^{2+} (mM)	K^+ (mM)	Mg^{2+} (mM)	Mn^{2+} (µM)	Fe^{2+} (µM)	Ba^{2+} (µM)	Na^+ (mM)	Na^+ diff
207-1261A-																				
1R-2, 145–150	2.95	2.95	35.3	4.06	7.55	562	26.7	105	319	0.55	33	95	9.6	11.4	49.0	16	14	0.8	469	490
3R-1, 134–139	14.54	14.54	34.7	3.73	7.38	573	22.6	570	169	0.62	34	111	9.7	10.7	46.4	8	6	0.3	478	498
4R-1, 145–150	71.15	71.15	34.5	3.29	7.54	582	11.9	940	191	0.39	31	181	10.2	8.4	37.1	5	7	1.5	492	504
5R-4, 140–150	137.30	137.30	33.7	2.46	7.44	600	2.9	1520	190	0.32	32	301	11.6	6.4	32.1	6	6	2.7	496	513
6R-5, 140–151	196.50	196.50	35.0	1.98	7.39	622	0.6	1580	182	0.35	32	458	13.7	5.8	29.9	7	7	28.9	499	529
7R-3, 140–150	241.30	241.30	35.5	1.91	7.33	637	0.2	1610	180	0.36	34	621	15.7	5.3	30.1	9	8	49.9	511	540
8R-3, 140–150	250.90	250.90	35.5	1.78	7.39	637	0.0	1610	160	0.39	34	668	16.1	5.3	29.2	9	7	48.7	522	540
10R-3, 140–150	270.20	270.20	36.3	1.58	7.48	649	0.1	1620	136	0.38	38	772	16.4	5.6	30.4	8	1	46.7	518	549
12R-5, 0–10	291.10	291.10	36.5	1.69	7.48	658	0.0	1455	145	0.42	48	857	17.0	5.5	32.2	7	3	41.5	532	552
14R-6, 90–100	312.80	312.80	36.7	1.43	7.69	662	0.3	1390	105	0.38	69	944	16.7	5.9	30.9	3	1	39.3	537	559
16R-3, 140–150	328.00	328.00	36.7	0.96	8.06	661	0.6	1750	60	0.28	80	1020	16.3	6.7	31.3	2	1	32.3	537	557
18R-5, 139–150	350.29	350.29	38.0	1.42	7.71	669	0.4	1610	96	0.35	114	1103	16.8	6.5	33.3	3	0	22.2	550	560
20R-6, 130–140	370.90	370.90	39.5	1.41	7.85	678	1.3	1690	351	0.36	137	1111	17.0	6.9	35.0	1	0	12.2	545	567
22R-3, 46–61	384.86	384.86	39.0	ND	ND	690	1.3	1650	577	0.47	162	1205	18.2	7.0	35.4	0	0	8.3	558	575
25R-4, 0–7	414.64	414.64	40.5	ND	ND	711	0.9	1515	733	0.56	197	1216	20.4	7.4	37.6	1	6	32.6	585	585
32R-5, 140–150	484.60	484.60	44.0	0.77	7.50	775	0.1	1415	346	0.27	268	1424	23.6	7.1	37.4	0	0	63.9	592	642
35R-5, 0–15	512.10	512.10	42.0	ND	ND	737	0.7	1210	307	0.32	292	1409	24.7	6.0	39.7	1	0	39.9	593	599
37R-1, 135–150	526.65	526.65	44.5	ND	ND	793	0.5	1630	136	0.20	283	1382	24.6	7.0	37.6	0	0	58.7	629	658
39R-1, 135–150	545.95	545.95	47.5	5.03	7.11	802	0.0	1560	477	0.69	306	1498	28.9	6.4	39.8	0	1	146.6	643	658
45R-3, 138–152	606.36	606.33	50.3	ND	ND	859	0.3	1800	637	0.89	312	1560	32.0	6.4	37.1	0	1	239.2	695	709
48R-5, 136–150	638.31	635.37	51.5	3.88	7.12	897	0.0	1845	608	0.96	318	1579	33.3	6.2	35.2	0	0	260.8	730	752
207-1261B-																				
11R-2, 147–157	619.37	612.38	48.0	4.75	7.02	849	1.4	1840	706	0.96	301	1342	30.0	6.2	35.3	0	0	64.6	697	715
14R-2, 130–140	648.00	647.25	51.0	4.29	7.29	907	0.0	1815	446	1.12	330	1670	33.3	5.8	31.8	1	1	250.2	750	769

Notes: * = ICP-AES. ND = not determined.

Table T18. Index properties of discrete samples, Holes 1261A and 1261B. (See table note. Continued on next three pages.)

Core, section, interval (cm)	Depth (mbsf)	Depth (mcd)	Water content (%) Wet	Water content (%) Dry	Density Bulk	Density Dry	Density Grain	Porosity (%)	Void ratio
207-1261A-									
1R-1, 78–80	0.78	0.78	48.8	95.3	1.512	0.774	2.768	72.0	2.576
1R-2, 34–36	1.84	1.84	46.8	87.9	1.540	0.820	2.765	70.4	2.374
3R-1, 18–20	13.38	13.38	40.5	68.1	1.644	0.978	2.796	65.0	1.861
4R-1, 54–56	70.24	70.24	35.9	55.9	1.715	1.100	2.753	60.0	1.502
4R-2, 70–72	71.90	71.90	34.5	52.6	1.751	1.148	2.796	58.9	1.436
5R-1, 68–70	132.08	132.08	31.0	44.9	1.792	1.236	2.702	54.2	1.185
5R-2, 89–91	133.79	133.79	30.8	44.5	1.805	1.250	2.732	54.3	1.187
5R-3, 80–82	135.20	135.20	31.8	46.5	1.783	1.217	2.723	55.3	1.237
5R-4, 98–100	136.88	136.88	29.7	42.3	1.826	1.283	2.731	53.0	1.128
6R-1, 74–76	189.84	189.84	29.6	42.0	1.810	1.274	2.670	52.3	1.096
6R-2, 65–67	191.25	191.25	28.8	40.5	1.829	1.302	2.685	51.5	1.063
6R-3, 77–79	192.87	192.87	29.3	41.5	1.823	1.289	2.695	52.2	1.091
6R-4, 68–70	194.28	194.28	29.3	41.5	1.834	1.296	2.729	52.5	1.106
6R-6, 64–66	197.25	197.25	28.8	40.4	1.840	1.310	2.713	51.7	1.071
7R-1, 86–88	237.76	237.76	30.0	42.8	1.824	1.277	2.739	53.4	1.144
7R-2, 74–76	239.14	239.14	27.9	38.8	1.851	1.334	2.693	50.5	1.020
7R-3, 72–74	240.62	240.62	28.2	39.2	1.865	1.339	2.752	51.3	1.055
7R-4, 78–80	242.18	242.18	28.3	39.5	1.859	1.332	2.741	51.4	1.058
7R-5, 82–84	243.72	243.72	28.7	40.2	1.837	1.311	2.699	51.4	1.059
7R-6, 73–75	245.13	245.13	27.1	37.2	1.918	1.398	2.842	50.8	1.033
8R-1, 78–80	247.28	247.28	26.8	36.6	1.881	1.377	2.712	49.2	0.969
8R-2, 85–87	248.85	248.85	28.0	38.9	1.855	1.335	2.711	50.7	1.030
8R-3, 88–90	250.38	250.38	28.3	39.5	1.852	1.327	2.721	51.2	1.051
8R-4, 74–76	251.74	251.74	27.0	36.9	1.862	1.360	2.669	49.0	0.962
8R-5, 83–85	253.33	253.33	27.5	38.0	1.877	1.360	2.748	50.5	1.020
9R-1, 76–78	256.96	256.96	28.6	40.1	1.844	1.316	2.717	51.6	1.065
9R-2, 31–33	258.01	258.01	27.7	38.3	1.840	1.331	2.647	49.7	0.990
9R-3, 87–89	260.07	260.07	28.9	40.6	1.824	1.298	2.672	51.4	1.059
9R-5, 78–80	262.98	262.98	27.2	37.3	1.866	1.359	2.690	49.5	0.979
9R-6, 38–40	264.08	264.08	28.7	40.3	1.840	1.312	2.710	51.6	1.065
10R-1, 110–112	266.90	266.90	27.1	37.2	1.880	1.371	2.729	49.8	0.991
10R-2, 45–47	267.75	267.75	27.0	37.0	1.864	1.360	2.675	49.2	0.967
10R-3, 63–65	269.43	269.43	27.9	38.6	1.866	1.346	2.733	50.7	1.030
10R-4, 90–92	271.20	271.20	27.9	38.7	1.867	1.346	2.738	50.8	1.034
10R-5, 30–32	272.10	272.10	25.9	35.0	1.901	1.408	2.717	48.2	0.929
11R-1, 67–69	276.07	276.07	28.8	40.4	1.833	1.306	2.693	51.5	1.063
11R-2, 77–79	277.67	277.67	27.1	37.2	1.862	1.357	2.679	49.3	0.974
11R-3, 86–88	279.26	279.26	28.2	39.3	1.862	1.337	2.745	51.3	1.053
11R-4, 72–74	280.62	280.62	28.7	40.2	1.847	1.318	2.728	51.7	1.070
11R-5, 72–74	282.12	282.12	28.3	39.6	1.868	1.338	2.770	51.7	1.070
11R-6, 79–81	283.69	283.69	29.5	41.9	1.817	1.280	2.689	52.4	1.101
12R-1, 79–81	285.89	285.89	26.3	35.7	1.910	1.407	2.762	49.0	0.962
12R-2, 25–27	286.85	286.85	27.3	37.5	1.871	1.361	2.713	49.8	0.993
12R-4, 78–80	290.38	290.38	26.5	36.1	1.888	1.387	2.716	48.9	0.958
12R-5, 86–88	291.96	291.96	26.4	35.9	1.892	1.393	2.719	48.8	0.952
13R-1, 80–82	295.50	295.50	21.5	27.3	1.901	1.493	2.482	39.9	0.663
13R-2, 78–80	296.98	296.98	25.1	33.6	1.885	1.411	2.626	46.3	0.861
13R-3, 67–69	298.37	298.37	21.5	27.4	1.875	1.472	2.426	39.3	0.648
13R-4, 63–65	299.83	299.83	21.6	27.5	1.901	1.491	2.489	40.1	0.669
13R-5, 89–91	301.59	301.59	19.1	23.7	1.930	1.561	2.442	36.1	0.565
13R-6, 78–80	302.98	302.98	21.8	27.8	1.907	1.491	2.508	40.5	0.682
14R-1, 64–66	305.04	305.04	21.6	27.6	1.909	1.497	2.506	40.3	0.675
14R-2, 74–76	306.64	306.64	21.6	27.5	1.902	1.491	2.489	40.1	0.669
14R-3, 132–134	308.72	308.72	21.2	26.9	1.917	1.511	2.504	39.7	0.657
14R-4, 75–77	309.65	309.65	22.1	28.4	1.892	1.474	2.491	40.8	0.690
14R-5, 25–27	310.65	310.65	20.4	25.6	1.985	1.580	2.612	39.5	0.653
14R-5, 58–60	310.98	310.98	27.1	37.1	1.927	1.405	2.865	51.0	1.039
14R-5, 66–68	311.06	311.06	17.9	21.8	1.953	1.603	2.436	34.2	0.520
14R-5, 101–103	311.41	311.41	22.9	29.7	1.886	1.455	2.514	42.1	0.728
14R-5, 143–145	311.83	311.83	21.7	27.7	1.910	1.495	2.514	40.5	0.681
14R-6, 8–10	311.98	311.98	29.6	42.1	1.747	1.229	2.485	50.5	1.022
14R-6, 27–29	312.17	312.17	22.2	28.5	1.917	1.492	2.551	41.5	0.710
14R-6, 53–55	312.43	312.43	22.3	28.6	1.931	1.501	2.586	42.0	0.723
14R-6, 75–77	312.65	312.65	24.5	32.4	1.890	1.427	2.604	45.2	0.825
14R-6, 85–87	312.75	312.75	24.4	32.3	1.903	1.438	2.636	45.4	0.832
14R-7, 13–15	313.03	313.03	22.3	28.7	1.904	1.480	2.527	41.5	0.708

Table T18 (continued).

Core, section, interval (cm)	Depth (mbsf)	Depth (mcd)	Water content (%) Wet	Water content (%) Dry	Density Bulk	Density Dry	Density Grain	Porosity (%)	Void ratio
14R-7, 33–35	313.23	313.23	23.5	30.7	1.928	1.474	2.645	44.3	0.794
14R-7, 53–55	313.43	313.43	24.8	33.1	1.908	1.434	2.669	46.3	0.862
15R-1, 25–27	314.25	314.25	32.6	48.3	1.772	1.195	2.738	56.3	1.291
15R-1, 85–87	314.85	314.85	25.9	35.0	1.875	1.389	2.643	47.5	0.903
15R-1, 130–132	315.30	315.30	28.9	40.7	1.855	1.318	2.769	52.4	1.101
15R-2, 30–32	315.80	315.80	27.8	38.4	1.859	1.343	2.707	50.4	1.016
15R-2, 85–87	316.35	316.35	27.8	38.5	1.870	1.350	2.742	50.7	1.030
15R-2, 131–133	316.81	316.81	24.9	33.2	1.929	1.449	2.729	46.9	0.884
15R-3, 31–33	317.31	317.31	27.1	37.1	1.877	1.369	2.717	49.6	0.985
15R-3, 85–87	317.85	317.85	26.5	36.1	1.896	1.392	2.737	49.1	0.966
15R-3, 110–112	318.10	318.10	23.4	30.6	1.920	1.471	2.621	43.9	0.782
15R-4, 37–39	318.87	318.87	21.5	27.4	1.942	1.524	2.573	40.8	0.688
15R-4, 78–80	319.28	319.28	21.1	26.7	1.938	1.530	2.544	39.9	0.663
15R-4, 112–114	319.62	319.62	24.7	32.7	1.898	1.430	2.633	45.7	0.841
15R-5, 24–26	320.24	320.24	20.4	25.7	1.959	1.559	2.559	39.1	0.642
15R-5, 88–90	320.88	320.88	21.6	27.5	1.976	1.550	2.655	41.6	0.713
15R-5, 107–109	321.07	321.07	25.8	34.8	1.850	1.373	2.571	46.6	0.873
15R-5, 128–130	321.28	321.28	20.4	25.6	1.950	1.552	2.538	38.8	0.635
15R-6, 21–23	321.71	321.71	21.9	28.0	1.942	1.517	2.593	41.5	0.710
15R-6, 48–50	321.98	321.98	29.2	41.2	1.781	1.262	2.560	50.7	1.029
15R-6, 100–102	322.50	322.50	25.3	33.9	1.843	1.377	2.526	45.5	0.835
16R-1, 54–56	324.14	324.14	28.5	39.8	1.820	1.302	2.635	50.6	1.024
16R-1, 100–102	324.60	324.60	26.1	35.4	1.848	1.365	2.584	47.2	0.893
16R-2, 80–82	325.90	325.90	26.6	36.3	1.836	1.347	2.580	47.8	0.915
16R-3, 80–82	327.40	327.40	27.8	38.4	1.851	1.337	2.684	50.2	1.007
16R-4, 80–82	328.90	328.90	26.1	35.4	1.870	1.382	2.642	47.7	0.913
16R-5, 80–82	330.40	330.40	26.8	36.7	1.833	1.341	2.581	48.0	0.924
17R-1, 77–79	334.07	334.07	27.1	37.2	1.824	1.329	2.571	48.3	0.935
17R-2, 63–65	335.43	335.43	22.5	29.1	1.972	1.528	2.700	43.4	0.767
17R-3, 69–71	336.99	336.99	26.3	35.6	1.880	1.386	2.677	48.2	0.931
17R-4, 80–82	338.60	338.60	26.4	35.8	1.886	1.388	2.699	48.6	0.944
17R-5, 79–81	340.09	340.09	25.9	35.0	1.897	1.405	2.703	48.0	0.923
17R-6, 81–83	341.61	341.61	20.3	25.5	2.045	1.629	2.742	40.6	0.683
18R-1, 66–68	343.56	343.56	26.5	36.1	1.894	1.392	2.730	49.0	0.961
18R-2, 88–90	345.28	345.28	22.1	28.4	1.978	1.541	2.691	42.8	0.747
18R-4, 73–75	348.13	348.13	24.3	32.1	1.947	1.474	2.739	46.2	0.858
18R-5, 74–76	349.64	349.64	24.6	32.5	1.960	1.478	2.789	47.0	0.887
18R-6, 74–76	351.14	351.14	24.0	31.5	1.942	1.477	2.708	45.4	0.833
19R-1, 23–25	352.73	352.73	20.9	26.5	1.949	1.541	2.562	39.9	0.663
19R-2, 62–64	354.62	354.62	27.3	37.5	1.865	1.357	2.694	49.6	0.985
19R-3, 50–52	355.80	355.80	22.1	28.3	1.952	1.521	2.625	42.1	0.726
19R-4, 52–54	357.32	357.32	23.9	31.5	1.922	1.462	2.655	44.9	0.816
19R-5, 60–62	358.90	358.90	28.7	40.3	1.867	1.331	2.796	52.4	1.101
19R-6, 26–28	360.06	360.06	23.1	30.1	1.953	1.501	2.688	44.2	0.791
19R-7, 60–62	361.90	361.90	28.4	39.6	1.862	1.334	2.754	51.6	1.064
20R-1, 70–72	362.80	362.80	24.8	33.0	1.905	1.432	2.663	46.2	0.859
20R-2, 70–72	364.30	364.30	24.2	32.0	1.929	1.462	2.688	45.6	0.839
20R-3, 70–72	365.80	365.80	25.4	34.0	1.910	1.426	2.705	47.3	0.897
20R-4, 70–72	367.30	367.30	25.9	34.9	1.889	1.400	2.677	47.7	0.912
20R-5, 68–70	368.78	368.78	29.6	42.0	1.852	1.304	2.805	53.5	1.152
20R-6, 78–80	370.38	370.38	24.1	31.7	1.957	1.487	2.752	46.0	0.851
20R-7, 30–32	371.30	371.30	22.4	28.8	2.013	1.562	2.789	44.0	0.785
21R-1, 64–66	372.44	372.44	21.9	28.1	1.977	1.543	2.678	42.4	0.735
21R-2, 27–29	373.55	373.55	24.0	31.6	1.920	1.459	2.655	45.0	0.820
21R-3, 24–26	374.82	374.82	16.5	19.8	2.129	1.778	2.707	34.3	0.523
22R-1, 62–64	382.02	382.02	22.3	28.7	1.991	1.547	2.732	43.4	0.766
22R-2, 70–72	383.60	383.60	20.2	25.3	2.035	1.624	2.714	40.1	0.671
23R-1, 31–33	391.41	391.41	18.5	22.7	2.073	1.690	2.699	37.4	0.597
23R-2, 54–56	393.14	393.14	19.0	23.5	2.045	1.656	2.670	38.0	0.612
23R-3, 32–34	394.42	394.42	18.0	21.9	2.072	1.700	2.670	36.3	0.571
23R-4, 39–40	395.99	395.99	19.1	23.6	2.053	1.662	2.691	38.2	0.619
23R-5, 43–44	397.53	397.53	21.9	28.1	1.972	1.539	2.664	42.2	0.731
23R-7, 40–42	400.50	400.50	15.0	17.7	2.167	1.841	2.699	31.8	0.466
24R-1, 29–31	400.99	400.99	16.2	19.4	2.128	1.783	2.689	33.7	0.508
24R-2, 61–63	402.81	402.81	19.2	23.8	2.045	1.652	2.681	38.4	0.623
24R-3, 28–30	403.68	403.68	19.3	23.9	2.034	1.642	2.659	38.3	0.620
24R-5, 29–31	406.49	406.49	19.0	23.5	2.078	1.682	2.740	38.6	0.629
25R-1, 55–57	410.85	410.85	20.7	26.0	2.003	1.589	2.666	40.4	0.678
25R-2, 64–66	412.28	412.28	19.4	24.1	2.030	1.635	2.660	38.5	0.627

Table T18 (continued).

Core, section, interval (cm)	Depth (mbsf)	Depth (mcd)	Water content (%) Wet	Water content (%) Dry	Density Bulk	Density Dry	Density Grain	Porosity (%)	Void ratio
25R-3, 45–47	413.59	413.59	14.0	16.2	2.186	1.881	2.681	29.8	0.425
25R-4, 69–71	415.33	415.33	17.9	21.8	2.081	1.709	2.684	36.3	0.571
25R-5, 31–33	416.45	416.45	14.3	16.6	2.281	1.956	2.867	31.8	0.466
26R-1, 27–29	420.17	420.17	21.0	26.7	2.002	1.581	2.687	41.2	0.699
26R-2, 94–96	422.19	422.19	22.7	29.4	1.958	1.513	2.677	43.5	0.769
26R-3, 11–13	422.61	422.61	17.6	21.3	2.113	1.742	2.734	36.3	0.570
26R-4, 13–15	424.13	424.13	18.2	22.3	2.126	1.739	2.797	37.8	0.608
26R-5, 47–49	425.47	425.47	18.8	23.1	2.068	1.680	2.706	37.9	0.611
27R-1, 58–60	430.08	430.08	17.4	21.1	2.097	1.732	2.691	35.6	0.554
27R-2, 69–71	431.69	431.69	21.2	26.8	2.042	1.610	2.785	42.2	0.730
27R-3, 56–58	433.06	433.06	18.2	22.2	2.079	1.700	2.696	36.9	0.586
28R-1, 58–59	439.68	439.68	20.3	25.5	2.016	1.606	2.678	40.0	0.667
28R-2, 17–19	440.27	440.27	16.6	20.0	2.149	1.792	2.753	34.9	0.537
28R-3, 44–46	442.04	442.04	18.1	22.0	2.062	1.690	2.656	36.4	0.572
28R-4, 16–18	443.26	443.26	14.7	17.3	2.165	1.846	2.680	31.1	0.452
28R-5, 30–32	444.50	444.50	17.9	21.8	2.047	1.681	2.615	35.7	0.556
28R-6, 17–19	445.87	445.87	23.6	30.9	1.919	1.467	2.628	44.2	0.792
28R-7, 12–14	447.32	447.32	17.7	21.5	2.075	1.707	2.663	35.9	0.560
29R-1, 26–28	448.96	448.96	16.8	20.2	2.085	1.735	2.637	34.2	0.520
29R-2, 91–92	451.11	451.11	21.0	26.5	1.963	1.551	2.594	40.2	0.672
29R-3, 14–16	451.84	451.84	17.6	21.3	2.077	1.712	2.659	35.6	0.553
30R-1, 50–52	458.80	458.80	13.1	15.1	2.217	1.926	2.690	28.4	0.397
30R-2, 36–38	460.02	460.02	15.2	17.9	2.121	1.798	2.626	31.5	0.460
31R-1, 48–50	468.08	468.08	16.8	20.2	2.090	1.738	2.648	34.4	0.523
32R-1, 17–19	477.37	477.37	15.3	18.0	2.182	1.849	2.740	32.5	0.482
32R-2, 13–15	478.83	478.83	14.9	17.6	2.158	1.835	2.679	31.5	0.460
32R-5, 15–16	483.35	483.35	17.8	21.6	2.027	1.667	2.572	35.2	0.542
33R-1, 7–9	486.87	486.87	16.2	19.4	2.107	1.765	2.651	33.4	0.502
34R-1, 54–56	497.04	497.04	21.2	27.0	1.927	1.518	2.529	40.0	0.666
34R-3, 24–26	499.76	499.76	21.7	27.6	1.887	1.479	2.461	39.9	0.664
35R-1, 88–90	506.98	506.98	20.0	25.1	2.011	1.608	2.651	39.3	0.649
35R-3, 106–108	510.16	510.16	19.2	23.8	2.070	1.672	2.734	38.8	0.635
35R-5, 23–25	512.33	512.33	19.8	24.7	2.015	1.617	2.647	38.9	0.638
36R-3, 4–6	518.74	518.74	19.0	23.4	2.059	1.669	2.697	38.1	0.616
36R-5, 8–10	521.82	521.82	19.6	24.4	2.054	1.652	2.723	39.3	0.648
37R-1, 31–33	525.61	525.61	16.3	19.5	2.112	1.768	2.663	33.6	0.506
37R-3, 3–5	528.33	528.33	13.0	14.9	2.225	1.936	2.697	28.2	0.393
37R-5, 9–11	531.39	531.39	25.4	34.1	1.887	1.408	2.648	46.8	0.881
37R-7, 44–46	534.74	534.74	14.4	16.9	2.211	1.892	2.749	31.2	0.453
39R-1, 46–48	545.06	545.06	16.2	19.4	2.151	1.802	2.733	34.1	0.517
40R-1, 37–39	554.57	554.57	11.7	13.3	2.278	2.011	2.719	26.0	0.352
40R-2, 45–47	556.15	556.15	20.9	26.4	1.990	1.575	2.649	40.6	0.682
40R-3, 31–33	557.47	557.47	18.1	22.2	2.019	1.653	2.572	35.8	0.557
40R-4, 89–91	559.55	559.55	24.5	32.4	1.854	1.400	2.515	44.3	0.796
40R-5, 25–27	560.41	560.41	27.7	38.3	1.771	1.281	2.458	47.9	0.919
40R-6, 33–35	561.99	561.99	22.2	28.6	1.911	1.486	2.538	41.4	0.708
41R-1, 32–34	564.12	565.03	31.2	45.3	1.673	1.152	2.347	50.9	1.038
41R-3, 144–146	568.24	569.15	28.2	39.3	1.758	1.261	2.448	48.5	0.941
41R-4, 56–58	568.86	569.77	24.6	32.6	1.885	1.422	2.595	45.2	0.826
41R-6, 65–67	571.95	572.86	23.0	29.9	1.903	1.465	2.558	42.7	0.746
42R-1, 50–52	573.90	575.56	22.0	28.3	1.944	1.515	2.605	41.8	0.719
42R-3, 104–106	577.31	578.97	24.5	32.4	1.982	1.497	2.844	47.4	0.900
42R-4, 5–7	577.82	579.48	30.9	44.6	1.654	1.143	2.280	49.8	0.994
42R-7, 58–60	582.83	584.49	35.9	56.0	1.619	1.038	2.398	56.7	1.311
43R-3, 91–93	586.88	588.16	9.8	10.8	2.339	2.110	2.717	22.3	0.288
43R-4, 65–67	588.00	589.28	19.8	24.8	1.861	1.492	2.333	36.1	0.564
43R-5, 108–109	589.93	591.21	31.0	45.0	1.688	1.164	2.383	51.1	1.047
44R-1, 3–5	592.63	594.04	36.1	56.6	1.560	0.996	2.217	55.1	1.225
44R-4, 131–134	598.15	599.56	7.5	8.2	2.462	2.276	2.781	18.1	0.222
44R-6, 61–63	600.45	601.86	29.7	42.3	1.722	1.210	2.421	50.0	1.000
45R-3, 128–130	606.26	606.23	32.9	49.0	1.639	1.100	2.323	52.6	1.112
45R-4, 88–90	607.38	607.35	30.9	44.8	1.648	1.138	2.266	49.8	0.991
45R-5, 34–36	607.84	607.81	28.5	40.0	1.760	1.257	2.468	49.1	0.963
45R-5, 48–50	607.98	607.95	25.0	33.3	1.844	1.384	2.514	45.0	0.817
45R-CC, 5–7	608.11	608.08	16.2	19.3	2.159	1.809	2.747	34.1	0.518
46R-2, 51–53	613.72	611.62	33.1	49.5	1.629	1.089	2.302	52.7	1.114
46R-5, 16–18	617.80	615.70	31.9	46.9	1.665	1.133	2.356	51.9	1.079
46R-5, 106–108	618.70	616.60	15.9	18.9	2.089	1.758	2.600	32.4	0.479
47R-2, 71–73	623.50	621.40	30.3	43.4	1.606	1.120	2.133	47.5	0.905

Table T18 (continued).

Core, section, interval (cm)	Depth (mbsf)	Depth (mcd)	Water content (%) Wet	Water content (%) Dry	Density Bulk	Density Dry	Density Grain	Porosity (%)	Void ratio
47R-5, 1–3	627.18	625.08	20.2	25.3	2.003	1.599	2.641	39.5	0.652
47R-5, 76–78	627.93	625.83	31.1	45.1	1.636	1.127	2.239	49.7	0.987
207-1261B-									
2R-1, 12–15	530.12	534.72	12.9	14.8	2.232	1.944	2.705	28.1	0.392
2R-1, 132–134	531.32	535.92	15.2	18.0	2.174	1.842	2.724	32.4	0.478
2R-2, 41–43	531.91	536.51	15.2	18.0	2.158	1.829	2.694	32.1	0.473
2R-2, 130–132	532.80	537.40	16.1	19.2	2.096	1.758	2.624	33.0	0.492
2R-3, 48–50	533.48	538.08	14.7	17.3	2.142	1.826	2.642	30.9	0.446
2R-3, 103–105	534.03	538.63	12.9	14.8	2.665	2.321	3.497	33.6	0.507
3R-1, 22–24	539.82	541.30	12.8	14.6	2.221	1.938	2.679	27.7	0.383
3R-3, 48–50	543.08	544.56	12.8	14.7	2.208	1.925	2.661	27.7	0.382
3R-4, 103–105	545.13	546.61	21.7	27.8	1.944	1.522	2.591	41.3	0.703
3R-5, 18–20	545.78	547.26	11.3	12.7	2.301	2.042	2.734	25.3	0.339
3R-6, 25–27	546.85	548.33	20.1	25.2	2.025	1.617	2.688	39.8	0.662
4R-1, 31–33	549.51	550.55	16.7	20.0	2.070	1.725	2.603	33.7	0.509
4R-2, 24–26	550.94	551.98	23.2	30.2	1.909	1.466	2.585	43.3	0.763
4R-3, 55–57	552.75	553.79	22.6	29.2	1.945	1.505	2.639	43.0	0.753
4R-4, 5–7	553.75	554.79	11.5	13.0	2.314	2.047	2.768	26.1	0.352
4R-4, 94–96	554.64	555.68	16.3	19.5	2.093	1.751	2.626	33.3	0.500
5R-1, 28–30	559.08	559.71	21.8	27.9	1.920	1.501	2.540	40.9	0.692
5R-2, 72–74	560.10	560.73	22.7	29.3	1.913	1.480	2.567	42.4	0.735
5R-7, 17–19	566.88	567.51	29.1	41.1	1.698	1.203	2.328	48.3	0.935
6R-3, 75–77	572.15	573.41	28.6	40.0	1.692	1.209	2.288	47.2	0.893
6R-5, 0–2	574.40	575.66	26.8	36.5	1.775	1.300	2.426	46.4	0.866
6R-7, 8–10	577.28	578.54	28.4	39.8	1.725	1.234	2.370	47.9	0.920
7R-1, 55–57	578.55	579.15	11.2	12.7	2.319	2.058	2.762	25.5	0.342
7R-4, 100–102	583.48	584.08	30.9	44.8	1.655	1.143	2.286	50.0	1.001
7R-5, 1–3	583.99	584.59	16.1	19.2	2.045	1.716	2.529	32.1	0.474
8R-1, 38–40	587.98	587.79	32.9	49.0	1.613	1.082	2.247	51.8	1.076
8R-2, 108–110	590.18	589.99	32.9	48.9	1.643	1.103	2.334	52.7	1.115
9R-2, 4–6	598.74	599.34	27.3	37.5	1.680	1.222	2.211	44.8	0.810
9R-3, 55–57	600.70	601.30	29.8	42.4	1.651	1.159	2.230	48.0	0.923
9R-4, 85–87	602.50	603.10	29.4	41.6	1.689	1.193	2.315	48.5	0.940
10R-2, 85–87	609.15	606.97	29.7	42.2	1.673	1.176	2.285	48.5	0.942
10R-3, 58–60	610.38	608.20	6.4	6.8	2.450	2.293	2.707	15.3	0.181
11R-1, 78–80	617.18	610.19	30.7	44.2	1.652	1.145	2.268	49.5	0.980
11R-2, 14–16	618.04	611.05	31.3	45.6	1.817	1.247	2.808	55.6	1.251
12R-1, 73–75	626.73	625.35	23.3	30.4	1.864	1.430	2.482	42.4	0.736
12R-2, 7–9	627.52	626.14	18.1	22.1	1.938	1.588	2.413	34.2	0.520
13R-1, 11–13	635.71	634.47	32.7	48.6	1.529	1.029	2.011	48.9	0.956
13R-5, 3–5	641.59	640.35	20.5	25.8	1.944	1.545	2.530	38.9	0.638
14R-2, 1–3	646.71	645.96	19.2	23.7	1.981	1.601	2.546	37.1	0.590

Note: This table is also available in **ASCII.**

Table T19. Average difference between GRA bulk density and MAD measurements, Holes 1261A and 1261B.

Unit/ subunit	Hole	Average difference (g/cm^3)	Number of samples
	207-		
IA	1261A	0.026	4
IB	1261A	0.068	51
IC	1261A	0.126	61
II	1261A	0.376	47
IIIA	1261A	0.206	11
	1261B	0.307	5
IIIB	1261A	0.249	8
	1261B	0.185	12
IV	1261A	0.230	22
	1261B	0.315	18

Note: Differences are calculated for each hole and lithostratigraphic unit. Where the difference between MAD and the GRA density exceeded 0.9 g/cm^3, the sample was omitted.

Table T20. Discrete measurements of *P*-wave velocity, Site 1261.

Core, section, interval (cm)	Depth (mbsf)	Depth (mcd)	Velocity (m/s) x	Velocity (m/s) y	Velocity (m/s) z
207-1261A-					
1R-1, 87	0.87	0.87	1489.8		
1R-1, 121.6	1.22	1.22	1489.4		
1R-2, 35.2	1.85	1.85	1492.9		
1R-2, 120.9	2.71	2.71	1490.7		
1R-3, 13.6	3.14	3.14	1492.8		
3R-1, 20.5	13.40	13.40	1532.7		
3R-1, 96.1	14.16	14.16	1508.1		
4R-1, 13.8	69.84	69.84	1536.9		
4R-1, 55.4	70.25	70.25	1537.3		
4R-1, 126.1	70.96	70.96	1545.2		
4R-2, 10	71.30	71.30	1535.2		
4R-2, 69.9	71.90	71.90	1546.5		
4R-3, 14.5	72.35	72.35	1547.5		
4R-3, 47.2	72.67	72.67	1541.7		
5R-1, 15.8	131.56	131.56	1587.9		
5R-1, 68.7	132.09	132.09	1574.0		
5R-1, 125	132.65	132.65	1572.1		
5R-2, 15.5	133.05	133.05	1565.1		
5R-2, 53.5	133.43	133.43	1561.3		
5R-2, 91.3	133.81	133.81	1566.6		
5R-2, 129.4	134.19	134.19	1586.3		
5R-3, 9.4	134.49	134.49	1578.7		
5R-3, 43.2	134.83	134.83	1572.6		
5R-3, 82.5	135.23	135.23	1564.6		
5R-4, 16.5	136.07	136.07	1591.2		
5R-4, 58	136.48	136.48	1561.6		
5R-4, 98.8	136.89	136.89	1569.7		
5R-4, 128.8	137.19	137.19	1590.5		
5R-5, 12.6	137.53	137.53	1574.4		
5R-5, 62.3	138.02	138.02	1597.0		
5R-5, 116.9	138.57	138.57	1579.8		
5R-6, 9.5	138.99	138.99	1571.8		
5R-6, 36.3	139.26	139.26	1575.7		
6R-1, 27.7	189.38	189.38	1571.5		
6R-1, 76.6	189.87	189.87	1600.2		
6R-1, 122.8	190.33	190.33	1615.7		
6R-2, 22	190.82	190.82	1589.4		
6R-2, 67.1	191.27	191.27	1605.6		
6R-2, 129.7	191.90	191.90	1606.7		
6R-3, 23.2	192.33	192.33	1621.3		
6R-3, 77.8	192.88	192.88	1607.7		
6R-3, 134.8	193.45	193.45	1622.8		
6R-4, 17.7	193.78	193.78	1619.4		
6R-4, 69.2	194.29	194.29	1611.6		
6R-4, 120.6	194.81	194.81	1630.2		
6R-6, 13	196.74	196.74	1617.7		
6R-6, 65.1	197.26	197.26	1636.0		
6R-6, 118.1	197.79	197.79	1629.3		
6R-6, 129.3	197.90	197.90	1638.9		
7R-1, 18.6	237.09	237.09	1591.2		
7R-1, 86.1	237.76	237.76	1591.0		
7R-1, 133	238.23	238.23	1617.1		
7R-2, 17.2	238.57	238.57	1616.8		
7R-2, 75.3	239.15	239.15	1603.3		
7R-2, 133.9	239.74	239.74	1593.6		
7R-3, 17.8	240.08	240.08	1613.3		
7R-3, 72.6	240.63	240.63	1617.1		
7R-3, 119.5	241.10	241.10	1613.1		
7R-4, 21.3	241.61	241.61	1610.9		
7R-4, 78.1	242.18	242.18	1608.9		
7R-4, 131.6	242.72	242.72	1615.6		
7R-5, 21.6	243.12	243.12	1620.9		
7R-5, 83.1	243.73	243.73	1603.6		
7R-5, 133.1	244.23	244.23	1631.6		
7R-6, 23.2	244.63	244.63	1621.9		
7R-6, 74	245.14	245.14	1611.7		
7R-6, 116.4	245.56	245.56	1602.1		
8R-1, 27	246.77	246.77	1605.9		
8R-1, 79.1	247.29	247.29	1601.7		
8R-1, 133.4	247.83	247.83	1581.2		
8R-2, 18	248.18	248.18	1608.5		
8R-2, 86.2	248.86	248.86	1606.1		
8R-2, 132.2	249.32	249.32	1613.1		
8R-3, 24.4	249.74	249.74	1624.5		
8R-3, 89.6	250.40	250.40	1619.2		
8R-4, 13.6	251.14	251.14	1620.3		
8R-4, 75.5	251.76	251.76	1614.7		
8R-4, 131.8	252.32	252.32	1623.0		
8R-5, 24.4	252.74	252.74	1610.8		
8R-5, 84.7	253.35	253.35	1619.8		
8R-5, 125.5	253.76	253.76	1624.3		
8R-6, 19	254.19	254.19	1617.6		
8R-6, 56.8	254.57	254.57	1624.9		
8R-6, 91.4	254.91	254.91	1631.7		
8R-7, 14.1	255.14	255.14	1633.1		
8R-7, 56.6	255.57	255.57	1630.7		
9R-1, 23.3	256.43	256.43	1603.3		
9R-1, 77.2	256.97	256.97	1589.6		
9R-1, 131.3	257.51	257.51	1609.2		
9R-2, 33	258.03	258.03	1567.0		
9R-2, 82.6	258.53	258.53	1630.9		
9R-2, 138.5	259.08	259.08	1618.1		
9R-3, 27.6	259.48	259.48	1612.8		
9R-3, 88.5	260.08	260.08	1617.8		
9R-3, 138.4	260.58	260.58	1613.9		
9R-4, 59.8	261.30	261.30	1608.6		
9R-4, 119.9	261.90	261.90	1616.0		
9R-5, 26.7	262.47	262.47	1625.0		
9R-5, 79.2	262.99	262.99	1617.5		
9R-5, 122.1	263.42	263.42	1621.3		
9R-6, 38.8	264.09	264.09	1611.6		
10R-1, 40.5	266.20	266.20	1624.3		
10R-1, 111.1	266.91	266.91	1635.7		
10R-2, 46.9	267.77	267.77	1634.4		
10R-2, 131.9	268.62	268.62	1649.1		
10R-3, 12.4	268.92	268.92	1606.0		
10R-3, 64	269.44	269.44	1629.0		
10R-3, 115.6	269.96	269.96	1622.7		
10R-4, 18.1	270.48	270.48	1640.3		
10R-4, 91.1	271.21	271.21	1639.0		
10R-4, 138.5	271.68	271.68	1630.4		
10R-5, 31.3	272.11	272.11	1642.4		
10R-5, 99.1	272.79	272.79	1625.5		
10R-5, 141.5	273.21	273.21	1654.3		
10R-6, 18	273.48	273.48	1657.5		
11R-1, 20.8	275.61	275.61	1584.7		
11R-1, 68	276.08	276.08	1591.9		
11R-1, 133.3	276.73	276.73	1620.7		
11R-2, 26.5	277.17	277.17	1633.2		
11R-2, 79.1	277.69	277.69	1604.4		
11R-2, 129.4	278.19	278.19	1634.3		
11R-3, 19.1	278.59	278.59	1598.0		
11R-3, 86.6	279.27	279.27	1625.1		
11R-3, 140.8	279.81	279.81	1640.9		
11R-4, 17.7	280.08	280.08	1601.6		
11R-4, 71.8	280.62	280.62	1622.2		
11R-4, 136.4	281.26	281.26	1638.3		
11R-5, 22.1	281.62	281.62	1629.8		
11R-5, 72.5	282.12	282.12	1640.9		

Notes: Multiple axis measurements were performed on 2-cm^3 samples. x-direction is perpendicular to the surface of a split core, y-direction is parallel to the surface of a split core, and z-direction is perpendicular to the top of the core. Only a portion of this table appears here. The complete table is available in **ASCII.**

Table T21. Checkshot survey data, Site 1261.

Checkshot station	Depth (mbrf)	Depth (mbsf)	Traveltime (sbsl)	Traveltime (sbsf two-way)	Interval time (s)	RMS velocity (m/s)	Interval velocity (m/s)
1	1911.0	0.0	1.269	0.000	1.269	1495.0	1495.0
2	2025.0	114.0	1.346	0.152	0.076	1495.0	1495.6
3	2040.0	129.0	1.355	0.170	0.009	1496.3	1671.3
4	2065.0	154.0	1.370	0.201	0.015	1497.6	1609.7
5	2085.0	174.0	1.382	0.225	0.012	1499.2	1669.5
6	2105.0	194.0	1.394	0.249	0.012	1499.9	1581.1

Notes: sbsl = seconds below sea level, sbsf = seconds below seafloor. RMS = root mean square. Rig floor (including Kelly Bushing) to sea level = 11.7 m. Air gun depth = 2 mbsl.